A test for the existence of protons in ultra-high energy cosmic rays

Dissertation
zur Erlangung des Grades eines
Doktors der Naturwissenschaften

erstellt von
Philipp Heimann, M.Sc.RWTH

eingereicht bei der Naturwissenschaftlich-Technischen Fakultät
der Universität Siegen
Siegen, Juni 2018

gedruckt auf alterungsbestndigem holz- und säurefreiem Papier

Betreuer und erster Gutachter:
Prof. Dr. rer. nat. Markus Risse
Zweiter Gutachter:
Prof. Dr. rer. nat. Ivor Fleck

Datum der Disputation: 2. Oktober 2018

Abstract

The determination of the composition of cosmic rays at ultra-high energies is still a challenge in astroparticle physics. Beside of the determination of the overall composition the knowledge of the general existence of single elements, specifically protons, is sufficient for certain analyses. This work presents a method which is able to reject the helium origin of single very deep air shower events. Utilizing a parametrized distribution of shower maxima, predicted by different hadronic interaction models and CONEX, it is possible to determine a probability value of a helium nucleus to induce an air shower with the observed depth of shower maximum or deeper. If this derived probability value is small enough, the hypothesis of a helium primary can be rejected. Since heavier primaries than helium tend to produce air showers with lower depths than Helium, which leads to smaller probabilities for deep events, these possible primaries can be excluded as well. After the development of the method, a check of the method's performance is presented and a first application to the data of the Pierre Auger Observatory is performed. The result shows that this method might be able to exclude the helium origin hypothesis with good significance.

Kurzzusammenfassung

Die Bestimmung der Massenkomposition der kosmischen Strahlung bei höchsten Energien gehört immer noch zu den Herausforderungen der modernen Astroteilchenphysik. Neben der Bestimmung der Gesamtkomposition kann es für einige Analysen ausreichen, die Existenz bestimmter Primärteilchen bei einer bestimmten Energie nachzuweisen. In dieser Arbeit wird eine Methode präsentiert, die die Parametrisierung der Verteilung der Tiefe des Maximums von Luftschauern, vorhergesagt durch CONEX für verschiedene hadronische Interaktionsmodelle, nutzt, um eine Wahrscheinlichkeit zu bestimmen, dass ein primärer Heliumkern einen Luftschauer mit der beobachteten Tiefe des Maximums oder tiefer auslöst. Wenn diese Wahrscheinlichkeit klein genug ist, kann die Hypothese eines primären Heliumkerns verworfen werden. Da noch schwerere Primärteilchen dazu tendieren Luftschauer mit kleineren Tiefen des Schauermaximums zu produzieren, können ebenso diese schweren Teilchen ausgeschlossen werden. Nach der Beschreibung der entwickelten Methode wird ein kurzer Test ihrer Leistungsfähigkeit präsentiert, bevor sie dann eine erste Anwendung auf Daten des Pierre Auger Observatoriums findet. Diese erste Anwendung zeigt, dass die Methode in der Lage sein kann, die Helium Hypothese mit guter Signifikanz auszuschließen.

Contents

0 Introduction

In this work a method to check for the existence of ultra-high energy protons is presented and applied to the data collected with the hybrid detector of the Pierre Auger Observatory. The method utilizes the properties of the distributions of the depths of maximum of extensive air showers to assign probabilities to the individual showers to be produced by helium nuclei. In case the helium probability is sufficiently low the conservative conclusion can be made that the shower was produced by the primary proton. The outcome of the method is the maximum energy at which the existence of the primary protons can be stated at the given confidence level.

In the first chapter a short overview of the phenomenology of cosmic rays and extensive air showers is given, starting with a short historic overview of the discovery over a description of the cosmic ray spectrum, source candidates and possible acceleration mechanisms to the atmospheric phenomenon of extensive air showers and their properties.

The second chapter presents the Pierre Auger Observatory, giving an overview of the two main detector systems, the surface and the fluorescence detector, the data acquisition, additional systems on site, the ongoing upgrade of the detector and the reconstruction procedure.

The third chapter gives an introduction into a modified Maxwell theory with Lorentz invariance violation, which can be regarded as a specific motivation for the development of this analysis. In the following sections is the basic idea and approach of the analysis is presented and the necessary modifications for the application to data are derived.

After the presentation of the analysis method the fourth chapter shows the performance of the method using different compositions with artificial mock data samples.

The description of the data selection and the presentation of the used data set of the Pierre Auger Observatory is the topic of the fifth chapter, while the sixth chapter presents the first results of the applied analysis.

The last chapter summarizes the developed analysis and the results of the application to the data of the Pierre Auger Observatory and gives an outlook for future applications and possible improvements.

1 Cosmic Rays

1.1. Discovery of Cosmic Rays

In the late 18^{th} century it was discovered an electroscope loses its charge over time, which was first reported by Charles-Augustin de Coulomb [Cou85]. He explained this effect with dust particles in the surrounding air, which would cause a loss of charge. Later experiments with instruments which were better protected against other loss currents showed that this explanation cannot hold. After the dicovery of ionizing radiation from radioactive elements, Julius Elster, Hans Geitel and Charles Thomson Rees Wilson found out that this radiation can cause the discharge of electroscopes [Els01, Wil01]. Thus the phenomenon of "self-discharging" electroscopes was explained by the ionizing radiation of radioactive elements in the Earth's surface.

But measurements of the ionization in air by Theodor Wulf on the Eiffel Tower in 1909 showed a confusing result: The ionization rate was decreasing with height, but the decrease was not as strong as one could expect for measurements in this height [Wul09]. In 1912, Victor F. Hess discovered an increasing ionization rate at higher altitudes during a balloon flight [Hes12]. His measurements were confirmed by Kolhörster and later by Millikan, who was able to measure in the stratosphere due to measurement automatization [Kol13, Kol14, Mil]. To explain the phenomenon of this "Höhenstrahlung", it was proposed that it is of cosmic origin.

In 1938, Pierre Auger discovered coincident signals between several particle detectors at a distance of approximately 100 m during a measurement at the Jungfraujoch in Switzerland [Aug39]. Auger concluded that the detected particles should have the same origin: a very high energy cosmic particle with an estimated energy of approximately 10^{15} eV. He proposed that this primary particle induced an avalanche of other particles, an extensive air shower.

1.2. Spectrum

Various measurements of cosmic rays showed a wide spectrum. It covers more than 10 magnitudes in energy and 30 magnitudes in flux [Oli14]. The energy range starts less than 10^9 eV (1 GeV) and was measured up to

slightly more than 10^{20} eV. These highest energies lead to center-of-mass energies in the collision with (resting) Nitrogen atoms of the Earth's atmosphere of approximately 1600 TeV, which is significantly higher than the LHC's center of mass energy (E_{CM} = 14 TeV [Oli14]). While cosmic rays of lower energies (around 10^{12} eV) have a flux of about one particle per square meter and second, the flux at ultra-high energies (above 10^{19} eV) drops down to one particle per square kilometer and century and below.

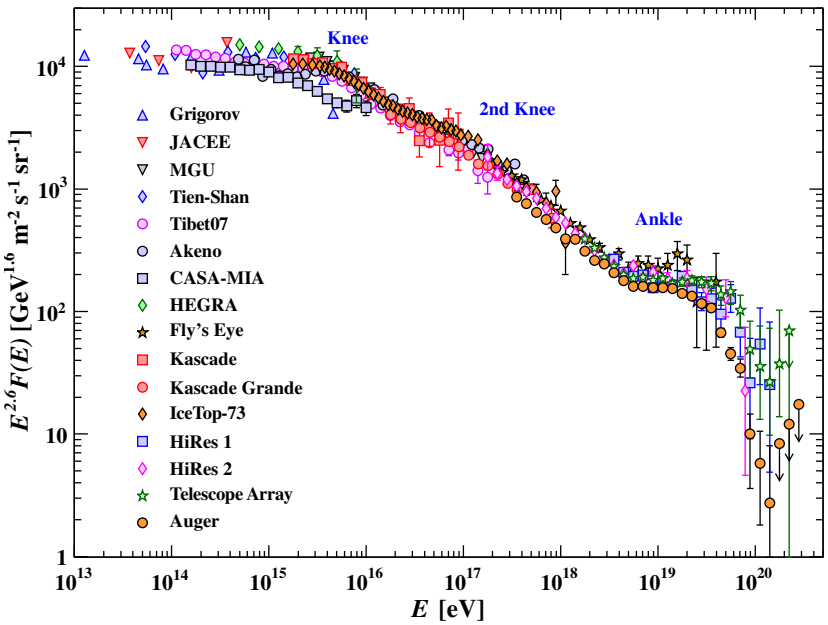

Figure 1.1.: All particle spectrum.[Oli14]

1.2.1. Lower end of the spectrum

Since cosmic ray particles need a certain minimum momentum to not be deflected by the Earth's magnetic field, the energy spectrum shows a cutoff depending on the observer's position and time. At the lower end of the cosmic ray spectrum, at energies of a few 10 GeV, the primary cosmic ray spectrum is additionally influenced by sun activity like sun spots or sun winds.

With increasing energy, the influence of the described local effects diminishes as shown in figure 1.1 and the spectrum follows a power law

$$\Phi \propto E^{-\gamma}. \tag{1.1}$$

For energies lower than $10^{15.5}$ eV the spectral index has a value of $\gamma \approx 2.7$. In this energy region, the spectral index changes to $\gamma \approx 3.1$. This feature of the spectrum is known as the "knee".

1.2.2. The knee

The reason for the change in the spectrum is still unknown. Nevertheless, there are several theories which describe possible origins of the knee. A short overview of these theories shall be given here.

The first class of theories describes the knee as a feature of the acceleration mechanism, commonly based on the shock acceleration described in section 1.3. The maximum energy a particle can achieve on cosmic timescales is $\sim Z \cdot 10^{15}$ eV, where Z is the charge number of the particle. The existence of the knee can be explained with the highest achievable energy of protons and their cut-off in the all particle spectrum. This would result in a measurable change in the composition of cosmic rays on Earth since the abundance of light primaries will decrease at higher energies than the knee due to this maximum achievable energy [Gai16].

Other theories include a background spectrum without any features, which is modified by a single local source like a supernova remnant, the assumption of the diffusive behavior of cosmic rays within the galaxy or the introduction of new particles outside the standard model [Gai16].

Measurements of the spectrum in the energy range of the knee indicate that the composition trends to heavier elements with increasing energy. This would prefer theories including this trend to heavier compositions, like the shock acceleration model or even the featureless background with a local source, which predicts particles of the Carbon, Nitrogen, and Oxygen (CNO) group. Nevertheless, the question of the origin of the knee is not finally solved since there are a lot of uncertainties such as the usage of various hadronic interaction models in the reconstruction of the data [Gai16].

1.2.3. The second knee

At about two orders of magnitude higher energies ($\sim 10^{17.6}$ eV) the spectrum gets slightly steeper again with a spectral index of $\gamma \approx 3.3$, the "second knee" [Gai16].

The most common explanations for this feature are extensions to the models on the existence of the knee. As mentioned the maximum achievable energy is proportional to the charge of the accelerated particle. This induces directly a multi knee theory, which includes a knee for every possible element. Following this, the second knee is correlated to the energy at which the heaviest elements with nucleus charge of $Z = 92$ have their cut-off energy [Gai16].

On the other hand, this model needs several assumptions, which include a non-neglectible fraction of heavy elements with $Z \geq 28$ in the primary cosmic ray composition. Since the question of the composition is still not finally answered (see section 1.5), these models are still under investigation [Gai16].

1.2.4. The ankle

At an energy of $10^{18.6}$ eV the spectrum gets flatter again, and the spectral index changes back to $\gamma \approx 2.6$, the so-called "ankle" [Gai16].

Most commonly the ankle is interpreted as the transition region from galactic to extragalactic sources. Since the models discussed for the knee and the second knee predict a cut off, the direct link between the transition and the ankle require an additional galactic component of heavy nuclei, which stands in contradiction to recent measurements in this energy range, which indicate a lighter composition [Gai16].

In the dip model, which is another but controversial model, the transition starts at the region of the second knee, where galactic iron dominated cosmic rays transits to light (proton) dominated extragalactic cosmic rays [Gai16].

In addition to these models, it is possible that the extragalactic spectrum is influenced by several effects during its propagation to the Earth, e.g. photo-disintegration of heavier nuclei with photons of the cosmic microwave background or the extragalactic background light [Gai16].

1.2.5. The spectrum at highest energies

At the highest energies of above $10^{19.7}$ eV the flux is suppressed (see figure 1.2). The first predictions of such a suppression were made by Greisen [Gre66] and seperately by Zatsepin and Kuz'min [Zat66] in 1966. Their calculations were based on the interaction of protons in the cosmic rays with photons of the cosmic microwave background. In this reaction

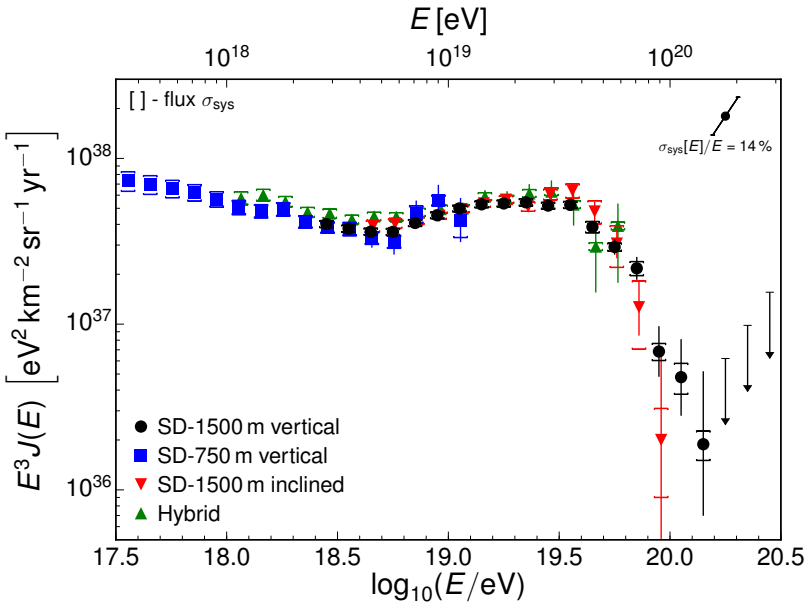

Figure 1.2.: ICRC 2015 data of Auger [Val15].

a Δ-resonance is produced.

$$\begin{aligned} p + \gamma_{\mathrm{CMB}} \rightarrow \Delta^{+}(1232) &\rightarrow p + \pi^{0} \\ &\rightarrow n + \pi^{+} \end{aligned}$$

Depending on the photon's energy, the proton's threshold energy for the $\Delta(1232)$-production is about $6 \cdot 10^{19}\,\mathrm{eV}$. Even if the GZK cutoff-energy matches quite well with the observed flux suppression at highest energies, the influence of this mechanism is not clear. Other possible origins of this flux suppression might be effects of the cosmic ray propagations (e.g. photo-disintegration) or simply the lack of sources able to accelerate particles up to these high energies.

Nonetheless, in 1962 the first cosmic ray particle of more than $10^{20}\,\mathrm{eV}$ was detected by the Volcanic ranch experiment [Lin63]. The highest energy ever was measured in 1991 at the Fly's Eye experiment with $3.2 \cdot 10^{20}\,\mathrm{eV}$ [Bir93].

1.3. Acceleration mechanisms

A central question of cosmic rays is the origin of their enormous energy. Several theories were proposed to explain the cosmic rays' energy. These theories can be divided into two categories, which are discussed in the following sections.

1.3.1. Bottom up models

Bottom-up models describe all processes which accelerate low energetic particles to high energies. In the following direct acceleration mechanism and the shock acceleration are presented.

Direct acceleration

As mentioned in section 1.2, the spectrum of cosmic rays follows a power law. This power law stands in contradiction to a thermal source for ultra-high energetic cosmic rays since the spectrum of a thermal acceleration would follow Planck's law. Even though the idea of acceleration with electric fields are disfavoured since the massive amount of ionized matter would short-circuit electric fields, which would be strong enough to accelerate ultra-high energetic cosmic rays [Gai16], this acceleration might be possible in local fields on short time-scales.

Stochastic acceleration

Another way to possibly accelerate particles to highest energies is shock acceleration. The energy gain of the charged particles is achieved via multiple scattering in a turbulent magnetic field.

The basis of these processes is the Fermi mechanism, which transfers the kinetic energy of the cloud to the particles to be accelerated. For the time being the particles are considered to be at relativistic energies already. Due to the different directions and velocities of particle and cloud it is possible that the particles enter the cloud several times. Considering that the particle increases its energy by a relative amount $\Delta E = \xi E$, the total energy of the particle after n acceleration cycles is given by

$$E_n = E_0 (1 + \xi)^n \Rightarrow n = \frac{\ln\left(\frac{E_n}{E_0}\right)}{\ln(1 + \xi)}, \tag{1.2}$$

where E_0 is the particle's energy before the first cycle [Sta10]. Now, assuming the particle has a probability P_{esc} to escape the acceleration cycle, the probability that the particle remains in the acceleration after n cycles is $(1-P_{\mathrm{esc}})^n$. Therefore the number N of particles with energies larger than E_n is

$$N(\geq E_n) \propto \sum_{m=n}^{\infty} (1-P_{\mathrm{esc}})^m = \frac{(1-P_{\mathrm{esc}})^n}{P_{\mathrm{esc}}} \tag{1.3}$$

Substituting n in 1.3 with 1.2 leads to

$$N(\geq E_n) \propto \frac{1}{P_{\mathrm{esc}}} \left(\frac{E_n}{E_0}\right)^{-\gamma}, \tag{1.4}$$

with

$$\gamma = \frac{\ln\left(\frac{1}{1-P_{\mathrm{esc}}}\right)}{\ln(1+\xi)}. \tag{1.5}$$

This mechanism gives naturally a power law as observed in cosmic rays. The relative energy gain per acceleration cycle in an interstellar cloud is given by

$$\xi = \frac{\Delta E}{E} = \gamma_{\mathrm{cl}}^2 (1+\beta_{\mathrm{cl}})^2, \tag{1.6}$$

where γ_{cl} is the Lorentz factor and β_{cl} the velocity in units of speed of light in vacuum of the cloud [Sta10]. ξ depends on the angle of the particle with respect to the moving direction of the cloud before and after the cycle. Averaging over these angles gives an average relative energy gain

$$\bar{\xi} \simeq \frac{4}{3}\beta_{\mathrm{cl}}^2. \tag{1.7}$$

This mechanism is referred to as second-order Fermi acceleration, due to the β_{cl}^2 proportion of $\bar{\xi}$. This proportion causes that the second order Fermi mechanism is quite inefficient and is unable to accelerate cosmic ray particles to highest energies, even within cosmological timescales.

Replacing the interstellar cloud with a plane shock wave (e.g. from a supernova remnant) the average relative energy gain is given by

$$\bar{\xi} \sim \frac{4}{3}\beta_S, \tag{1.8}$$

where $\beta_S = \frac{v_1 - v_2}{c_0}$ is the relative velocity of the plasma flow at the shock. The acceleration using these astrophysical shocks yields the first-order

Fermi mechanism, which is more efficient than the second-order Fermi mechanism. In this case, the spectral index is only depending on the compression of the shock

$$\gamma = \frac{3}{v_1/v_2 - 1}, \tag{1.9}$$

and the maximum achievable energy depends on the lifetime of the shock fronts [Sta10].

1.3.2. Top down models

In contrast to bottom-up models, top-down models predict the origin of ultra-high energetic cosmic ray in the decay of hypothetical particles. These hypothetical X particles are necessarily extremely massive with rest masses $m_0 c^2 \gg 10^{21}\,\mathrm{eV}$, which removes the imperative for a sufficient acceleration mechanism like in the bottom-up models. Examples for top-down allowing theories were super-heavy dark matter [Kuz98], annihilation of relic neutrinos in Z-Bursts [Fod02] or topological defects [Kal99].

These theories give a comfortable way to describe the production of cosmic rays. However, most of these models were heavily constrained or even excluded from measurements, for instance by searches for ultra-high energetic photons [Aab17].

1.4. Possible Sources

The possible sources of high energy cosmic rays are as various as the theories of the acceleration of cosmic ray particles. While the sun is the main source for the lower end of the spectrum (energies of a few GeV), the higher end of the spectrum remains still unclear.

Anthony Hillas defined in 1984 the simple Hillas-criterion

$$B\,[\mu\mathrm{G}] \cdot L\,[\mathrm{kpc}] > E\,[\mathrm{EeV}] \cdot \frac{2}{Z\beta}, \tag{1.10}$$

where the ability to accelerate particles to a certain energy E requires a sufficiently large size L or a sufficiently strong magnetic field B [Hil84], while Z is the charge number of the cosmic ray particle and β its velocity in terms of the speed of light.

Nonetheless, even some distant astronomical objects seem to be able to produce cosmic rays with highest energies (compare figure 1.3).

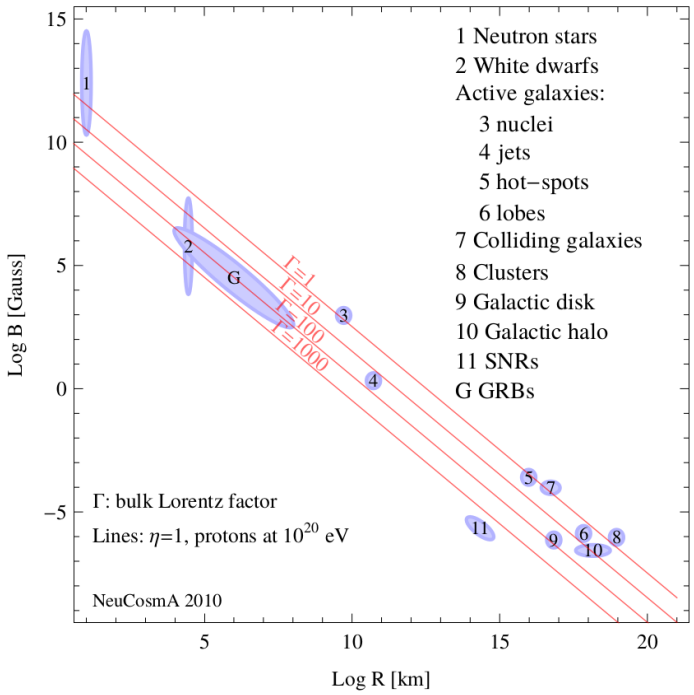

Figure 1.3.: Different possible sources of cosmic rays in an Hillas plot. ν is the acceleration efficiency and Γ is the Lorentz factor of the acceleration region [Hüm10].

Active galactic nuclei (AGN) and radio lobes

Active galactic nuclei (AGN) can be found at the center of active galaxies, which is, in general, a super-massive black hole with its accretion disk around it [Gai16]. With an extreme magnetic field of several hundred Gauss strength and a size of the accretion disk of about 10^{-5} pc, AGN fulfill the Hillas criterion of equation 1.10 even for energies up to 10^{20} eV [Gai16]. Even direct acceleration mechanism might be possible, since local electrical potential differences of 10^{21} V may be possible on short time-scales. In the radio lobes of radio-loud AGN, first-order Fermi acceleration might be possible up to energies of 10^{19} eV [Gai16].

However, it is assumed that most of the energy is lost while an ultra-high energetic particle propagates through the surrounding of the AGN. In this radiation field, the ultra-high energetic particles should suffer from synchrotron losses, interactions with photons of the field or adia-

batic losses, which predict particles with an energy of 10^{16} eV to be emitted by an AGN [Gai16].

Besides the acceleration of particles in the inner region of an AGN, it might be possible that so-called hot spots in the radio lobes of AGN can achieve highest energies. The strongest shocks possible are assumed to be in these hot spots, where the first order Fermi mechanism might accelerate particles up to 10^{21} eV.

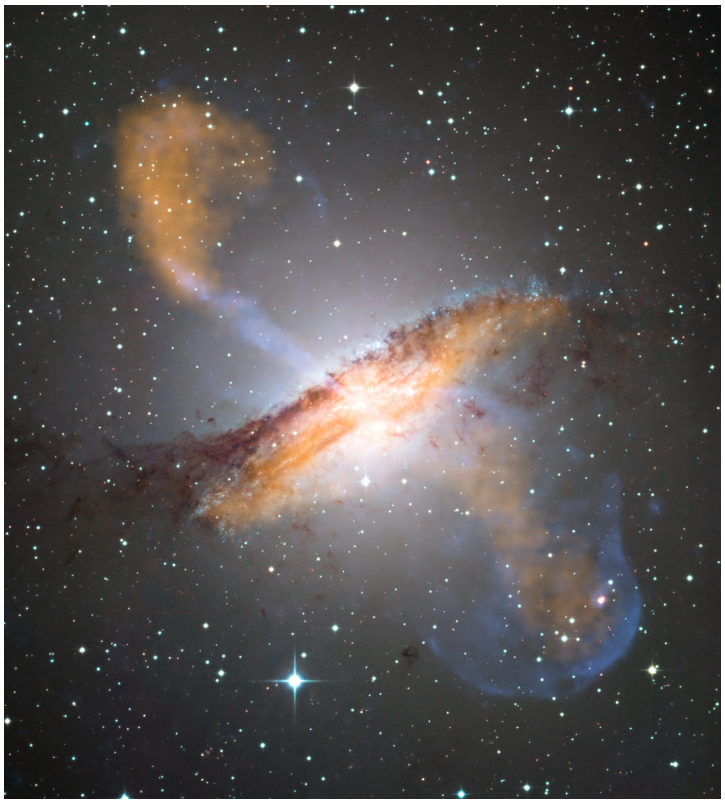

Figure 1.4.: Centaurus A (composite image) as an example of an active galaxy [ESO09].

The closest galaxy with an active nucleus is Centaurus A (CenA, NGC 5128, figure 1.4), which has a distance of 3.8 ± 0.1 Mpc to the solar system [Har10]. Therefore CenA is a promising candidate for a local source of cosmic rays, inside the GZK horizon. But recent results can still not confirm Centaurus A as a source for ultra-high energetic cosmic rays [Aab15].

Supernova remnants

A Supernova remnant (SNR) is the classical example for shock acceleration. Supernovae are explosions of stars, caused by different reasons. While supernovae of type Ia are caused by a gravitational collapse of a white dwarf with about $1.4\,M_\odot$, depending on its composition, supernovae of type II arise when stars of about $8\,M_\odot$ up to $30\,M_\odot$ collapse. Stars with even higher masses end their lives as supernovae of type Ib or Ic [Jan11]. These star explosions cause shock waves, which might be able

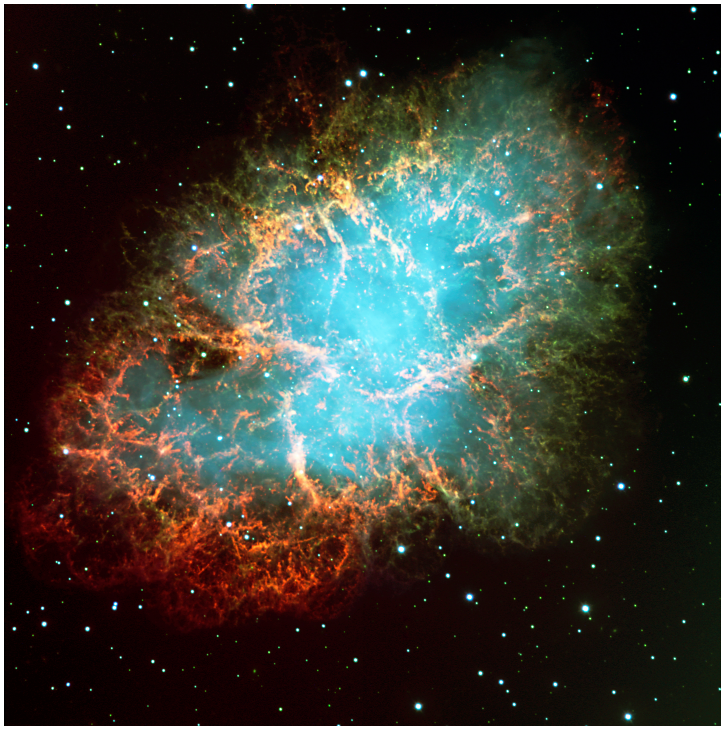

Figure 1.5.: The Crab nebula (composite image) as an example of a supernova remnant [ESO99].

to accelerate particles with the first order Fermi mechanism to a range of $10^{18}\,eV$ in case of a type IIb supernova. In two different SNR were characteristic gamma-ray spectra discovered by the Fermi Large Area Telescope, which might be originated by the decay of neutral pions produced while the interaction of accelerated protons with interstellar matter (ISM), which supports SRN as sources of cosmic rays [Gai16].

1.5. Composition

The knowledge of the composition of cosmic rays is fundamental to the understanding of their origins (compare sections 1.3 and 1.4). Due to the extreme low event rates, a direct measurement of the composition is only viable for the lower end of the energy spectrum.

1.5.1. Composition below 100 GeV

Determined from balloon or satellite mounted experiments the composition of cosmic rays below 100 GeV is well known.

98 % of the cosmic rays arriving at Earth at these energy ranges are hadronic, protons and heavier nuclei. Only 2 % are electrons and positrons (extracted from [Oli14]). The hadronic fraction consists mostly of protons (approx. 90 %), followed by Helium nuclei (approx. 9 %) [Gai16]. Only the remaining fraction is made of heavier elements. Despite their small fractions, all elements are present in cosmic rays and the abundances are – with a few exceptions – comparable to their relative abundances in the solar system, which is an indication for their origin in a stellar nucleosynthesis. The relative abundance of protons and Helium, the two lightest elements, is lower in cosmic rays than in the solar system. This is explained by their high ionization energy, which causes that these particles remain uncharged and cannot take part in acceleration mechanisms [Gai16].

Higher abundances, e.g. for Lithium, Beryllium, and Boron, can be explained by the fragmentation of heavier nuclei during their propagation to Earth [Gai16].

1.5.2. Composition at ultra-high energies

In energy domains, where a direct detection of cosmic rays is not feasible, the determination of the composition is one of the greatest challenges of modern astroparticle physics. Information on the composition at ultra-high energies is based on analyses of extensive air showers (see section 1.6). These analyses are based on the properties of air showers like X_{max}, which are mass dependent [Abr10], but also depending on hadronic interactions [Eng11]. This means that these observables – even for a pure composition with constant energy – are statistically distributed, therefore a single measurement cannot provide any precise information on the primaries mass.

By taking a whole dataset into account it is possible to make some qualitative statements, comparing the data with simulations. These simulations underlie several uncertainties originating from model assumptions used. One of these issues is the necessary usage of hadronic interaction models, which are based on accelerator data. Besides the uncertainties of these models, coming from the respective fit to the accelerator data, two other sources of uncertainties are important in the case of air shower simulations. As mentioned in section 1.2, today's available accelerator data cannot provide such an enormous center-of-mass energy as occurring in the collision of ultra-high energetic cosmic rays with atoms of the Earth's atmosphere. At this point, an extrapolation of the hadronic interaction model is needed in order to make a prediction of the behavior of hadronic interactions at these energies [Hec98].

Another impact gives the topology of the interactions. While almost all accelerator data at the highest achievable energies are produced using colliders, where two particles collide with nearly the same energy, the impact of a cosmic ray particle is comparable to a fixed-target experiment. This leads to an extreme forward boost of the system, which makes an extrapolation with associated uncertainties necessary [Hec98].

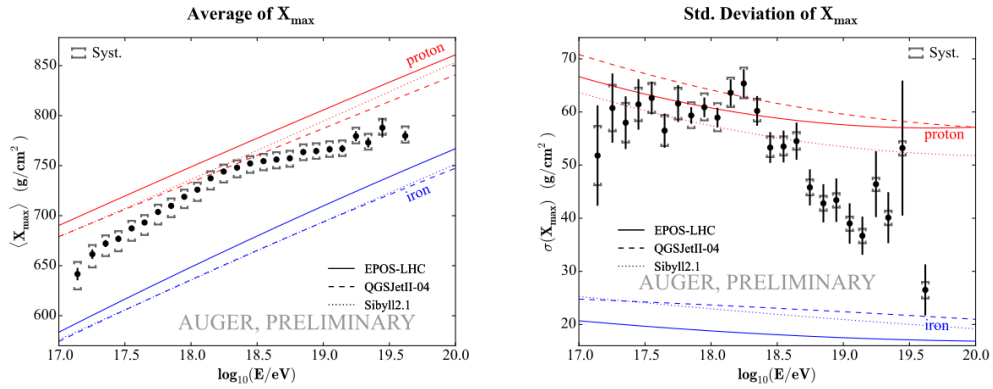

Figure 1.6.: $\langle X_{\mathrm{max}} \rangle$ and $\sigma_{X_{\mathrm{max}}}$ versus energy in the data of the Pierre Auger Observatory. The lines indicate the expectation from simulations with different interaction models [Plu].

Nevertheless recent measurements indicate a mixed composition even for highest energies. As shown in figure 1.6 neither the average X_{max} nor the X_{max} standard deviation are compatible to a pure and constant composition. The evolution of $\langle X_{\mathrm{max}} \rangle$ with energy shows a tendency to

heavier compositions for higher energies, while $\sigma_{X_{\max}}$ does not show such a clear tendency due to larger uncertainties [Plu].

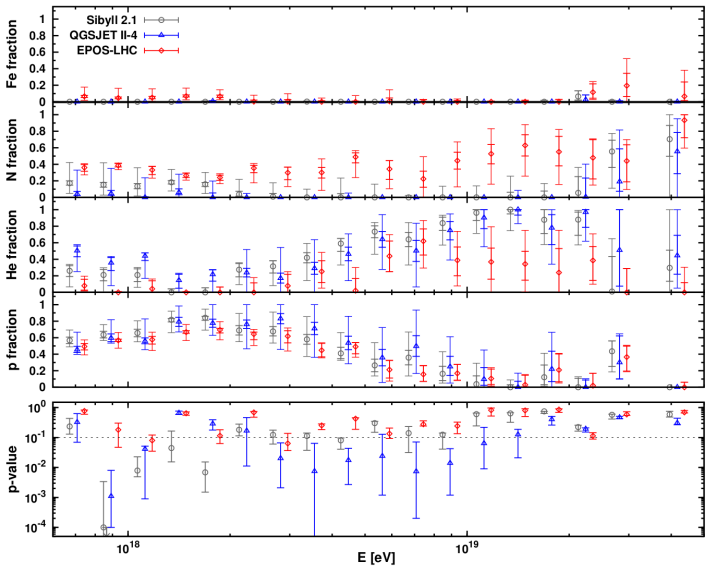

Figure 1.7.: The expected $X_{\max}$ distributions of four nuclei are composed to a total distribution and their weights are fitted to the data. The results of the derived experimental fractions are plotted versus the primary energy [Bel17].

A similar result shows figure 1.7, where the expected $X_{\max}$ distributions of four possible primaries were used to fit their relative abundances to match the resulting total distribution with the data. These results indicate a diminishing fraction of protons with increasing energy, while the fraction of heavier elements increases. But still, the existence of protons at highest energies cannot be excluded [Bel17].

While the data of the Pierre Auger Observatory gives indications for a mixed composition with increasing mass, the data of the HiRes, the High-Resolution Fly's Eye Experiment, shows indications of a constant proton dominated composition [Abb10]. This might be explainable due to different analysis procedures (compare [DS17]).

1.6. Extensive air showers

For the ultra high energetic regime the direct detection of cosmic rays is not suitable. Nevertheless, with the utilization of extended air showers, it is still possible to detect ultra-high energetic cosmic rays indirectly. Extended air showers occur when a high energetic cosmic ray particle hits the Earth's atmosphere.

An important observable of extensive air showers is the depth of the shower maximum. This observable is mostly measured using its atmospheric depth. In contrast to the height, the atmospheric depth takes into account the mass density profile of the atmosphere, which influences the distance between interactions within an air shower [Sta10].

In order to derive the atmospheric depth from the height one needs to know the density profile of the atmosphere. With this knowledge, one can derive the atmospheric depth X by integrating the density profile $\rho(h)$:

$$X = \int_H^\infty \rho(h) \mathrm{d}h, \tag{1.11}$$

where H is the height corresponding to the atmospheric depth X [Sta10]. For an inclined path it is necessary to modify the atmospheric depth to the slant depth X_{slant}

$$X_{\text{slant}} = \frac{X}{\cos \vartheta}, \tag{1.12}$$

where ϑ is the inclination of the path [Sta10], which holds true for zenith angles up to 60°.

1.6.1. Shower development

After the initialization of an extensive air shower by a primary particle, an avalanche of particles propagates through the atmosphere. The original energy of the cosmic ray particle is split to millions and millions of secondary particles. The process of producing more and more secondary particles differ from particle type to particle type. Since many particles behave similarly, one can differentiate between three components: The electromagnetic component – consisting of electrons, positrons, and photons –, the hadronic component – consisting of hadronic particles – and the muonic components – consisting muons and antimuons. The influence of the primary mass on the overall shower development will be discussed in chapter 3.

Electromagnetic component

The two main interactions for the development of the electromagnetic component are Bremsstrahlung

$$e^{\pm} + {}^{A}_{N}X \rightarrow e^{\pm} + {}^{A}_{N}X + \gamma$$

and pair production

$$\gamma + {}^{A}_{N}X \rightarrow e^{+} + e^{-} + {}^{A}_{N}X,$$

where ${}^{A}_{N}X$ denotes an arbitrary atom, in whose electric field these interactions take place. A simple approach for the description of the development of an electromagnetic cascade[1] gives the Heitler model [Mat]. Based on the two processed mentioned above, the Heitler model assumes a uniform distribution of the initial energy to the electromagnetic products and the same interaction length for both processes. With these simplifications, the number of particles after i generations is given by

$$N_i = 2^i, \tag{1.13}$$

the energy of these N_i particles is

$$E_i = \frac{E_0}{N_i} = \frac{E_0}{2^i}, \tag{1.14}$$

where E_0 is the energy of the initial particle. In the Heitler model, both processes will happen until the energy of the particles falls below a critical value E_c. Due to the even distribution of the energy,

$$i_c = \frac{\ln \frac{E_0}{E_c}}{\ln 2} \tag{1.15}$$

describes the maximum number of possible generations [Mat]. Therefore

$$N_{\max} = 2^{i_c} = \frac{E_0}{E_c} \tag{1.16}$$

Considering a depth of the first interaction X_0 and an interaction length of λ (given in units of atmospheric depth) the depth of shower maximum can be determined by

$$X_{\max} = \lambda \ln \frac{E_0}{E_c} + X_0. \tag{1.17}$$

[1] Which might be a component of an air shower or an independent air shower itself.

Besides the mentioned simplifications this model holds for pure electromagnetic showers. Since extensive air showers are mainly induced by hadronic particles, the electromagnetic component is fed by the decay products of the hadronic component. This leads to an overlap of many independent electromagnetic cascades, which makes a more detailed simulation of a real air shower unavoidable for a detailed understanding of the components' behavior [Mat].

Muonic component

Unlike the other shower components, the muonic component doesn't undergo many interactions. Fed by the hadronic component, the muonic component consists of muons.

Since the cross-section of neutrinos for any kind of matter is extremely small, they are mostly negligible for the shower development [Sta10], except for the amount of energy they carry. Detectors need to take this "invisible" energy into account when reconstructing the air shower's total energy, e.g. by introducing a correction factor (see section 2.5.1).

Even though muons have also a quite small cross-section for interactions with air, they are much easier to detect due to their charge. While low energetic muons mostly decay to electrons

$$\mu^{\pm} \rightarrow e^{\pm} + \nu_{\mu}(\bar{\nu}_{\mu}) + \bar{\nu}_{e}(\nu_{e})$$

with a lifetime of $\tau_{\mu} = 2.2\,\mu$s and feed the electromagnetic component, the higher energetic muons can reach ground level, due to relativistic time dilation. The number of muons in an air shower depends on its energy and the ratio of electrons to muons on the mass number of the primary particle[Gai16].

Hadronic component

In the hadronic component, the highest variation of particles occurs. The most common particles in the hadronic cascade are protons, neutrons, kaons, and pions, beside of many others that can occur. Apart from hadronic particles, this component produces even muonic and electromagnetic parts of the air shower, which behaves just like described in the prior paragraphs. This is due to the possible decay of hadronic particles in the air shower, e.g.

$$\pi^{\pm} \rightarrow \mu^{\pm} + \nu_{\mu}(\bar{\nu}_{\mu})$$

for a muonic product or

$$\pi^0 \rightarrow \gamma\gamma$$

for an electromagnetic product [Sta10].

Due to the variety of the particle types, it is not possible to describe every process as easily as for the electromagnetic component. But with some modifications, it is possible to adapt the Heitler model, described in the paragraph of the electromagnetic component, to the hadronic component. One possible modification of the Heitler model is adjusting the number of resulting particles after one interaction. This simplifies the complex processes of the hadronic particles to a single "interaction" producing a bunch of particles. Using only this modification the equations of the simple Heitler model can be reused by replacing the "2" by m, the number of shower particles produced in each interaction. Based on this modification, one can complexify the Heitler model, e.g. taking statistical fluctuations of the interactions into account (exponential distribution of the interaction length, instead of a constant one) [Mat].

1.6.2. Detection of air showers

Since cosmic rays pass through the whole atmosphere, it is possible to detect air showers with ground-based detectors. With these ground-based detectors, it is possible to counter the extreme low event rate of ultra-high energetic cosmic rays. In this section, some detection methods are presented briefly.

Cherenkov detectors

Cherenkov detectors are based on the Cherenkov effect. The Cherenkov effect describes the emission of light (more generally: electromagnetic waves) when a charged particle moves through a dielectric medium faster than light in this medium. While passing through this dielectric medium the charge of the particle causes a new orientation of the medium's molecules. This results in an electromagnetic wave, which forms a cone behind the charged particle. The opening angle of the cone can be determined geometrically, as shown in figure 1.8.

Based on the geometrical determination, the opening angle of the cone is given by

$$\cos\varphi = \frac{1}{\beta n}, \tag{1.18}$$

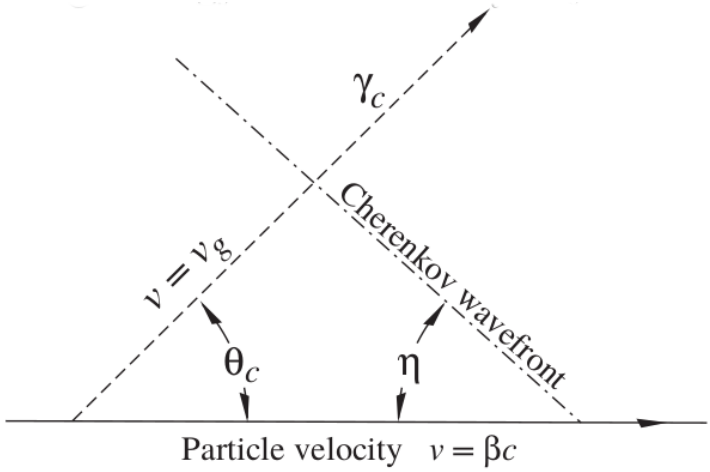

Figure 1.8.: Geometrical determination of the Cherenkov angle [Oli14].

where β denotes the speed of the particle in units of the speed of light in vacuum and n the refractive index of the medium [Oli14].

Due to the high amount of energy in an extensive air shower, many of its particles exceed the speed of light in the medium. Therefore the charged particles in an air shower emit Cherenkov radiation when hitting a Cherenkov detector. The produced Cherenkov light can be detected by light-sensitive detectors, like photo-multiplier tubes.

In principle, it is possible to utilize all transparent dielectric materials to build Cherenkov detectors. Maybe the most common material for this is water (or ice), due to the low price and the high availability. For Cherenkov detectors the energy threshold is given by

$$E_{\text{thres}} = m \cdot n \cdot \sqrt{\frac{1}{n^2 - 1}}, \tag{1.19}$$

where m is the mass of the charged particle in natural units [Oli14].

Utilizing this effect it is viable to build detector fields of Cherenkov detectors to detect the footprint of an extensive air shower. Since the footprints of air showers grows with their energy, the necessary density of detectors decreases with energy [Sta10].

Another use of Cherenkov light is the direct imaging of Cherenkov radiation, using telescopes. Using this technique the atmosphere's air is utilized and the Cherenkov cone is observed directly. Since the opening angle of the Cherenkov cone is quite narrow, the observing telescope

needs to directly look along the air shower's path [Gai16].

Examples for Cherenkov detectors are the SD component of the Pierre Auger Observatory (see chapter 2.1), the IceTop detector at the IceCube Neutrino Observatory [Abb13] for the detector field method or MAGIC [Lor04] for the direct imaging method.

Fluorescence detectors

Fluorescence detectors observe the atmosphere for the detection of air showers, utilizing the fluorescence light induced by the shower [Sta10]:

While passing through the air, the particles in the shower can excite the electrons of air's molecules (mainly Nitrogen). When these excited electrons fall back to their normal state, they emit fluorescence light. This emission is isotropic and occurs along the path of the air shower. In contrast to the direct Cherenkov imaging method the telescopes used for the fluorescence detectors just need to have the path of the air shower in their field of view due to the isotropy of the fluorescence light [Sta10].

Since the fluorescence light from extensive air showers is very weak, this method needs certain detection conditions, like low ambiance light [Sta10].

The emitted fluorescence light from nitrogen molecules is mainly in an ultra-violet band between 300 nm and 420 nm [Kei13].

Examples of detectors utilizing this effect are the FD component of the Pierre Auger Observatory (see section 2.2) or at the Telescope Array project [Kaw08].

Radio detection

Besides the emission of Cherenkov light and fluorescence light, electromagnetic radiation in other regimes is emitted as well, like radio waves. The main sources of radio waves in air showers are geomagnetic effects and charge excesses [Sta10].

Geomagnetic effects were caused by the influence of Earth's magnetic field, where the charged particles of an air shower can be deflected by the Lorentz force. Due to this deflection, an acceleration acts on the charged particles. This causes the particles to emit synchrotron radiation, which includes radiation in the radio band. At the same time, positive and negative charged particles were accelerated in different directions, which causes a charge excess. This forms a dipole moment within the air shower, which is another source of radiation in the radio band [Sta10].

Detectors utilizing this radio emission are the AERA extension of the Pierre Auger Observatory (see section 2.3.2) or LOPES at the former KASCADE Grande array [Sch13].

2 The Pierre Auger Observatory

One of the biggest challenges in astroparticle physics is the extremely diminishing rate of arriving cosmic rays towards ultra-high energies. The flux of cosmic ray particles above the energy of the ankle is at the order of one single particle per square kilometer and year. In order to obtain a viable amount of detected events in an experiment in an acceptable time the considered experiment needs to cover a huge area.

Presently the Pierre Auger Observatory [Pie96] is the largest observatory for extended air showers. It was proposed in 1991 by James Cronin and Alan Watson in order to improve the measurement of cosmic rays at highest energies. Originally there are two detector fields intended, one in the nothern hemisphere and one in the southern, covering an area of $5000\,\mathrm{km}^2$ each. However the plan for the nothern site was abandoned later on, while the design of the southern site was modified to a hybrid detector design, including the fluorescence detector component.

For the location of the (southern) site of the observatory a high plateau of the Pampa Amarilla in Argentina was chosen [The]. The construction started in 2001 near the town of Malargüe, province of Mendoza, Argentina and was finished in 2008, while the data acquision started in 2004 [Suo].

The southern site of the Pierre Auger Observatory uses two different types of detectors to measure extensive air showers [The]. Both detector types have their own advantages and disadvantages, but they deliver independent measurements of extensive air showers. Nonetheless both measurements can be combined e.g. to cross-calibrate both methods, which is one of the key features of the observatory.

2.1. The surface detector

The surface detector (SD) is a field of 1660 water Cherenkov detectors, which covers an area of roughly $3000\,\mathrm{km}^2$ [All08]. The detection principle is based on the Cherenkov effect. While passing through matter it might happen, that a particle's speed exceeds the speed of light in this medium [Che34]. If the particle is charged, it polarizes the medium around and emits a light cone of so-called Cherenkov light[1]. The en-

[1] A similar effect could take place with uncharged particles in a polar medium, the Askar'yan effect[Gor].

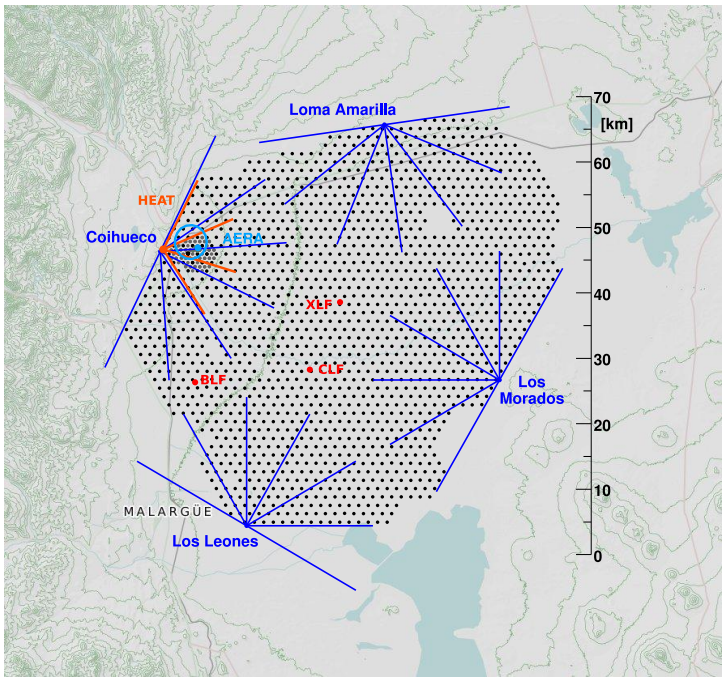

Figure 2.1.: Overview of the Pierre Auger Observatory [Veb13].

ergy threshold for the production of Cherenkov light in water (refractive index $n = 1.33$ [Lid03]) for muons is at $E_{\text{thres}} \approx 160\,\text{MeV}$.

2.1.1. Experimental setup

To utilize the Cherenkov effect the Pierre Auger Observatory uses $12\,\text{m}^3$ highly purified water per detector tank [All08]. Each tank has a diameter of 3.6 m and is made of polyethylene. To obtain guaranteed opaqueness, the inner side of the tank is black. Within the tanks there is an additional liner, which encloses the purified water. These liners prevent contaminations of the water, ensure additional light-proofness of the tanks and provide windows for the photo sensors. The insides of the liners have a diffuse reflective coating for an optimal detection of the Cherenkov light. This Cherenkov light is detected with three photo-multiplier tubes (PMTs) with a diameter of approximately 23 cm, which are symmetrically mounted at a distance of 1.2 m from the center of the respective tank. These PMTs amplify the incoming Cherenkov signal with $2 \cdot 10^5$ nominal gain [Suo09] and transmit it to a Flash Analog-to-Digital Converter (FADC), where the filtering and digitalization of signals are pro-

Figure 2.2.: This SD-Tank is placed in front of the main buildung of the Pierre Auger Observatory. It is not filled with water and has a window in the front to let visitors see the inside of a tank (Picture: private).

Figure 2.3.: Scenic view over the SD detector field, as seen from the Coihueco FD-site, showing the lined up SD tanks (Picture: private).

cessed with a rate of 40 MHz, which corresponds to a resolution in time of 25 ns [All08]. The now digitalized signal is then processed by a Field-Programmable Gate Array (FPGA). Within this processing the signals are tested whether they fulfill different trigger conditions (see section 2.1.2). If so, the traces of the corresponding signals and their time stamp are stored locally. The time stamp is provided by a Global Positioning System (GPS) device attached to each tank, which delivers a time resolution of 8 ns. The needed electrical power of 10 W in average is supplied by a solar panel and an attached battery, which can be recharged with the energy of the solar panel. The time stamp and the fullfilled trigger condition are transmitted via radio to the base station, running the Central Data Aquisition System (CDAS). With this setup, each of the 1660 tanks, which are deployed in an trigonal pattern with 1.5 km distance between the tanks, are completely autarkic from each other [All08]. With this spatial distance an air shower with a primary energy of 10^{19} eV would trigger five tanks on average. An exception to this spacing between the tanks lies in the field of view of the Coihueco FD-telescopes, where the spacing is shortened to 750 m on an area of 23.5 km^2 [Var13], the infill-array. Due to the shorter spacing, the infill-array has a lower threshold in energy to detect air showers, which is supported by HEAT (see section 2.3.1) and

part of AMIGA (see section 2.3.3).

One unit for displaying the signal of a single station, which may occur, is the Vertical Equivalent Muon (VEM), corresponding to the signal of a single muon (I^{peak}_{VEM} denotes the height of that signal peak), which passes the tank in its center vertically downwards, would induce. I^{peak}_{VEM} is estimated with a calibration process for each tank individually (see section 2.1.3) [Ber].

2.1.2. Data Acquisition

Before the collected data can be reconstructed the raw data has to pass five levels of triggers, to deliver high quality data[Abrb].

The first two trigger levels are implemented on the single station level. To pass the first trigger level (T1) the recorded data need to fulfill (at least) one of two different conditions. The first possible trigger is a simple threshold trigger (TH), wherein all three PMTs deliver a signal of $1.75 I^{peak}_{VEM}$ or higher coincidently in one bin in time. The second trigger type is a "time-over-threshold" trigger (ToT), where at least 13 time bins (corresponding to 325 ns) in a sliding time window of 3 μs need to exceed a signal of $0.2 I^{peak}_{VEM}$ in two of three PMTs coincedently. This second trigger type takes into account that the arrival time of the air shower's particles far from the shower axis is dispersed, same applies to not so inclined showers. The ToT-Trigger is also very effective in reducing the random muon background, since the average signal length of a single muon is approximately 150 ns. All data passing the T1 trigger is stored locally for 10 s, awaiting a possible T3 trigger [Abrb].

To pass the T2 trigger criterion the threshold for the TH-T1 trigger is increased to $3.2 I^{peak}_{VEM}$ and coincidence in all three PMTs. The T2 criteria for the ToT trigger is the same as for the ToT-T1 trigger, so that every ToT-T1 triggered signal triggers the T2. The occurence of a T2 together with the time stamp of occurence and its type is then sent to the CDAS.

With the collected data of all tanks the CDAS is able to apply the third-level trigger (T3) condition to the combination of the local triggers. Like on the trigger levels before, two modes of T3 triggers are implemented. The first mode applies only to ToT-T2 triggers. The so-called "ToT2C_1&3C_2" (C_n denotes the set of the n-th closest neighbours) is triggered if at least one of the closest and one of the second closest neighbours had also a ToT-T2 occurence within an appropriate time window. Since the ToT-T2 trigger filters background events very effictively,

the ToT$2C_1$&$3C_3$ delivers a very pure signal, where about 90 % of the T3 are actual real air showers and is most efficient for zenith angles below 60° [Abrb].

The second mode, called "$2C_1$&$3C_2$&$4C_4$", applies to both T2 triggers. This mode triggers, if at least one of the closest neighbours and one of the second nearest neighbours had also an T2 occurence. Additional a fourth tank at the maximum range of the fourth closest neighbours with a T2 occurence is needed to fulfill the condition. All four T2-triggered tanks need to have the T2 triggered in a time window, which implies coincidence. This trigger type works most efficent for horizontal showers, due to the permissivity of this trigger about 10 % are real air showers, though[Abrb].

If a T3 is triggered a signal is sent back to the stations. On the reception of this T3 trigger signal the T2 triggered tanks and those with T1 data within a 30 μs window arround the T3 transmit the still locally stored T1 data traces to the CDAS, where they are stored permanentely and can be analyzed. This procedure is necessary due to the limited bandwidth (approximately 1.2 kbit/s per tank) of the wireless communication. The necessary transfer rate is reduced that way to an acceptable value.

The fourth trigger level (T4) is the physics trigger, which is necessary to find the real air shower events in the stored T3 data set. Again, two different types of T4 triggers are implemented. The "3ToT" trigger aplies to the T3 events of type ToT$2C_1$&$3C_2$. To fulfill the 3ToT condition three ToT-T2 triggered tanks need to fit to a plane shower front moving the speed of light. The second mode, the "4C1", requires four nerby stations, which fit again to a plane shower front, which moves with the speed of light. This trigger is applied to the $2C_1$&$3C_2$&$4C_4$-T3, but accepts all T2-types for the nearby triggered tanks. Both T4 have a very high efficiency of > 98 % (3ToT) and ≈ 100 % (4C1) respectively [Abrb].

If an air shower only grazes the detector array at its border, a part of the shower remains undetected. Due to this lack of information the reconstruction machanism of the shower core position might fail and therefore delivers wrong shower energies. To prevent this a fifth trigger level is implemented. This fiducial trigger requires a full-functional hexagon (all six closest neighbours) arround the tank with the highest signal to ensure a correct reconstruction of the event. Including this trigger level reduces the effective area of the array by 19 %, which is also caused by non-functional tanks inside the array [Abrb].

2.1.3. Calibration

The recorded signals are depending on the exact tank properties, which are slightly varying from tank to tank, though. These small differences might be caused i.e. by differences in the optical couplings of the PMTs. In order to encounter these variations and remove the tank dependence of the signal, the tanks are calibrated utilizing the low energetic muon background. The obtained calibration values are permanentely monitored. By sending the calibration results to the CDAS even time depending changes, e.g. (seasonal) temperature changes, can be compensated [Abrb].

In order to correlate the size of the shower's footprint to its energy an advantage of the hybrid design is used: High quality hybrid events, which FD energy estimators could be determined without SD data, cross-calibrate the energy reconstruction of the SD. These events needs to pass very strict selection cuts, e.g. a good accuracy, a shower maximum in the field of view of the FD and clear atmosphere condition [Tue13, Pes11].

2.2. The fluorescence detector

At the perimeter of the SD array the four fluorescence detector (FD) stations are placed on small hills (see figure 2.4) [Abra]. At each of the sites six telescopes give an 180° in azimuth view over the SD field, so the FD component has 24 telescopes in total[2].

2.2.1. Detection principle

As the name indicates, the detection principle is based on fluorescence light. Charged particles of an extensive air shower can excite the nitrogen molecules of the atmosphere[3] while propagating through it. When these excited molecules de-excite, they emit photons. In the case of nitrogen these photons are in the ultra-violet regime with wavelengths between 300 nm and 430 nm. Since the fluorescence light emission induced by an extensive air shower has a very small intensity, it is necessary that the ambience is as dark as possible. Therefore the FD is only operational during the nights and only if the fraction of the moon illuminated is smaller than

[2] There are an additional three telescopes at the Coihueco site, refer to section 2.3.1

[3] Since the vast majority of the air's molecules are nitrogen, the other possible molecules are neglected.

Figure 2.4.: Outside view of the Coihueco FD station (Picture: private).

60 %, which leads to a duty cycle of the FD of about 13 % [Abra], which might be increased in the future by tweaking the cameras' electronics [Zor15].

2.2.2. Experimental setup

In order to minimize the amount of light beside the fluorescence light in the telescopes, each telescope has an UV filter with a transmission band of 290 nm to 410 nm in front of it. In addition, the aperture of the telescopes is increased by a corrector ring which is mounted in front of the UV filter. With this corrector ring the aperture increases by approximately a factor of two compared to the telescope without the ring.

Each of the 24 telescopes has a segmented mirror of approximately 13 m^2 reflective area. Twelve of these telescopes, located at the Los Leones and Los Morados sites, utilize 36 rectangular anodized aluminium mirror segments each. The other twelve telescopes at Coihueco and Loma Amarilla use 60 hexagonal glass mirror segments. This whole optical system focusses the incoming fluorescence light on a 440 pixel camera, localized at the focal plane of the telescope, arranged in a 22×20 matrix [Amb]. This geometry covers a total field of view of $30° \times 28.6°$. All pixels, which are hexagonal photo-multipliers, are held by a spherical aluminium shell. Between the single pixels a simplified version of the

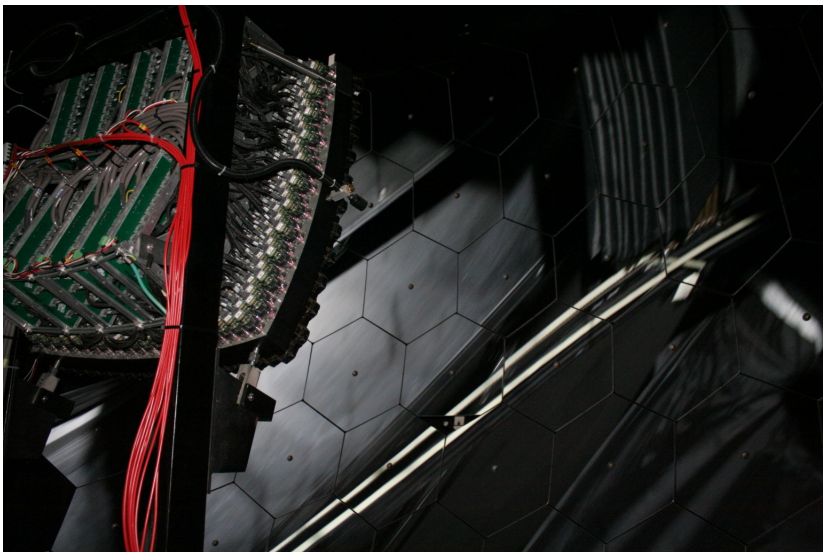

Figure 2.5.: The mirror of one FD telescope (right) at the Coihueco site and the photomultiplier camera on the upper left side (Picture: private).

'Winston cones' [Amb] is placed, to collect light at the border of the pixels and between them, to increase the effiency of light collection.

2.2.3. Data Acquisition

Due to the need of a dark sky, the fluorescence detectors collect data only in nights around new moon. The operators in these nights control the parameters of the telescopes separately and remotely from the central Auger building. Standard calibration processes are run at the beginning and the end of each night of operation, using standard light sources attached to each telescope [Abra]. After the standard calibrations the operator can open the shutters. In order to protect the optical system, the shutters stay closed if it is rainy, too windy or too bright at the FD site. If the conditions change during the night, the system automatically closes the bays.

Each telescope camera is connected to a "mirror PC" [Abra] via 20 front-end boards, one for each column. The first level trigger (FLT) is realized on this front-end board. The board contains two components: the analog board and the FLT module. The analog boards adapt to the dynamic range, adjust the gain and prepare the signal for the analog-

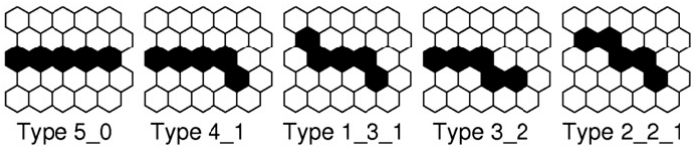

Figure 2.6.: The five standard patterns for the SLT. The orientation of these patterns is free and are also found if rotated or mirrored [Abra].

to-digital converter (ADC). After the digitalization of the signal of each channel the FLT board stores and processes this raw data for later access. The trigger condition of the FLT is a threshold cut. This pixel trigger is generated if the sum of the ADC signals of a single pixel in a certain time range exceeds the threshold, while the time range is adjustable to achieve a constant trigger rate of 100 Hz [Abra].

On the second level trigger (SLT) board all pixel triggers of the FLT are read out. In order to find the light traces of an air shower, the board searches for certain patterns of five pixels (figure 2.6) in a straight track. If the air shower trace does not hit the center of the pixels, it might not produce pixel triggers all along the way. Therefore and to be roboust to defect PMTs only four of five pixel triggers are sufficient to pass the SLT condition. The successful SLTs are stored togehter with the GPS timestamp.

This data is accessible for the mirror PCs, which are able to identify three different kinds of events.. There are external triggers, e.g. Laser shots of the central laser facility, and calibration events beside the real air shower events. The third level trigger (TLT) is designed to reject noise from direct muon hits and randomly triggered pixels as well as triggered pixels caused by distant lightnings. The efficiency of this algorithm depends on the weather conditions, but identifies about 94 % of the background events correctly while rejecting about 0.7 % of the real air shower data [Abra].

Events passing the TLT send a T3 trigger signal to the CDAS, which causes the SD component to collect data as described in section 2.1.2. The T3 orders the array to collect even data from low energetic air showers, which mostly would not trigger the SD T3. These low-energetic events may trigger single SD tanks, which can provide sufficient data for a good hybrid reconstruction.

2.2.4. Atmospheric Monitoring

The observation of air showers using the FD telescopes depends on the weather conditions on site: clouds may distort or block the flourescence light from the shower, the light might be reflected due to atmospheric distortions and the relation between altitude and atmospheric depth is varying, depending e.g. on air temperature or air pressure. These are some atmospheric factors which may lead to increased uncertainties on the air shower's observables[4]. In order to decrease the impact of these uncertainties, the atmospheric conditions of the observatory are monitored [Pie12]. Beside weather stations at all four FD sites and the central laser facility (CLF), the data of the **G**lobal **D**ata **A**ssimilation **S**ystem (GDAS) is used to reduce uncertainties on the observables. In addition, the average cloud fraction is determined at every FD site by an infrared camera.

The Lidar (**li**ght **d**etection **a**nd **r**anging) [Ben] system scans the atmosphere hourly during FD operation, utilizing backscattered laser light to detect whether there are clouds in the field of view of the telescopes and, if so, their ranges from the FD sites. Therefore all four FD stations are accompanied with a Lidar telescope (See figure 2.4, the small white building on the right side). During FD operation the incoming air shower is immediately and preliminary reconstructed. If a preliminary reconstructed air shower fulfills several conditions, the Auto-Scan of the Lidar system is interrupted and the "Shoot-the-Shower" (StS) program is initiated. The StS shall provide more detailed atmospheric information for these showers. Therefore the Lidar starts to scan the Shower-Detector-Plane[5] for clouds [Pie12].

The collected atmospheric data is afterwards used for a later reconstruction of the air shower data with reduced atmospheric uncertainties.

2.3. Other detectors at the Auger Observatory

Beside the two main components and the complementary systems of the Pierre Auger Observatory, there are other instruments present, which extend the functionality of the Observatory or test new detection principles. In this work, the **H**igh **E**levation **A**uger **T**elescopes (HEAT), the **A**uger

[4] Since some parts of the FD data are used to cross-calibrate the SD component, even the SD observables are subject to atmospheric variations.

[5] The plane spanned by the shower axis and the telescope. For more details see section 2.5.1.

Figure 2.7.: The HEAT telescopes at the Coihueco site in their upward tilted position (Picture: private).

Engeneering **R**adio **A**rray (AERA) and **A**uger **M**uons and **I**nfill for the **G**round **A**rray (AMIGA) will be presented exemplarily.

2.3.1. High Elevation Auger Telescopes (HEAT)

In addition to the standard FD telescopes at the Coihueco site there are three other telescopes, belonging to HEAT [Meu]. With the possibility to tilt the entire telescope housing up to an angle of 60° to the ground, HEAT is able to observe air showers in the upper atmosphere and small depths of shower maxima, which are not in the field of view of the standard FDs. This reduces the minimum air shower energy to be detected, since lower energetic cosmic rays produce showers with smaller depths of shower maximum than higher energetic ones. HEAT is therefore a low energy extension of the FD component with a primary energy threshold of 10^{17} eV [Meu]. The experimental setup of HEAT is basically the same as for the standard FD telescopes, with a few changes adapting to the special purpose: The most obvious difference is the light-weight construction of the HEAT housing. Each telescope has its own housing, which can be lifted by hydraulic stamps by an angle of 30°. HEAT is also operational in non-tilted position, which can be used for cross-calibration with the Coihueco FDs. Since lower-energetic air showers occur more often than

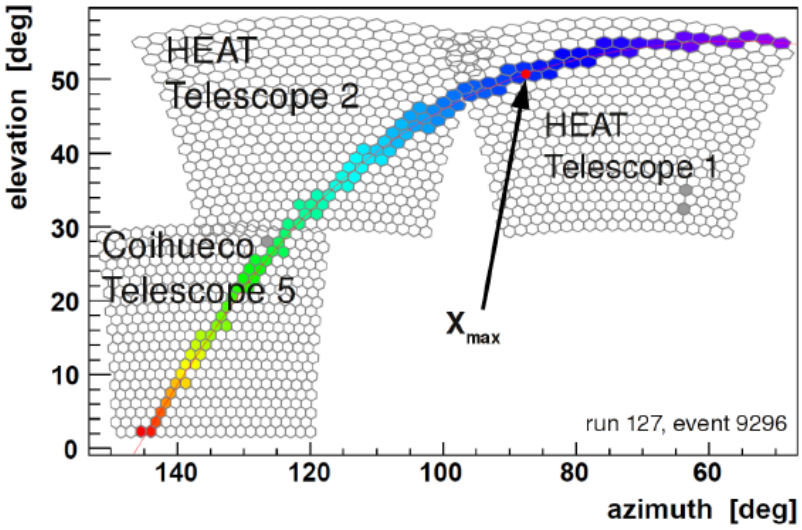

Figure 2.8.: An air shower event detected by one Coihueco telescope and two HEAT telescopes. The shower maximum (indicated with a red dot) was seen in HEAT 1 [Meu].

the higher energetic ones, the DAQ systems has been tweaked with an increased sampling rate.

In addition to the HEAT telescopes, the SD component has an smaller spacing – the so-called infill array – in an area near to Coihueco, which is able to reconstruct lower energetic air showers with smaller footprints.

Combining HEAT with the Coihueco telescopes may provide longer traces of air shower, as shown in figure 2.8. Such an event would be rejected by the standard FD analysis cuts, since the standard FD telescope was not able to see the shower maximum directly.

2.3.2. Auger Engineering Radio Array (AERA)

While propagating through the atmosphere, the particles of the extensive air shower emit electromagnetic radiation at several frequencies. The AERA extension at the Auger Observatory aims at radio emissions in the MHz regime [Fli]. Compared to other detection principles, the radio detection of air showers might be a very cost-efficient solution for air shower detectors in the future. The antennas used for radio detection are easier to deploy and very simple to build. The radio detection of air showers is sensetive to the shower maximum like the fluorescence detector, but has

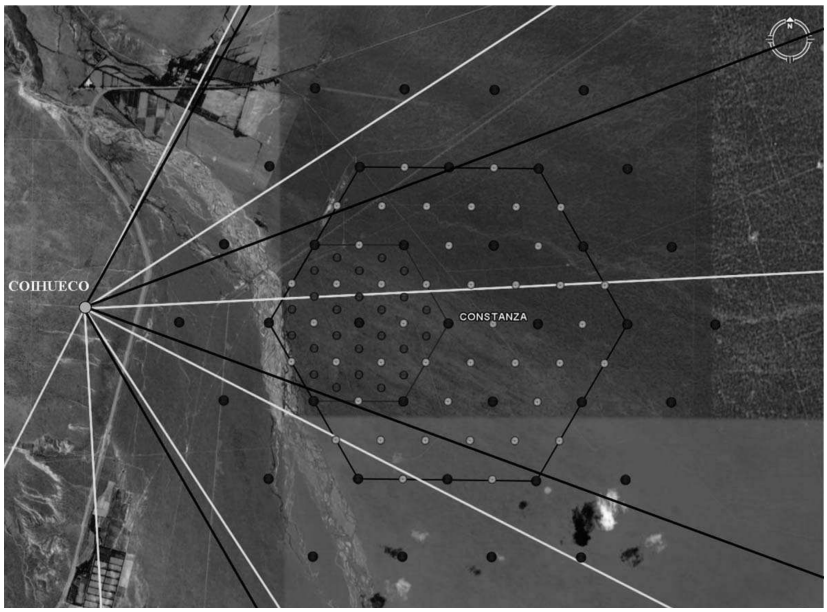

Figure 2.9.: Overview of the Amiga enhancement. Each dot represents a SD with buried muon counter, with different spacings [Var13].

no need for a dark ambient. Nevertheless such a radio detector needs a radio-quiet place to be self-triggered, since e.g. the transmission of the FM-radio broadcast interferes with the radio emission of air showers.

In order to proof the principle of radio detection, the AERA experiment built a $20\,\mathrm{km}^2$ radio antenna array within the SD field. Like the SD station, each radio station operates autarkic. The array is near the Coihueco FD station, so the radio-detected showers can be compared to the showers detected with the FD.

2.3.3. Auger Muons and Infill for the Ground Array (AMIGA)

AMIGA extends the infill array with a muon counter [Var13]. Shielded by $\sim 3\,\mathrm{m}$ of earth the $30\,\mathrm{m}^2$ plastic-scintillator detectors are able to count muons going through: The much higher cross-section of electrons and other electro-magnetic particles in matter causes a strong absorption of these particles, while muons pass through this matter nearly unaffected. The SD stations of the infill array are identical to those in the main array, except for upgraded electronics, which is capable to transmit the addi-

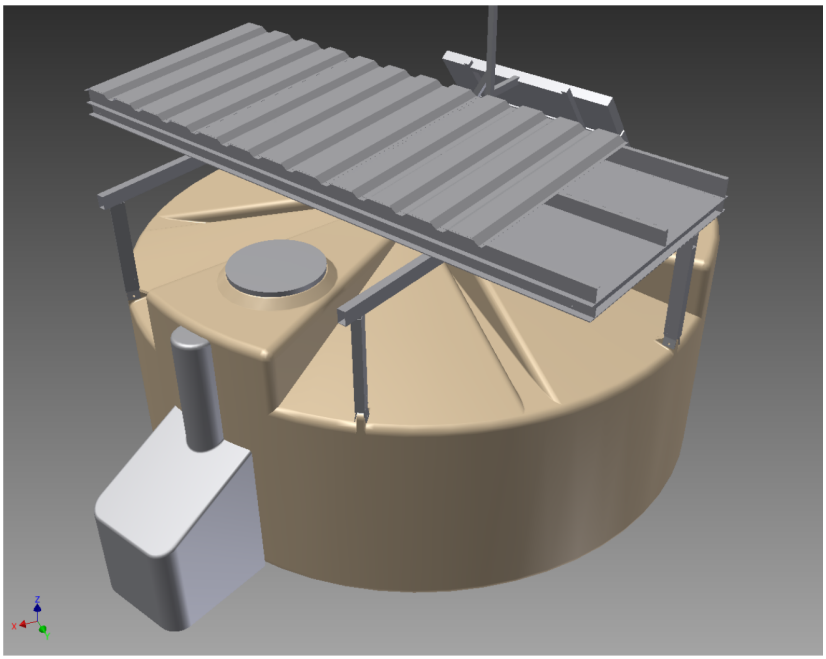

Figure 2.10.: A rendered picture of the new SSD component, mounted on an SD tank [Eng16].

tional data from the associated muon counter.

Since the muonic component of an air shower is depending on mass and energy of the primary cosmic ray, this gives the possibility to determine the composition of cosmic rays.

2.4. AugerPrime

In order to extend the possibilities of the existing detector, the observatory is currently upgraded. The AugerPrime project extends the existing SD tanks with an component based on scintillators, the **s**urface **s**cintillator **d**etector (SSD) [Eng16]. As shown in figure 2.10, the SSD unit, which is a box with two scintillation detectors of 1.9 m^2 area each, is mounted on top of the original SD tank. The scintillation light is lead to two photomultipliers with wavelength-shifting fibers. Additionally, the SD electronics are upgraded to adapt to the SSD module. This includes an increase of the SD sampling rate to 120 MHz, so both detectors are read out synchronously, since the SSD is triggered by the SD tank. With an additional small PMT in the SD tank, which is inserted to one of the

Figure 2.11.: The first deployed SSD on September 15 2016 with the deployment crew [SSD16].

filling ports, the dynamic range of the tank can be increased by a factor of 32. The first SSD module was installed in September 2016 (see figure 2.11).

Due to the different response of the SSD compared to the SD to the electromagnetic and muonic components of an air shower, it is in principle possible to separate between those with the combined data. This may be helpful to determine the composition of primary cosmic rays, since the ratio of number of electrons and muons in an air shower is a mass-sensitive observable.

2.5. Air shower reconstruction

If recorded data passes all trigger conditions the air shower event is reconstructed. In this section, the method of reconstruction is described.

As mentioned in the beginning of this chapter, the measured data of FD and SD can be combined in a hybrid reconstruction. In the case that an air shower passes all trigger levels of both detectors, a full reconstruction in SD and FD is possible. These "golden" hybrid events deliver important information to cross check SD and FD and are used to determine the

energy scale of the SD using the FD energy reconstruction. But even if an FD event did not pass all SD triggers, the hybrid trigger of the FD system records the SD data, even if only a single tank detected a signal.

2.5.1. Hybrid reconstruction

The hybrid reconstruction is mainly based on the data of the fluorescence telescopes with the addition of the timing information of the triggered SD tanks.

The first step is the determination of the shower-detector-plane (SDP), which includes the shower axis and the detecting FD telescope [Pie15b]. The SDP is determined by minimizing

$$S = \frac{1}{\sum_i q_i} \sum_i q_i \left(\frac{\frac{\pi}{2} - \arccos\left(\vec{p}_i \cdot \vec{n}_\perp^{\,\mathrm{SDP}}\right)}{\sigma_{\mathrm{SDP}}} \right)^2 , \tag{2.1}$$

where q_i is the integrated signal of the respective pixel, $\vec{p}_i$ the pointing direction of this pixel and $\vec{n}_\perp^{\,\mathrm{SDP}}$ is the normal vector in spherical coordinates of the SDP, defined by two free parameters θ_{SDP} and ϕ_{SDP} [Pie15b]. σ_{SDP} is determined through measurements of laser shots from the CLF with known geometry and was determined as $\sigma_{\mathrm{SDP}} = 0.35°$. Since the S function is normalized, it is interpreted as a χ^2 function, whereas the uncertainties of the fit parameters can be determined with $S + 1$.

Afterwards the angular movement is determined by another χ^2 minimization, which uses the timing information from the surface detector as well. The angular movement with respect to the horizontal axis of the telescope can be represented by

$$t(\chi_i) = T_0 + \frac{R_p}{c} \tan\left(\frac{\chi_0 - \chi_i}{2}\right). \tag{2.2}$$

The three free parameters – the time of the closest approach T_0, the minimum distance to the telescope R_p and the angle of the shower axis to the horizontal axis of the telescope χ_0 [Por70] – can be obtained by minimizing

$$\chi^2 = \sum_i \frac{(t_i - t(\chi_i))^2}{\sigma(t_i)^2} + \frac{(t_{\mathrm{SD}} - t(\chi_{\mathrm{SD}}))^2}{\sigma(t_{\mathrm{SD}})^2}, \tag{2.3}$$

summed over all pulses with the centroid pulse time t_i and the corresponding uncertainty $\sigma(t_i)$, adding the timing information of the SD t_{SD} with uncertainty $\sigma(t_{\mathrm{SD}})$.

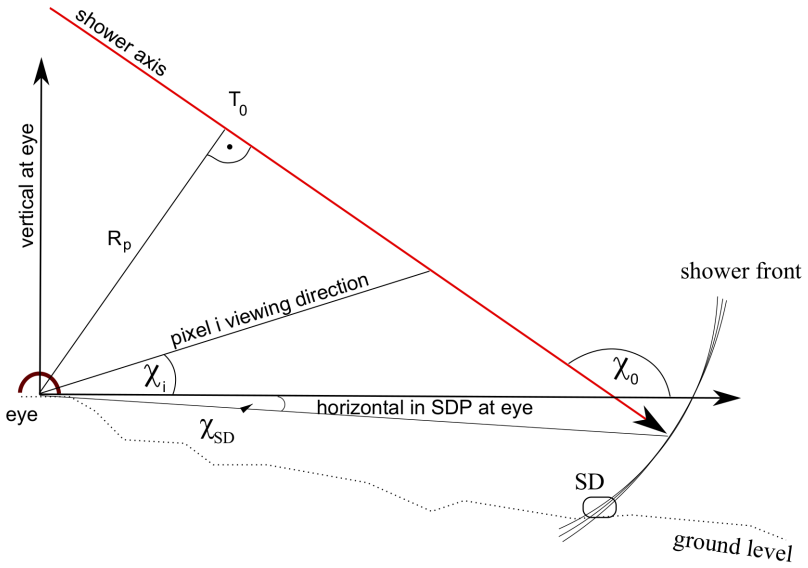

Figure 2.12.: Schematic sketch of the fit parameters for the angular movement [Pie15b].

The next step, which is necessary to reconstruct the air shower's profile, is the calculation of the total light at the aperture [Pie15b]. This is achieved by

$$F_i = \frac{1}{A_{\text{dia}}} \sum_{j=1}^{N_{\text{pix}}} s_{ij}, \tag{2.4}$$

where A_{dia} is the area of the opening of the diaphragm, s_{ij} the signal in the j-th pixel in time bin i, where j is running over all pixels N_{pix} within a certain angular distance to the vector from telescope to shower center, where the signal-to-noise-ratio is maximized.

With these geometry informations and the reconstruction of the light collected at the aperture as a function of time, one is able to reconstruct the profile of the shower, which is the deposited energy as a function of slant depth. After converting the light at the aperture and the shower geometry to the deposited energy and slant depth a Gaisser-Hillas-function [Gai77]

$$f_{\text{GH}}(X) = \left(\frac{\mathrm{d}E}{\mathrm{d}X}\right)_{\text{max}} \left(\frac{X - X_0}{X_{\text{max}} - X_0}\right)^{(X_{\text{max}} - X_0)/\lambda} e^{(X_{\text{max}} - X_0)/\lambda} \tag{2.5}$$

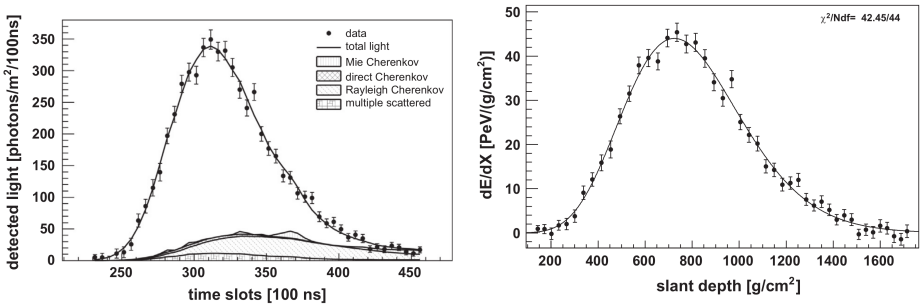

(a) Light at aperture for an example shower...

(b) .. and its deposited energy and reconstructed shower profile.

Figure 2.13.: Example FD measurement with profile reconstruction [Pie15b].

is fitted to the data to determine depth of shower maximum $X_{\max}$. As a final step the integration of the f_{GH} profile, corrected for "invisible energy" (e.g. neutrinos or high energetic muons), delivers an estimator for the shower's energy E_0, using the calibration of the detector [Pie15b].

2.5.2. SD reconstruction

With the determination of the size of an air shower on the ground and the measurement of the time the signal was detected, it is possible to reconstruct the energy and the arrival direction [Pie15b].

After passing all five trigger levels described in section 2.1.2[6] the arrival direction of the shower can be determined from the signal timing. A simple but rough estimation can be done under the assumption of a plane shower front trajecting with the speed of light. A more detailed approach uses an inflating sphere, which can be described with

$$c_0 \cdot (t_i - t_0) = \left|\vec{x_0} - \vec{x_i}\right|, \tag{2.6}$$

where t_i and $\vec{x_i}$ are the time and position of the i-th triggered tank and t_0 and $\vec{x_0}$ describing a virtual origin of the shower. As mentioned, equation 2.6 gives only a rough estimate of the shower's arrival direction, nevertheless one can utilize this fit to determine the radius of curvature of the shower front.

[6] For some analyses the T5 trigger might be relaxed to increase statistics, e.g. for arrival-direction studies [Pie15b].

The impact point of the air shower on the ground $\vec{x}_{\mathrm{gr}}$ is determined in a second step, in which a lateral distribution function (LDF) is fitted to the stations' signals. For this purpose a modified Nishimura-Kamata-Greisen function [Pie15b]

$$S(r) = S\left(r_{\mathrm{opt}}\right) \cdot \left(\frac{r}{r_{\mathrm{opt}}}\right)^{\beta} \cdot \left(\frac{r + r_1}{r_{\mathrm{opt}} + r_1}\right)^{\beta+\gamma} \tag{2.7}$$

is used, where r_{opt} is the optimum distance, which is determined to be 1000 m [NEW07], $r_1 = 700\,\mathrm{m}$ and $S\left(r_{\mathrm{opt}}\right) = S(1000)$ is a shower size estimator. The parameter β depends on shower size and zenith angle of the shower, since very inclined showers developed further compared to not inclined ones. For an analysis using showers with only three triggered stations, one can fix β and γ using an parametrization obtained from showers with four or more triggered tanks.

The main uncertainties for this reconstruction of $S(1000)$ and $\sigma_{S(1000)}$ come from the shower-to-shower fluctuations, which contribution is constantly about 10 %, the properties of the SD – ability to detect only finite number of particles, limited dynamic range – as well as an uncertainty due to assumptions of the lateral distribution's properties, both summing up to 6 % at highest energies to 20 % for low energies[Pie15b].

The point of impact $\vec{x}_{\mathrm{gr}}$ can now be determined by triangulation using the r_i. Using this, the arrival direction can be determined with the virtual shower origin from the first step:

$$\hat{a} = \frac{\vec{x}_0 - \vec{x}_{\mathrm{gr}}}{\left|\vec{x}_0 - \vec{x}_{\mathrm{gr}}\right|}. \tag{2.8}$$

The angular resolution depends on the shower's inclination and number of triggered tanks and is smaller than 1.6° for three triggered tanks and smaller than 0.9° for six or more triggered tanks [BON09].

Since the signal measured in the tanks is attenuating with increasing inclination the reconstructed $S(1000)$ value is normalized to a median angle of $\bar{\theta} = 38°$, using the Constant Intensity Cut (CIC) and a third degree polynominal in $x = \cos^2\theta - \cos^2\bar{\theta}$ named $f_{\mathrm{CIC}}(\theta)$. This gives

$$S_{38} = \frac{S(1000)}{f_{\mathrm{CIC}}(\theta)}. \tag{2.9}$$

Using the cross-calibration with the FD, described in 2.1.3, the energy can be determined via

$$E_{\mathrm{SD}} = A \cdot (S_{38}/\mathrm{VEM})^B, \tag{2.10}$$

where A and B are calibration constants, determined from the cross calibration, and S_{38} given in units of VEM.

The energy resolution of the reconstruction of the SD component is between $\frac{\sigma_{E_{\mathrm{SD}}}}{E_{\mathrm{SD}}} = (16 \pm 1)\,\%$ for lower energies and $\frac{\sigma_{E_{\mathrm{SD}}}}{E_{\mathrm{SD}}} = (12 \pm 1)\,\%$ at the highest energies [Pie15b].

3 Description of method

The main obstacle for determining the primary composition is the uncertainty from high-energy hadronic interactions. The aim of this work is drawing conclusions about the primary composition that are solid, as much as possible, with regard to this uncertainty. Thus, it takes a look at methods and observables with a reduced sensitivity to details of the hadronic interactions, even if the price to pay is access to only certain aspects of the primary composition instead of getting the "complete" (but uncertain) picture. Examples of such approaches are (1) the elongation rate, which indicates any changes in the composition with energy (for a division into light / heavy elongation rate, see [Och14]); (2) the correlation of X_{max} and S_{1000}, which indicates the purity of the composition at a given energy [You12, Ris14b]; (3) the exponential slope of the tail of the X_{max} distribution, which can indicate the ratio of the proton-to-helium abundances [Wer14, Ris14a].

3.1. Specific Motivation: Lorentz invariance violation

Instead of the determination of the overall composition of cosmic rays, as mentioned in section 1.5, this work focusses on checking for the existence of a specific particle species, namely protons. This knowledge can be useful and sufficient for some analyses. One of these applications shall be discussed here briefly.

Since there are many open questions, which still cannot answered by the standard model of particle physics, there are many theories trying to extend standard model theories. One of these theories questions the Lorentz invariance by introducing Lorentz invariance breaking processes in the photon sector. This is achieved by the introduction of an additional Lorentz violation tensor to the standard model's action

$$\mathcal{S}_{\mathrm{modM}} = \int_{\mathbb{R}^4} \mathrm{d}^4x \left(-\frac{1}{4} (\eta^{\mu\rho}\eta^{\nu\sigma} + \kappa^{\mu\nu\rho\sigma}) F_{\mu\nu}(x) F_{\rho\sigma}(x) \right), \tag{3.1}$$

where $F_{\mu\nu}(x)$ is the standard Maxwell field strength, $\eta^{\mu\nu}$ the metric of a Minkowski spacetime and $\kappa^{\mu\nu\rho\sigma}$ is the Lorentz violating tensor. This Lorentz violating tensor has 19 independent components and all of the

components are assumed to be very small $|\kappa^{\mu\nu\rho\sigma}| \ll 1$, which is necessary for energy positivity[Kli].

Ten of these parameters would lead to a birefringence of the vacuum and are bounded to a 10^{-32} or better level by lab experiments. The eight of the remaining nine components are non-isotropic, which can lead to a directional dependence of the phenomelogy of this theory. These nine components can be rewritten as a vector in an $\mathbb{R}^9$ parameter space

$$\vec{\alpha} \equiv \begin{pmatrix} \alpha^0 \\ \alpha^1 \\ \alpha^2 \\ \alpha^3 \\ \alpha^4 \\ \alpha^5 \\ \alpha^6 \\ \alpha^7 \\ \alpha^8 \end{pmatrix} \equiv \begin{pmatrix} \tilde{\alpha}^{00} \\ \tilde{\alpha}^{01} \\ \tilde{\alpha}^{02} \\ \tilde{\alpha}^{03} \\ \tilde{\alpha}^{11} \\ \tilde{\alpha}^{12} \\ \tilde{\alpha}^{13} \\ \tilde{\alpha}^{22} \\ \tilde{\alpha}^{23} \end{pmatrix}, \tag{3.2}$$

where α^0 is the isotropic parameter[Kli]. In the case of a positive scale, which is derived from these nine components (for details see references 12, 26, 27, 28, 29 of [Kli]), high energetic particles can produce cherenkov radiation above a certain energy threshold in the vacuum, which would lead to an extreme energy loss above this energy threshold within very short distances[Kli].

This energy threshold depends on the values of $\vec{\alpha}$. Therefore it is possible to give an upper limit on the non-birefringent parameters by determine the energy and mass of an ultra-high energetic particle using

$$R\left(\alpha^0 + \alpha^j \hat{\mathbf{q}}^j_{\text{prim}} + \tilde{\alpha}^{jk} \hat{\mathbf{q}}^j_{\text{prim}} \hat{\mathbf{q}}^k_{\text{prim}}\right) \leq \left(\frac{m_{\text{prim}} c_0^2}{E_{\text{prim}}}\right)^2, \tag{3.3}$$

where j and k are summed over 1 to 3[1], $R(x) \equiv \frac{x+|x|}{2}$ is a ramp function, $\hat{\mathbf{q}}^j_{\text{prim}}$ is the direction of a cosmic ray particle and m_{prim} and E_{prim} its mass and energy[Kli].

Assuming that α^0 is the only non-zero component of $\vec{\alpha}$ equation 3.3 simplifies to

$$\alpha^0 \leq \left(\frac{m_{\text{prim}} c_0^2}{E_{\text{prim}}}\right)^2. \tag{3.4}$$

[1]The remaining components of $\tilde{\alpha}^{jk}$ are given, since $\tilde{\alpha}^{jk}$ is symmetric and traceless, particular $\tilde{\alpha}^{jk} = \tilde{\alpha}^{kj}$ and $\tilde{\alpha}^{33} = -\tilde{\alpha}^{11} - \tilde{\alpha}^{22}$[Kli].

Symbol	Meaning
p_1^{He}	single event, using ($X_{\mathrm{max}}^{\mathrm{obs}}$, E^{obs})
p_N^{He}	penalized for N events in the set, using (X_{max}^{obs}, E^{obs})
$p_{1,\Delta}^{\mathrm{He}}$	single event, accounting for sys.+stat. errors
$\min_i(p_{1,\Delta}^{\mathrm{He}})$	single event with the smallest probability in energy bin i
$P_{1,i}^{\mathrm{He}}$	single event, dedicated simulation for candidates in bin i
$P_{N,i}^{\mathrm{He}}$	penalized for N events in bin i
P_i^{He}	penalized for N_{bins}

Table 3.1.: Probabilities for helium nuclei to produce a shower with $X_{\mathrm{max}} \geq X_{\mathrm{max}}^{\mathrm{obs}}$.

Using this equation, it is possible to determine a new upper limit on the isotropic Lorentz invariance violation parameter with the measurement of a single ultra-high energetic particle with known mass.

3.2. Brief descreption of main idea

In this work, the focus is on a method to test the existence of light primaries by using just one event (the deepest) and calculating the probability of the hypothesis that this certain event was induced by a Helium primary. In case of a small helium probability, the existence of particles lighter than helium is suggested at this energy.

This is based on the mass dependency of the position of the shower maximum. The lighter a particle the more likely a deep shower is induced. In this approach particles heavier than Helium would end up giving higher Helium probabilites by trend. So, if the probability for Helium is very small, even all heavier particles can be excluded. It should be noted that a relatively large helium probability does not automatically imply a complete absence of lighter particles, though perhaps one could think about placing an upper limit.

3.3. Properties of X_{max} distributions

For the reader's convenience designations of the helium probabilities introduced in the following are summarized in table 3.1.

In order to exclude primary cosmic rays heavier than protons the presented method utilize the distribution of the depth of shower maxima.

The dependencies of $X_{\max}$ can be predicted in detailed simulation studies (e.g. [Dom]) and observations (compare section 1.5 and figure 1.6), based on different interaction models and shall be presented here.

This work uses the parameterizations of $X_{\max}$ distributions with the generalized Gumbel function [Dom]:

$$\mathcal{G}(X_{\max}|E,A) = \frac{1}{\sigma}\frac{\lambda^{\lambda}}{\Gamma(\lambda)} e^{-\lambda z - \lambda e^{-z}} \quad \text{with } z = \frac{X_{\max}-\mu}{\sigma}, \tag{3.5}$$

here μ, σ and λ are the functions of the energy E and of the mass number A of the primary particle.

3.3.1. Energy dependence of the $X_{\max}$distribution

As implicated by the simple Heitler model (compare section 1.6.1) the depth of the shower maximum depends on the energy of the primary cosmic ray particle. The increased number of possible interactions with increased energy, described in section 1.6.1, is the main source of this ability.

Figure 3.1 shows several $X_{\max}$distributions with different energies for the same primary and interaction model. Besides the tendency to pro-

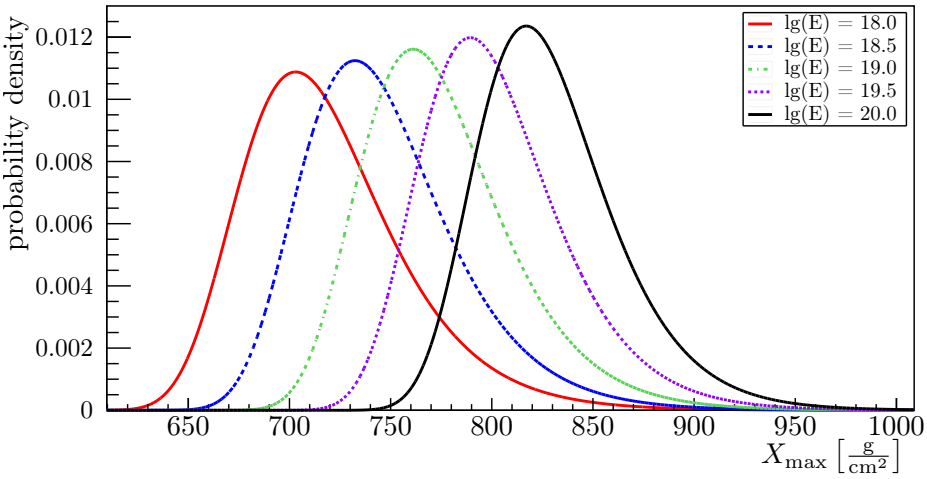

Figure 3.1.: Predicted $X_{\max}$distributions from [Dom] for Helium primaries ($A = 4$) and the EPOS-LHC [Pie15a] interaction model at varying energies.

duce deeper shower maxima with increasing energy, also the size of the fluctuations decreases, which is visible in the height of the distribution's maxima. This can be explained with the increased number of particles in the shower, since the fluctuations to different directions (lower or higher depth) cancel each other.

3.3.2. Mass dependence of the X_{max}distribution

As already mentioned the depth of the shower maximum is a mass sensitive measure. Therefore the distribution of the shower maximum's depth depends on the primaries mass. In contrast to the energy dependence, the depth of the shower maximum decreases with an increasing mass of the primary at constant energy. This is related to the depth of the first interaction or penetration depth, commonly referred to X_1[Gai16]. The cross-section of primary-air interactions is growing with the mass number. Therefore the probability of an interaction at very low depths increases, which leads to an earlier shower development.

Figure 3.2 shows the predicted X_{max}distributions for several primaries at constant energy and a single interaction model. Differences in the width of the distributions are visible again. The smaller variations of heavier primaries originate from their increased cross-section with air and therefore increased interaction probability.

The fact that lighter primaries tend to produce deeper shower maxima will be utilized for this work: If the probability of a certain primary to produce a shower with an observed depth or even deeper is extremely small, then one can exclude this and heavier particles, since they would be even more unlikely to produce such deep shower maxima, up to a certain confidence level as primary.

3.3.3. Influence of hadronic interaction models

For the study of air shower simulation the impact of hadronic interaction models can not be neglected. As mentioned in section 1.5 hadronic interaction models are tuned to fit to the available data from accelerators and are extrapolated for the use of air shower simulations. Since every interaction model is focussed to fit different feature of the accelerator data best, their extrapolation for air shower simulations behaves similar but not same. This is shown in figure 3.3 for three interaction models:

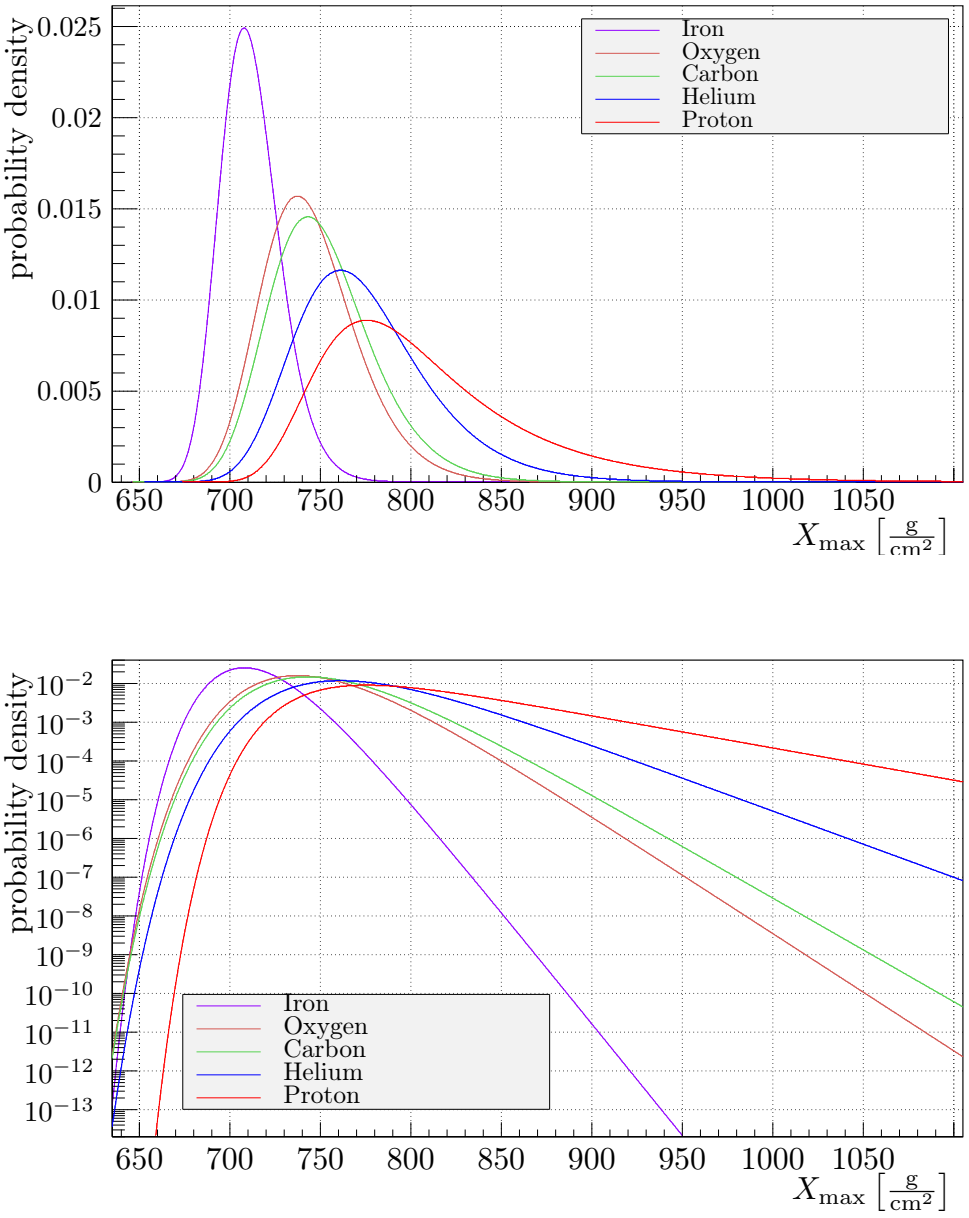

Figure 3.2.: Gumbel parameterizations [Dom] of $X_{\max}$ distributions for different primary nuclei for EPOS LHC at 10^{19} eV on linear (top) and log (bottom) scales. See appendix A for integrated distributions.

QGSJet II-04[Ost11], Sibyll 2.1[Ahn09][2] and EPOS-LHC. The general behavior of the distribution doesn't change with an exchange of interaction models: The average depth of shower maximum increases with decreasing mass.

Comparing the three interaction models the EPOS-LHC model produces the deepest showers on average, while QGSJetII-04 has the lowest average shower maximum's depth, but the largest spread. For very deep showers the picture changes for Helium, where the EPOS-LHC model has a lower chance than QGSJetII-04 and Sibyll 2.1 to produce a very deep shower.

3.4. Helium probability as a measure for lighter primaries

As shown in section 3.3.2 air showers tend to have a deeper shower maximum the lighter the primary cosmic ray is[3]. Using this information the probability of a Helium primary can be used to exclude Helium or heavier primaries for single events to a certain confidence level.

Possible candidates for an air shower's primary need to be stable, since the sources of ultra-high energetic cosmic rays are distant and the particle need to survive to earth. Therefore only a few particles lighter than helium are reasonable candidates, namely protons (Hydrogen nuclei) and photons. Recent researches were not able to confirm the existence of ultra-high energetic photons (compare e.g. [Nie15]). Based on this it is assumed that photons do not exist at these energies. Therefore the only remaining candidate particle is the proton. In this conservative approach events found by the presented method will be considered as proton candidates[4].

In this section, the basic method for the exclusion of heavy – in the sense of Helium or heavier – primaries is developed and presented. Af-

[2] Sibyll 2.1 has already been updated to version 2.3[Rie15], which includes latest LHC data. Since there is no parametrization of the Gumbel distribution for Sibyll 2.3 yet, version 2.1 is used as example. QGSJet II-04 and EPOS-LHC already includes LHC data.

[3] In fact, the lighter non-hadronic electrons produce very high shower maxima, due to the fact that QED processes are dominant in electron-induced showers (compare section 1.6.1)

[4] In the case that photons are found at ultra-high energies, one need to find a possibility to exclude photons as well, e.g. by comparison of the muonic component.

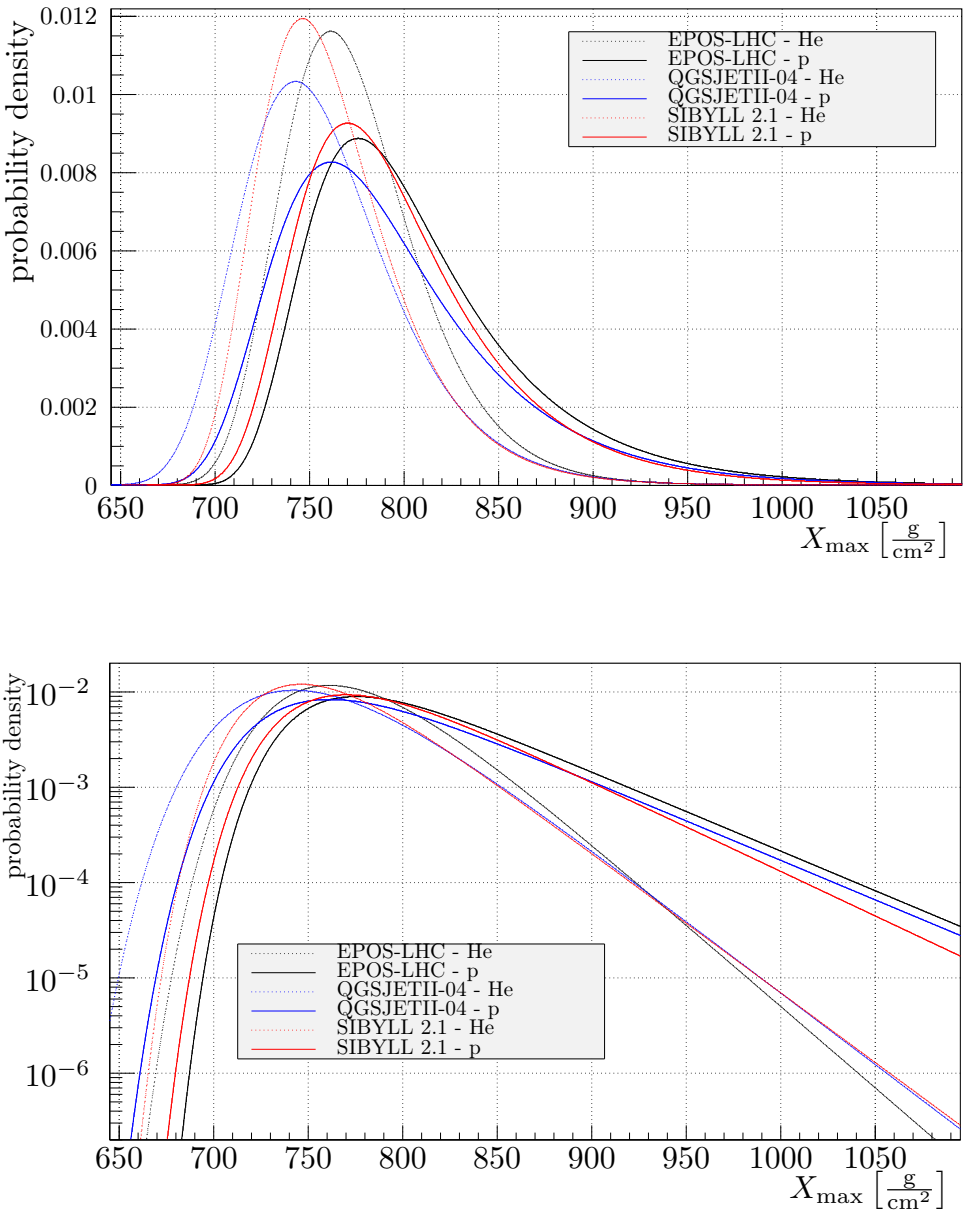

Figure 3.3.: Gumbel parameterizations of $X_{\max}$ distributions for protons and helium for different interaction models at 10^{19} eV on linear (top) and log (bottom) scales.

terwards, a simulation study shows the properties of the developed measure and its ability to potentially identify protons.

3.4.1. Single event probability

For an observed air shower of energy E^{obs} with a depth of the shower maximum $X_{\mathrm{max}}^{\mathrm{obs}}$, the probability for a single helium nucleus of energy E^{obs} to induce a shower with $X_{\mathrm{max}}^{\mathrm{obs}}$ or deeper is

$$p_1^{\mathrm{He}}\left(X_{\mathrm{max}} \geq X_{\mathrm{max}}^{\mathrm{obs}} \middle| E = E^{\mathrm{obs}}, A = 4\right) = \int_{X_{\mathrm{max}}^{\mathrm{obs}}}^{\infty} \mathcal{G}(X_{\mathrm{max}}|E,A)\,\mathrm{d}X_{\mathrm{max}}, \tag{3.6}$$

where $\mathcal{G}(X_{\mathrm{max}}|E,A)$ is a parametrization of the X_{max} distribution using the Gumbel function [Dom]. Calculation of p_1^{He} is a first step in the analysis and will be performed for each detected event. With this measure, one is able to determine the probability of a single Helium primary to induce a shower with the observed depth or even deeper. If this probability is small the hypothesis of a Helium primary might be rejected. From equation (3.6) it is seen that the tails of the p_1 distributions should follow the exponential behavior of the tails of X_{max} distributions:

$$p_1\left(X_{\mathrm{max}} \geq X_{\mathrm{max}}^{\mathrm{obs}} \middle| E, A\right) \sim \exp(-X_{\mathrm{max}}^{\mathrm{obs}}/\Lambda_A). \tag{3.7}$$

For large X_{max} values helium probabilities dominate among all other non-proton primaries (compare figure 3.2) and to confirm the presence of protons in the primary beam on the basis of the observation of the deepest shower one needs to demonstrate that the probability for it to be produced by helium is small.

3.4.2. Multiple event probability

In more realistic situations one needs to have an estimation of the probability for a given sample of the events, generally speaking with the unknown mass composition. In the most conservative approach one should assume 100% helium composition for setting the upper limit on the probability, since any admixtures of heavier elements can only decrease that limit. For a helium sample ($A = 4$) of N events with the energy E a probability to produce n showers with $X_{\mathrm{max}} \geq X_{\mathrm{max}}^{\mathrm{obs}}$ is given by a binomial distribution:

$$p_N^n\left(X_{\max} \geq X_{\max}^{\text{obs}} \middle| E, 4\right) = \binom{N}{n} \left(p_1\left(X_{\max} \geq X_{\max}^{\text{obs}} \middle| E, 4\right)\right)^n \times \left(1 - p_1\left(X_{\max} \geq X_{\max}^{\text{obs}} \middle| E, 4\right)\right)^{N-n} \quad (3.8)$$

For the exclusion of primaries heavier than protons the probability that none ($n = 0$) of the N primaries induces a shower with $X_{\max} \geq X_{\max}^{\text{obs}}$ is of interest. This simplifies equation (3.8) to:

$$p_N^0\left(X_{\max} \geq X_{\max}^{\text{obs}} \middle| E, 4\right) = \left(1 - p_1\left(X_{\max} \geq X_{\max}^{\text{obs}} \middle| E, 4\right)\right)^N. \quad (3.9)$$

So the probability for a helium sample of a size N to induce at the least one shower with $X_{\max} \geq X_{\max}^{\text{obs}}$ is

$$p_N^{\geq 1}\left(X_{\max} \geq X_{\max}^{\text{obs}} \middle| E, 4\right) = 1 - \left(1 - p_1\left(X_{\max} \geq X_{\max}^{\text{obs}} \middle| E, 4\right)\right)^N. \quad (3.10)$$

The general behavior of $p_N^{\geq 1}$ as a function of p_1, without any assumptions on the underlying distributions for p_1, is shown in figure 3.4. For $p_1 \ll 1$ with Taylor expansion one gets from equation (3.10)

$$p_N^{\geq 1} \approx N p_1. \quad (3.11)$$

Using the relation between p_1 and the depth of the shower maximum, as given by the Gumbel distributions (see e.g. equation 3.6), one gets specific dependencies for $p_N^{\geq 1}$ on $X_{\max}^{\text{obs}}$ for different primary particles and interaction models. It shall be denoted for brevity the probability for a single helium shower to have $X_{\max} \geq X_{\max}^{\text{obs}}$ as

$$p_1^{\text{He}} \equiv p_1\left(X_{\max} \geq X_{\max}^{\text{obs}} \middle| E, 4\right) \quad (3.12)$$

and the probability for the set of N helium showers to produce at the least one event with $X_{\max} \geq X_{\max}^{\text{obs}}$ as

$$p_N^{\text{He}} \equiv p_N^{\geq 1}\left(X_{\max} \geq X_{\max}^{\text{obs}} \middle| E, 4\right). \quad (3.13)$$

The examples for p_N^{He} for different sample sizes N for EPOS LHC are given in figure 3.5. For $p_N^{\text{He}} \ll 1$, combining $p_N^{\text{He}} \approx N p_1^{\text{He}}$ with equation (3.7), one gets the approximation: $p_N^{\text{He}} \sim N \exp(-X_{\max}^{\text{obs}}/\Lambda_{\text{He}})$. Now for a given $X_{\max}^{\text{obs}}$ and a helium sample of size N with the energy E, one can estimate in this ideal case the probability to observe at the least one shower with $X_{\max} \geq X_{\max}^{\text{obs}}$.

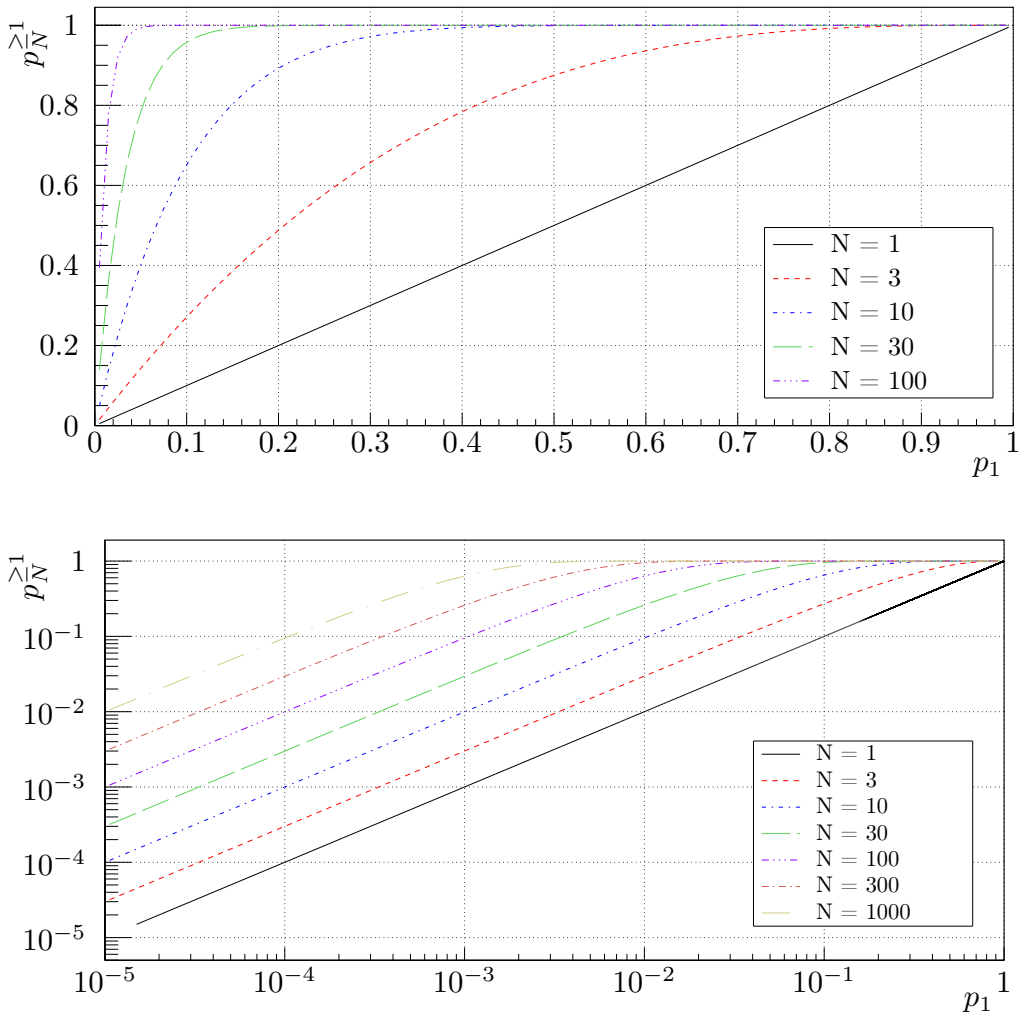

Figure 3.4.: The general behavior of $p_N^{\geq 1}$ as a function of p_1 as given by equation (3.10) without any assumptions on the underlying p_1 distributions on the linear (top) and log (bottom) scales.

3.4.3. Simulation study

To test the approach the following toy Monte-Carlo study was performed: Using Gumbel distributions for EPOS-LHC p–He samples with different sizes $N = 1, 3, 10, 30, 100, \ldots, 3000, 10000$ and different proton fractions $f_p = 1.0, 0.9, 0.8, \ldots, 0.0$ were prepared. For each N and f_p sets $\{\mathcal{S}(f_p, N)\}$ of

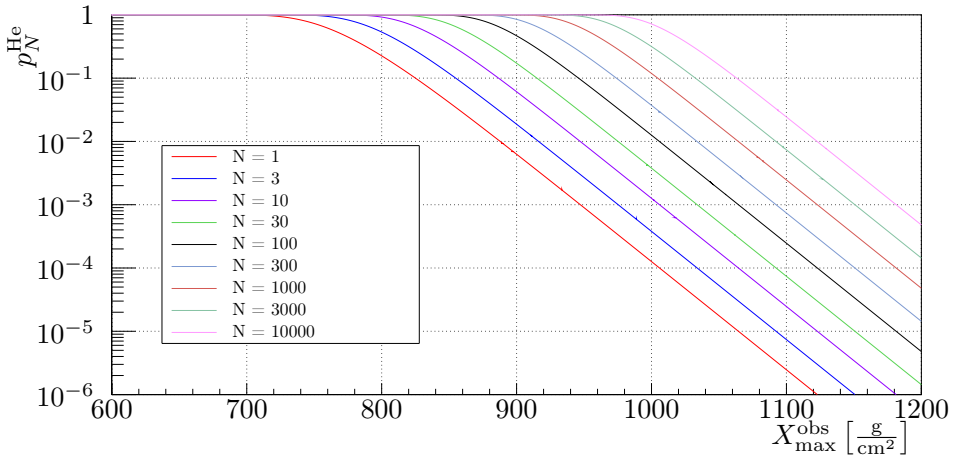

Figure 3.5.: The probabilities p_N^{He} for the sets of N helium showers to produce at the least one event with $X_{\mathrm{max}} \geq X_{\mathrm{max}}^{\mathrm{obs}}$. EPOS-LHC, $E = 10^{19}\,\mathrm{eV}$.

10000 samples were simulated at the fixed energy of $10^{19}\,\mathrm{eV}$[5]. From each sample $\mathcal{S}(f_p, N)$ one deepest event was picked out and p_N^{He} corresponding to X_{max} of this event was calculated.

The example distribution for the probabilities p_{100}^{He} (i.e. for the samples of the size $N = 100$) are given in figure 3.6.2. For the pure proton samples most of p_{100}^{He} values ($> 60\%$) are below 0.02, but still for many samples relatively large $p_{100}^{\mathrm{He}} > 0.05$ probabilities can be found. Thus even for a pure proton set of relatively small size $N \sim 100$ it might happen that the deepest event will not be deep enough to confirm reliably the presence of the primary protons. With the decreasing fraction of protons in the sample more and more of the deepest events may even be produced by helium and correspondingly large p_{100}^{He} values can be found more frequently. For pure helium samples the distribution of p_{100}^{He} becomes uniform as expected, since the same distribution p_1^{He} was used to both produce and interpret the data.

To have an idea on the chances to confirm the presence of the protons in the primary radiation, the dependence of the median of the p_N^{He} distribu-

[5] for $N = 1$ and 3, for cases when $f_p \times N$ is not an integer number, it was guaranteed that the composition averaged over all 10000 samples $\{\mathcal{S}(f_p, N)\}$ will contain the correct proton fraction f_p

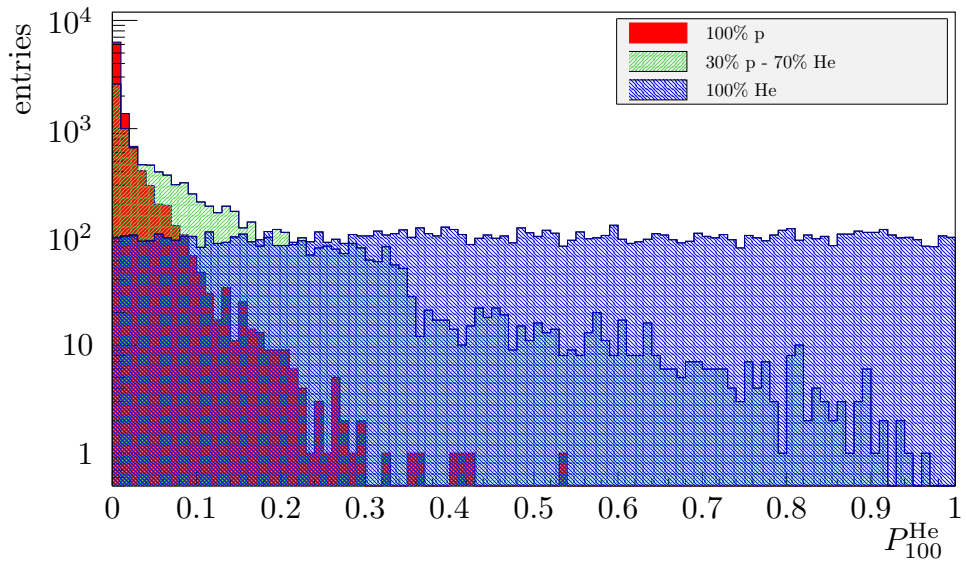

Figure 3.6.: p_{100}^{He} distributions for Monte-Carlo samples $\{\mathcal{S}(f_p, 100)\}$ containing 100 events with proton fractions $f_p = 1.0, 0.3$ and 0.0, EPOS LHC, 10^{19} eV.

tions on the fraction of protons f_p and on the sample size N was studied. From results presented in figure 3.7 one can see, for example, that for pure proton samples $f_p = 1.00$ the median value of 0.01 is reached for the sample size of around 50 events, but to reach the same median value for $f_p = 0.30$ one needs already a sample of around 500 events. This makes one realizes that it might be a challenging task to confirm the presence of protons in real data for high energies where statistics is relatively low (and possibly the proton fraction is low as well). Nevertheless one can count on a chance of having a single "gold plated" deep proton event which might be enough for drawing the conclusion that protons are likely to exist in the primary beam. From figure 3.8 one can see that even for single proton samples $f_p = 1.0$, $N = 1$ for few hundreds of samples (out of 10000) p_N^{He} is below 0.01, for larger samples the probability to have a "gold plated" event is growing rather quickly.

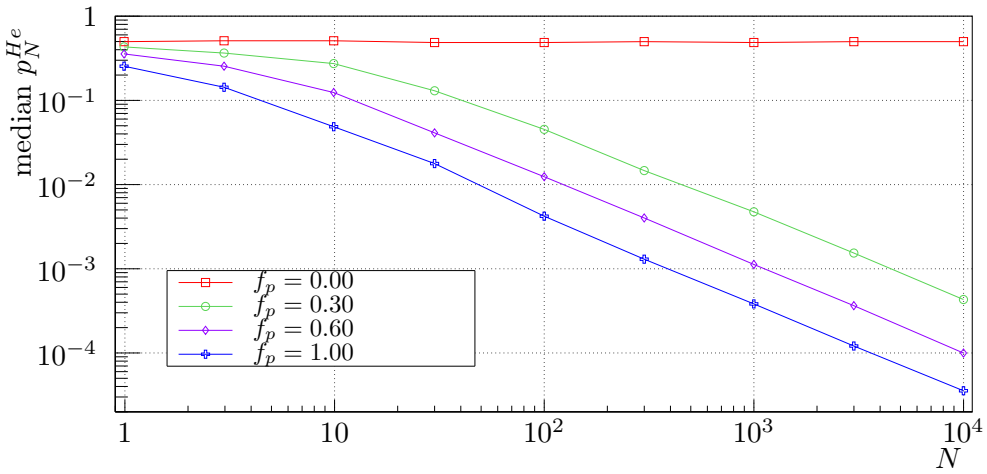

Figure 3.7.: The dependence of the median of the p_N^{He} distributions on the fraction of protons f_p and on the sample size N. See text for more details. EPOS-LHC, 10^{19} eV.

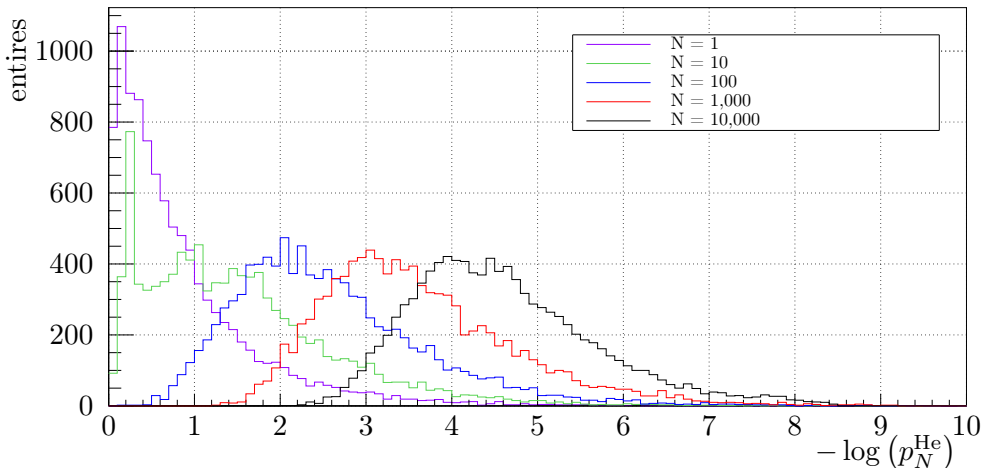

Figure 3.8.: p_N^{He} distributions for pure proton samples $f_p = 1.00$ of different sizes N. EPOS-LHC, 10^{19} eV.

3.5. Candidate selection

For real event factors like detector acceptance, resolution and uncertainties of the measurement and reconstruction should be taken these measures into account, due to their influence on the probability.

In this section we include into the calculation of the probability systematic and statistical errors on $X_{\mathrm{max}}$and FD energy of an event, the detector acceptance and penalization for number of events and the number of the energy bins. After selecting candidates with the smallest probabilities the final helium probability for them should be determined via dedicated real MC simulations. The outcome of the method is the highest energy bin where the presence of primary protons can be stated at a given confidence level.

3.5.1. Uncertainties on $(X_{\mathrm{max}}^{obs}, E^{obs})$, detector acceptance

The systematic uncertainties are treated conservatively maximizing the helium probability: the systematic uncertainty $\Delta X_{\mathrm{max}}^{\mathrm{syst}}$ is substracted from the measured $X_{\mathrm{max}}^{\mathrm{obs}}$

$$X'_{\mathrm{max}} = X_{\mathrm{max}}^{\mathrm{obs}} - \Delta X_{\mathrm{max}}^{\mathrm{syst}}, \tag{3.14}$$

correspondingly the uncertainty on energy ΔE^{syst} is added to E^{obs}

$$E' = E^{\mathrm{obs}} + \Delta E^{\mathrm{syst}}, \tag{3.15}$$

and the helium probability is calculated using the Gumbel distribution $\mathcal{G}(X_{\mathrm{max}}|E', 4)$ for E'. For the systematic errors $\Delta X_{\mathrm{max}}^{\mathrm{syst}}$ and ΔE^{syst} in this work constant values of $10\,\frac{\mathrm{g}}{\mathrm{cm}^2}$ [Aab14] and 15 % [Ver13] are used in the case of the data of the Pierre Auger Observatory.

To take the detector acceptance into account the distribution is modified using the parameterization for a relative acceptance $\mathcal{A}(X_{\mathrm{max}}|E')$

$$\mathcal{G}^*_{\mathcal{A}} = \mathcal{G}(X_{\mathrm{max}}|E', 4) \cdot \mathcal{A}(X_{\mathrm{max}}|E') \tag{3.16}$$

and is re-normalized

$$\mathcal{G}_{\mathcal{A}} = \frac{\mathcal{G}^*_{\mathcal{A}}}{\int_0^\infty \mathcal{G}^*_{\mathcal{A}}\,\mathrm{d}X_{\mathrm{max}}}. \tag{3.17}$$

Further, for the evaluation of the $p^{\mathrm{He}}_{1,\Delta}$ probability, random shower maxima $X^{\mathrm{rnd}}_{\mathrm{max}}$ are generated using the acceptance modified Gumbel distribution $\mathcal{G}_{\mathcal{A}}$. The impact of the acceptance correction on $p^{\mathrm{He}}_{1,\Delta}$ is shown in figure 3.9 for the example of the standard FD cuts of the Pierre Auger Observatory, as described in [Aab14].

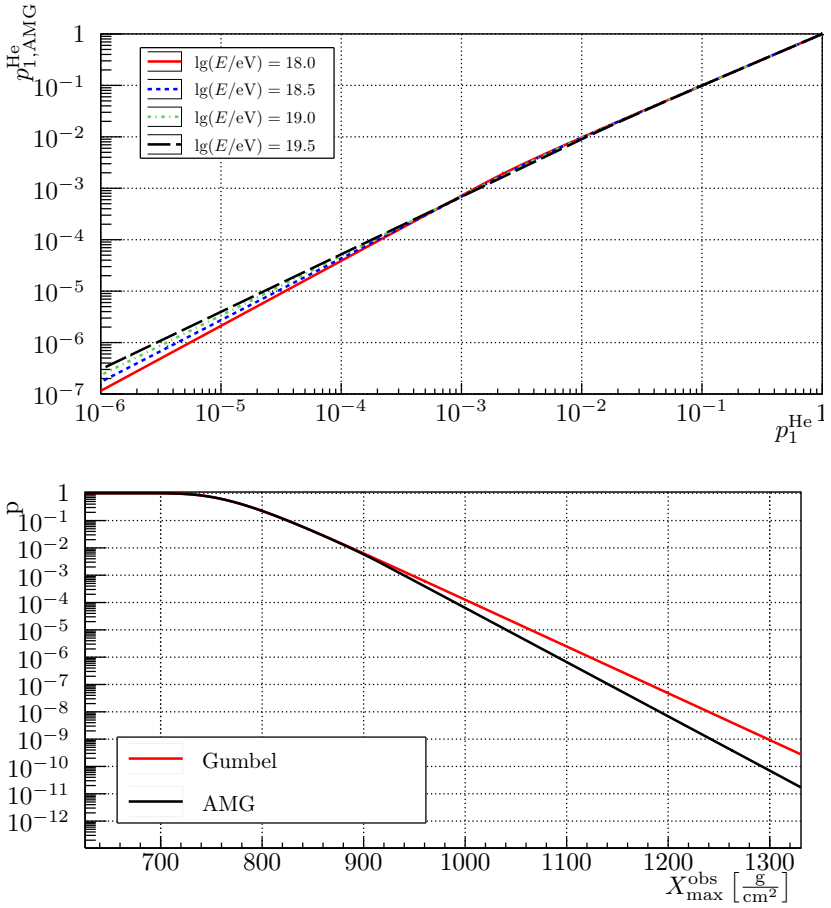

Figure 3.9.: Comparison of the probabilities for helium nuclei to produce a shower with $X_{\mathrm{max}} > X^{\mathrm{obs}}_{\mathrm{max}}$: p^{He}_1 — using the Gumbel distribution, $p^{\mathrm{He}}_{1,\mathrm{AMG}}$ — using the acceptance-modified Gumbel (AMG) distribution.

The statistical uncertainty on energy ΔE^{stat} is transformed to an X_{max} uncertainty $\Delta X^{\mathrm{E,stat}}_{\mathrm{max}}$ using an elongation rate of 60 g/cm^2 per decade. The impact of the energy's uncertainty is small compared to the uncertainty of the measurement of the shower maxmimum's depth: An uncertainty of

15 % in energy gives a transformed uncertainty of about 3.5 g/cm^2, which is well below the typical $\Delta X_{\max}^{\text{stat}}$ of about 12 g/cm^2.

3.5.2. Determination of $p_{1,\Delta}^{\text{He}}$

In order to include the uncertainties of the shower's measurement the value of $p_{1,\Delta}^{\text{He}}$ is determined. In contradiction to the simple p_1^{He} value, $p_{1,\Delta}^{\text{He}}$ should give not only a measure of the showers depth but also how certain the measure of this depth was: Measured shower events with large uncertainties shall be penalized with higher probabilities, since lower $X_{\max}$ values with higher probabilities were still likely. Nonetheless, these statistical uncertainties cannot be handled as conservative as the systematic ones, since the fluctuations can also cause a reconstruction with lower than the real depth of shower maximum. Nonetheless, the observed and reconstructed $X_{\max}$ is the most probable one and therefore should be favored. In order to weight these possibilities, following algorithm was established.

Utilizing the normalized acceptance modified Gumbel distribution of equation 3.17 a random shower maximum $X_{\max}^{\text{rnd}}$ is picked, using E' of the corresponding observed event:

$$X_{\max}^{\text{rnd}} \sim \mathcal{G}_{\mathcal{A}}(X_{\max}|E', 4) \tag{3.18}$$

For both, the transformed energy uncertainty $\Delta X_{\max}^{\text{E,stat}}$ and the statistical uncertainty $\Delta X_{\max}^{\text{stat}}$, two random values are picked from gaussian distributions $\Delta X \sim \mathcal{N}\left(0, (\Delta X_{\max}^{\text{stat}})^2\right)$, $\Delta X^E \sim \mathcal{N}\left(0, \left(\Delta X_{\max}^{\text{E,stat}}\right)^2\right)$ and are added to $X_{\max}^{\text{rnd}}$

$$X_{\max}^{\text{probe}} = X_{\max}^{\text{rnd}} + \Delta X + \Delta X^E. \tag{3.19}$$

The ratio of the number of trials N_{deep}, in which $X_{\max}^{\text{probe}} \geq X'_{\max}$, to the total number of trials N_{tot} gives $p_{1,\Delta}^{\text{He}}$

$$p_{1,\Delta}^{\text{He}} = \frac{N_{\text{deep}}}{N_{\text{tot}}} \tag{3.20}$$

The procedure is stopped when the error on $p_{1,\Delta}^{\text{He}}$ reaches the value of 0.05

$$\frac{\Delta p_{1,\Delta}^{\text{He}}}{p_{1,\Delta}^{\text{He}}} \simeq \frac{1}{\sqrt{N_{\text{deep}}}} \leq 0.05 \qquad \text{(i.e. } N_{\text{deep}} \gtrsim 400\text{)}. \tag{3.21}$$

bin	E_{min}	E_{max}	N_i based on ICRC2017[Bel17]
1	17.8	17.9	4586
2	17.9	18.0	4001
3	18.0	18.1	3338
4	18.1	18.2	3396
5	18.2	18.3	2704
6	18.3	18.4	2075
7	18.4	18.5	1596
8	18.5	18.6	1099
9	18.6	18.8	1405
10	18.8	19.0	824
11	19.0	19.4	711
12	19.4	∞	127

Table 3.2.: List of energy bins: $[E_{\mathrm{min}}, E_{\mathrm{max}}[$

In the next step all events are sorted into twelve energy bins, following table 3.2, and the event with the smallest probability $\mathrm{min}_i\left(p^{\mathrm{He}}_{1,\Delta}\right)$ in each bin i is taken as a candidate event.

3.6. Determination of the final probabilities P^i_{He}

In the previous section the determination of the preliminary candidate probability $\mathrm{min}_i\left(p^{\mathrm{He}}_{1,\Delta}\right)$ and candidate selection was presented. This selection method provides a quick and easy algorithm to determine the least probable events in a bin.

Since the detector acceptance is a function of the shower's geometry one needs to take the candidate's geometry into account. This can be done via dedicated simulations reproducing the individual shower geometry of each candidate and allowing to estimate a final single event probability $P^{\mathrm{He}}_{1,i}$.

3.6.1. Dedicated simulations

The determination of the final probabilities for all twelve candidates with $\mathrm{min}_i\left(p^{\mathrm{He}}_{1,\Delta}\right)$ is performed using dedicated CONEX and $\overline{\mathrm{Off}}\underline{\mathrm{line}}$ simulations.

These simulations use the reconstructed shower geometry to include directional effects, which were averaged in the acceptance function.

For this a large number of helium showers for the respective energy E' and the same geometry of the candidate event is produced. The number of simulated events with $X_{\mathrm{max}} \geq X'_{\mathrm{max}}$ is calculated as:

$$f_{\mathrm{He}} = \sum_{j} \int_{X'_{\mathrm{max}}}^{\infty} \mathcal{N}\left(X_{\mathrm{max}}^{\mathrm{recon,j}}, \left(\Delta X_{\mathrm{max}}^{\mathrm{E,stat,j}}\right)^2 + \left(\Delta X_{\mathrm{max}}^{\mathrm{stat,j}}\right)^2\right) \mathrm{d}X_{\mathrm{max}} \tag{3.22}$$

where j runs over all simulated events, the $X_{\mathrm{max}}^{\mathrm{recon,j}}$ are the reconstructed shower maxima and $\Delta X_{\mathrm{max}}^{\mathrm{E,stat,j}}$ and $\Delta X_{\mathrm{max}}^{\mathrm{stat,j}}$ are the statistical uncertainties. That is, each event contributes to f_{He} according to its probability to produce $X_{\mathrm{max}} \geq X'_{\mathrm{max}}$. The final (single-event) helium probability of the i-th candidate is determined as

$$P^{\mathrm{He}}_{1,i} = \frac{f_{\mathrm{He}}}{N_{\mathrm{totsim}}}, \tag{3.23}$$

where N_{totsim} is the sufficient large simulation statistics.

Afterwards, the penalization for the number of events in the respective bin is applied to determine $P^{He}_{N,i}$ as described in section 3.4.2.

3.6.2. Penalization for the number of bins

The search in N_{bins} should be treated as multiple trials and thus should be penalized. For the derivation of the penalty factor consider picking N_{bins} random numbers representing the smallest probabilities $P^{He}_{N,i}$ in each bin (see table 3.1). In the most conservative case of 100 % Helium composition the distribution of $P^{\mathrm{He}}_{N,i}$ is uniform (see figure). The probability that an uniformly distributed random number X_i is greater than some value $P_s \in (0,1)$ is given by

$$P(X_i > P_s) = 1 - P_s. \tag{3.24}$$

Since X_i are independent , the probability of all X_i being greater than P_s is

$$\begin{aligned} P\left(X_i > P_s,\ \forall i \in [1, N_{\mathrm{bins}}]\right) &= \prod_{i=1}^{N_{\mathrm{bins}}} P(X_i > P_s) && (3.25)\\ &= \prod_{i=1}^{N_{\mathrm{bins}}} 1 - P_s && (3.26)\\ &= (1 - P_s)^{N_{\mathrm{bins}}}. && (3.27) \end{aligned}$$

The probability of at least one random number being smaller or equal to P_s is given by

$$P(\exists i \in [1, N_{\text{bins}}] : X_i \leq P_s) = 1 - P(X_i > P_s,\ \forall i \in [1, N_{\text{bins}}]) \quad (3.28)$$
$$= 1 - (1 - P_s)^{N_{\text{bins}}}. \quad (3.29)$$

Setting P_s equal to $P^{\text{He}}_{N,i}$ one gets the final expression for the penalized probability

$$P^{\text{He}}_i = P\left(\exists i \in [1, N_{\text{bins}}] : X_i \leq P^{\text{He}}_{N,i}\right) = 1 - \left(1 - \left(P^{\text{He}}_{N,i}\right)\right)^{N_{\text{bins}}}. \quad (3.30)$$

P^{He}_i is the final probability of the candidate event in bin i.

3.6.3. Impact of interaction model

Due to differences in X_{max}between various interaction models the search might, in principle, result in model-dependent sets of the selected proton candidates. However, the chance for this to happen is very small: the usage of QGSJet II-04 or EPOS-LHC gives the same candidates for all 400 sets analyzed in section 4.

Nonetheless, as conservative choice of the final probability, the largest value of P^{He}_i predicted by an interaction model is chosen.

The confidence level for excluding helium or heavier masses for each candidate is given by $CL_i = 1 - P^{\text{He}}_i$.

4 Performance of method

After the development of the method it is tested that it has the expected performance. With an artificially created set of mock data it is possible to test the Helium hypothesis against itself in a quick way with high statistics.

4.1. Mock samples

To test the performance of the method, we implemented a quick way to produce a big amount of mock samples with different mass compositions from the parametrizations of X_{max}distributions with the Gumbel function [Dom]. The mock showers are produced from energy spectrum E^{-3} and their X_{max} values are picked from the Gumbel distribution for the corresponding primary nuclei. Further, events are removed from the samples in accordance with the behavior of the FD acceptance. The generated energy and X_{max} values are smeared using the distributions of statistical uncertainties on energy and $X_{\mathrm{max}}$from data [Aab14]. Finally, using the same distributions of uncertainties we assign measurement errors to $X_{\mathrm{max}}$and energy of each event. This way the mock samples contain the same information as data and one can apply to them the search algorithm described in chapter 3.

The performance of the method is tested on four different mass compositions:

100 % p	100 % He	50 % p + 50 % He	35 % p + 35 % He + 30 % N

For each composition 100 sets consisting of 26,000 events each are produced using Gumbel X_{max}parametrization for EPOS-LHC.

4.2. Benchmarks

To evaluate the performance of the proton search the following benchmarks are checked at a given confidence level:

1. Number of sets with at least one candidate at a certain confidence level;

2. Number of candidates per set (possible values lie between 0 and 12);

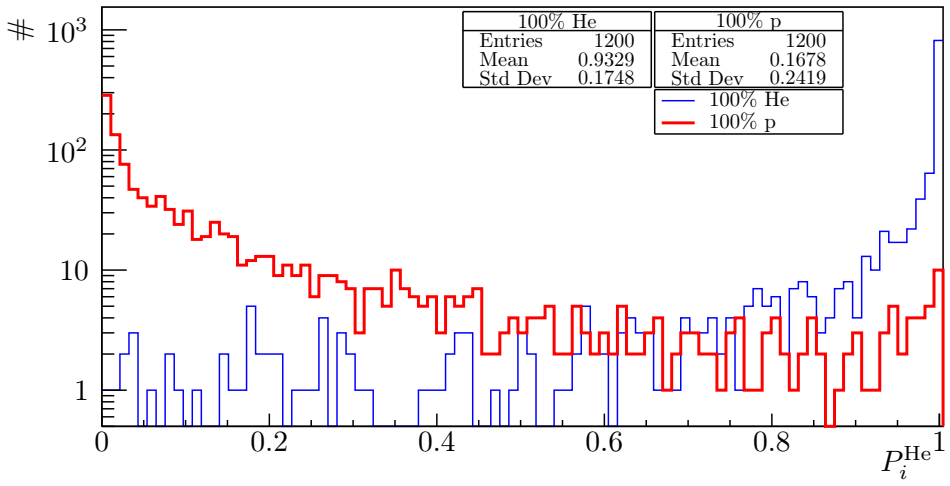

Figure 4.1.: Distribution of all P_i^{He} for the pure compositions. Bins without a candidate due to the pre-selection cut where handeled as $P_i^{He} = 1$.

3. Maximum energy of a candidate at a certain confidence level;

4. Fraction of protons among candidates (for mixed compositions only).

For the pure helium composition the result for the first benchmark is shown in figure 4.2.

The number of sets with at least one proton candidate is within the expectations with only a single point outside the 1σ band.

For compositions including protons the number of sets with at least one proton candidate is significantly larger than for the pure helium case (figure 4.3). For all three compositions up to 99 % confidence level the candidates are found in the majority (> 60 %) of the sets. Only at the highest tested confidence level of 99.9 % this number drops to about 25 to 40 sets out of 100 for the mixed compositions.

The total number of candidate events per set (the second benchmark), shown in figures 4.4 and 4.5, grows as expected with the increase of the proton fraction. For all compositions containing protons there is a chance to find candidates up to the confidence level of 99.9 % though in this case the mean number of candidates per set is smaller than one.

Since at a given confidence level the number of candidates and their maximum energy are correlated, the mean energy of the most energetic candidates decreases with an increase of the confidence level (figure 4.7). For instance at a confidence level of 95 % for compositions containing

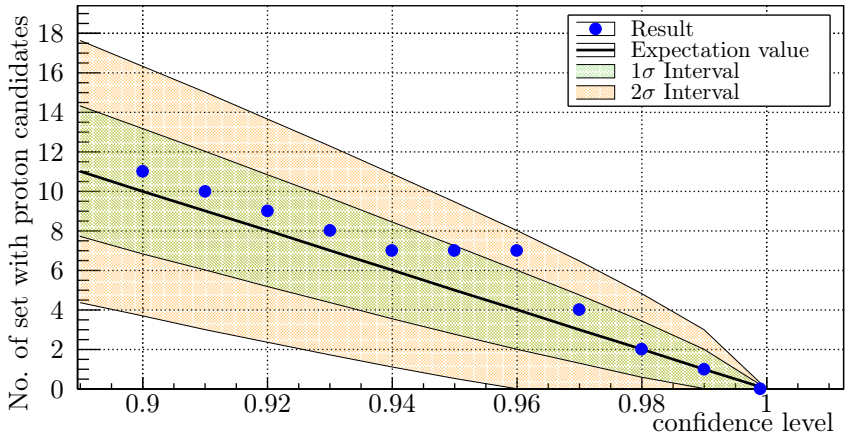

Figure 4.2.: Pure helium samples: number of sets out of 100 with at least one proton candidate as a function of the confidence level compared to the poissonian expectation.

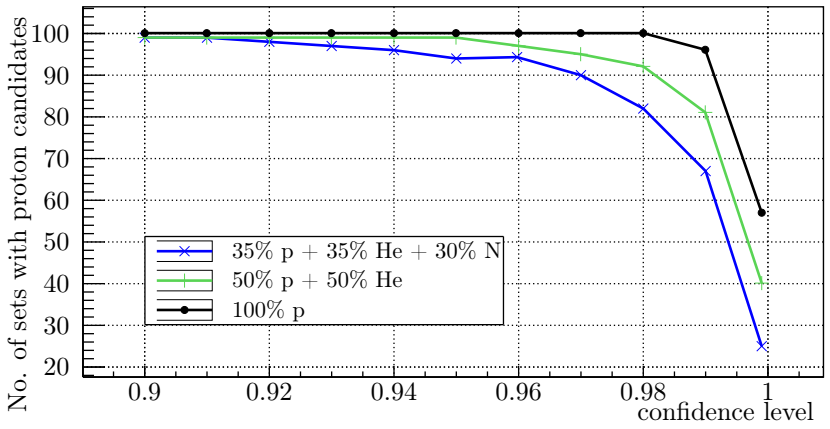

Figure 4.3.: Compositions including protons: number of sets out of a total of 100 with at least one proton candidate as a function of the confidence level.

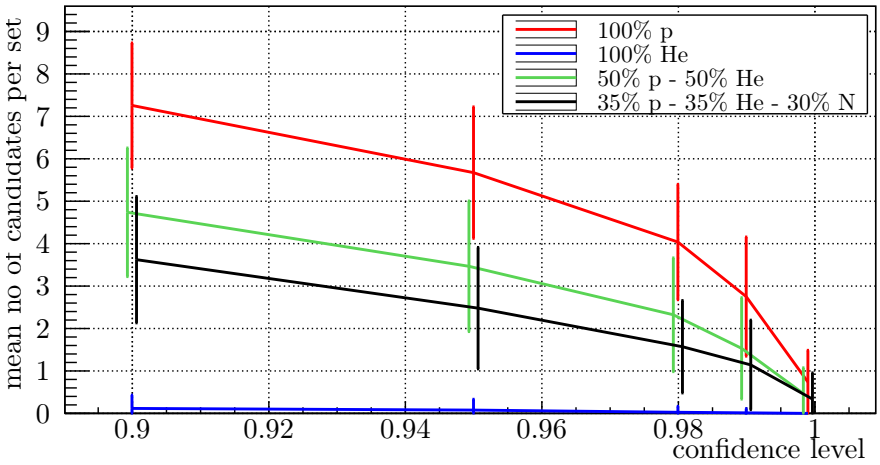

Figure 4.4.: Mean number of candidates per data set. The error bars show the standard deviation of the mean. The data points are shifted along x-axis to improve visibility.

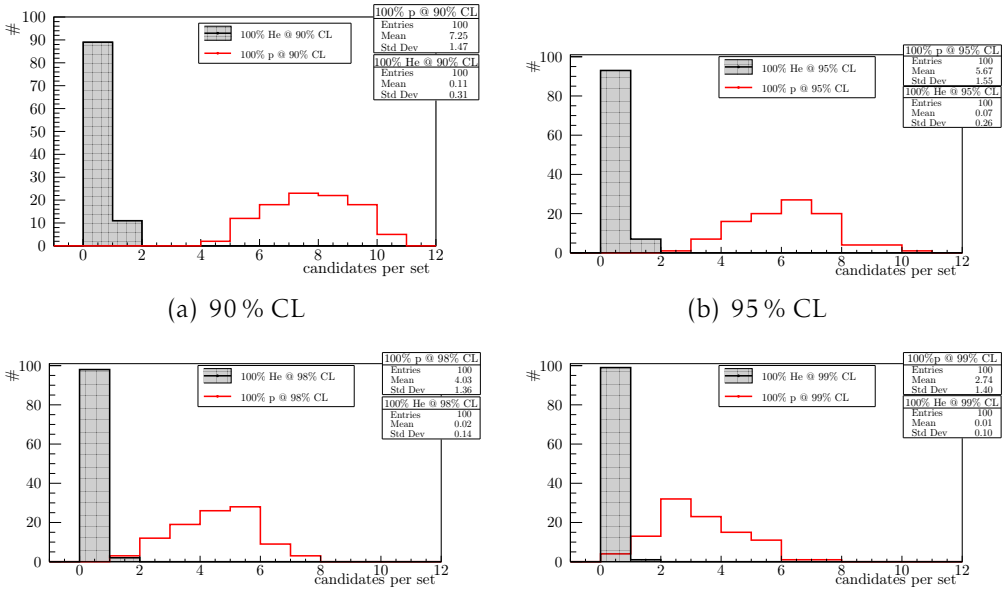

(a) 90 % CL (b) 95 % CL

(c) 98 % CL (d) 99 % CL

Figure 4.5.: Distributions of number of proton candidates per set at different confidence levels.

protons the mean maximum energy is $\lg(E/\mathrm{eV}) \approx 18.4 - 18.9$. At the same time in a few samples the highest maximal energy still can be above

$\lg(E/eV) \approx 19.5$ (figure 4.6).

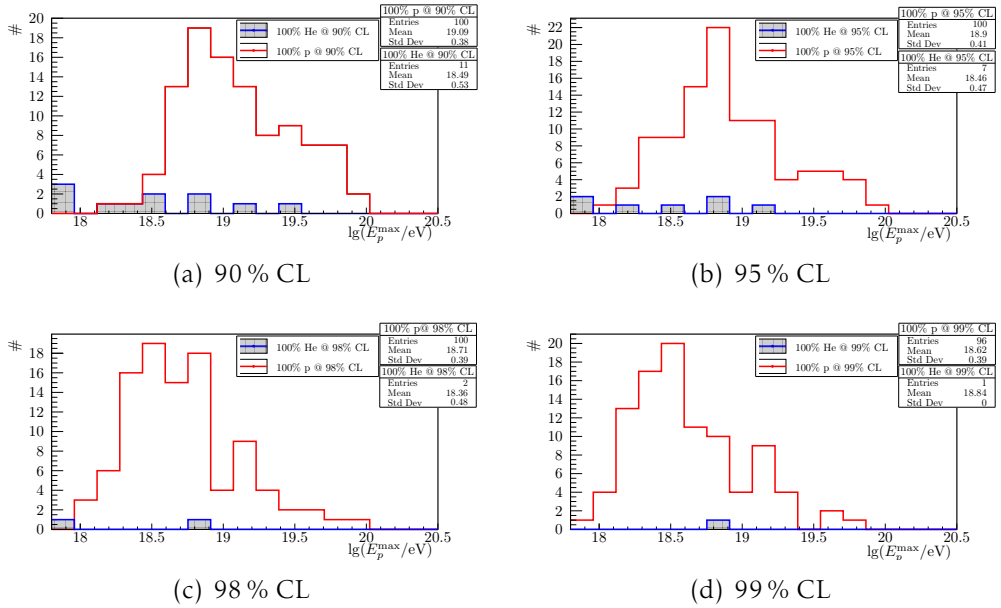

(a) 90 % CL (b) 95 % CL

(c) 98 % CL (d) 99 % CL

Figure 4.6.: Distribution of maximum energy of proton candidates per set at different confidence levels.

The fraction of correctly identified protons (the fourth benchmark) for both mixed compositions is given in figures 4.8 and 4.9. As expected this fraction increases for higher confidence levels. A misidentification happens only at confidence levels below 95% (figure 4.8), but even there about 98 % of the candidates are MC protons.

In the 35 %p + 35 %He + 30 %N case a single outlier in the fourth lowest bin causes a misidentification up to the CL of 98% (figure 4.9).

4.3. Summary

The tests of the method have shown that it performs in accordance with the expectations. The estimated highest energy up to which the protons can be most probably found in a proton-containing mock sets of 26000 events, lies in the range $\lg(E/eV) \approx 18.4 - 18.9$.

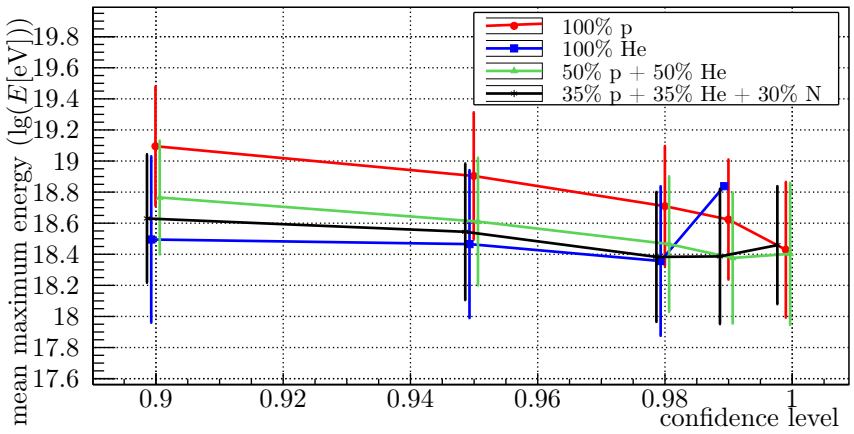

Figure 4.7.: Average energy of the most energetic candidate. The error bars show the standard deviation of the mean. The data points are shifted along x-axis to improve visibility.

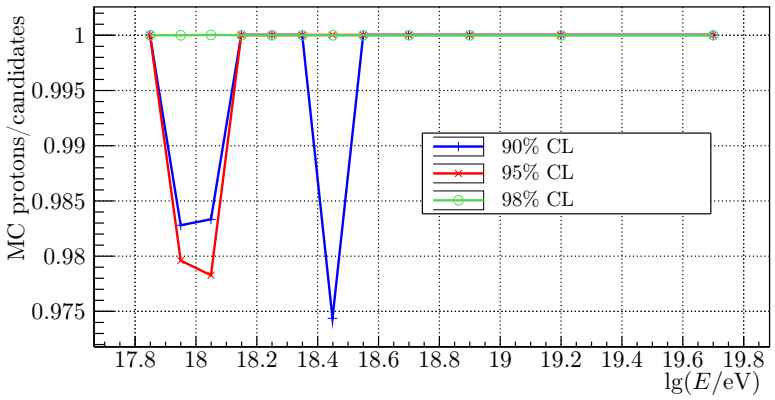

Figure 4.8.: Fraction of candidates, which are MC protons, in the 50 %p + 50 %He case.

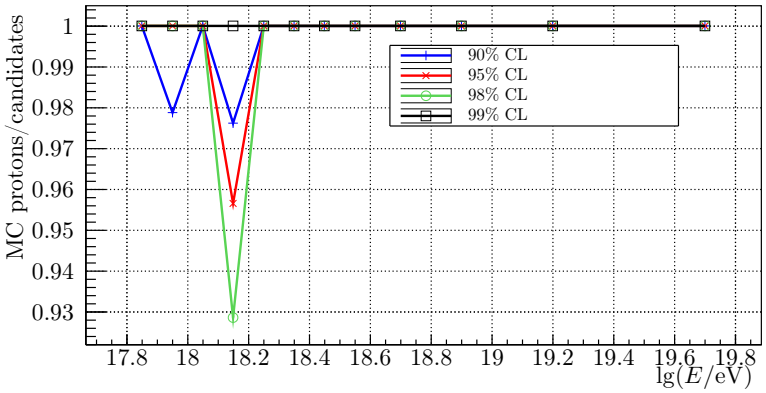

Figure 4.9.: Fraction of candidates, which are MC protons, in the 35 %p + 35 %He + 30 %N case.

5 Data selection

The developed analysis is applied to the data of the Pierre Auger Observatory. In this chapter, the process of the selection of the raw events is described. These cuts ensure a sufficiently high quality of the recorded data. This analysis is applied to the hybrid data of the Pierre Auger Observatory as presented in [Bel17].

5.1. Description of the selection criteria

The first set of cuts applied to the raw data rejects data taken with unstable conditions. The **Bad FD periods** cut rejects acquired data taken during time periods, where the FD telescopes were not in operation or had non-optimal conditions. This happens if no calibration is available, occurring glitches of the GPS or the PMT baseline is unstable. Other cuts related to the PMT of the FD are the **bad pixels** cut, which takes malfunctioning pixels in the air shower's trace into account, or the **Skip saturated PMT** cut, which is activated when the PMT's signal is saturated [Por14].

Closely related to the PMT are the cuts of the **Shutter status**: While the shutters of the FD telescopes were closing the acquisition of data is still possible. Due to the smaller aperture, the mean signal and its RMS during this phase is smaller compared to the periods when the shutter is fully opened. Therefore a certain threshold for the RMS of the recorded data is required for the acquired data to be accepted [Por14].

The last cut directly connected to the data acquisition is called **Good 10 MHz Correction** cut. This cut ensures that only data with a GPS timing precision at nanosecond level is accepted.

The next section of cuts is related to the properties of hybrid measurement of the events, which is necessary to perform this analysis based on X_{max}. The **Has hybrid geometry** cut rejects events without any reconstructed SD tanks, which are obviously no hybrid events, while events with at least one triggered tank are called "brass hybrid events".

Very inclined showers are rejected by the **Maximum zenith angle** cut as well as events with a reconstructed FD energy lower than $10^{17.8}$ eV. Events, whose SD reconstruction uses a very distant (more than 1.5 km distance from the core) tank as a reference, are rejected by the cut of the **Maximum distance Core-Tank** [Por14].

As mentioned in chapter 2.2.4 the atmospheric conditions at the time

of the shower's detection are monitored. This is ensured by using the **Measured Mie model available** cut, which checks if the aerosol content in the atmosphere had been measured and modeled. The **Maximum VAOD**[1] cut restricts events while the atmosphere was too dense, caused by aerosols, since this increases the systematic uncertainty on the event's energy. An additional **cloud cut** only accepts events with an admissible small cloud coverage [Por14].

The cuts on the reconstruction ensures a sufficiently good reconstruction by rejecting events with only a short track in the FD (**Minimum track length** cut), with larger gaps in the recorded tracks (**Maximum gap in the slant depth** cut).

The probability of an air shower to be detected as brass hybrid event depends on the shower geometry, the primary's mass and its position on the array. This probability can be determined for every detected shower and possible primary type. To be accepted the calculated probability for inducing a brass hybrid event must be greater than 90 % for proton and iron primaries (**Minimum P brass** cut). The difference of the probabilities between both primaries should not exceed 5 % (**Maximum P brass proton iron difference** cut). The **profile** χ^2 cut is designed to reject events with a badly reconstructed profile [Por14].

The last cuts to describe are cuts on the depth of the shower's maximum. The first condition requires the depth of the reconstructed shower maximum to be in the geometrical field of view (FOV) of the respective telescope (X_{max}**in FOV** cut). This reduces the uncertainty on the reconstructed depth. The X_{max}**in expected FOV** cut takes the viewing angle to the shower into account. This cut decreases the geometrical FOV to an area, in which the uncertainties due to the viewing angle are acceptably small. The reconstructed X_{max}needs to be in this expected field of view. The resulting data set is biased to the composition of cosmic rays, since a limited field of view has different responses to light particles, penetrating deeper with a larger spread, and heavier particles, penetrating shallower with a relatively small spread. In order to remove that bias, the X_{max}**in fiducial field of view** cut is designed. In the application of this cut, a fiducial volume is determined, in which the observation of air showers is not biased. This is done by comparing the reconstructed X_{max}values of virtual showers with same geometry and energy as the observed one with and without a limited field of view. The area where the difference between unlimited and limited field of view is bigger than $5\,\frac{\mathrm{g}}{\mathrm{cm}^2}$ is the re-

[1] **V**ertical **A**erosol **O**ptical **D**epth

jection area. The case of equality one can determine the upper and lower limit of the rejection area. For the fiducial FOV cut, the lower end of the expected field of view needs to be lower than the lower end of the fiducial rejection area, and – analogous – the upper end of the expected field of view needs to be larger than the upper limit of the fiducial rejection area [Por14].

These cuts are applied to the taken data, which result in a dataset, which is referred to as the ICRC 2017 data set in the following. This set includes the data taken in the period from December 1, 2004 to December 31, 2015 [Bel17].

5.2. The ICRC 2017 data set

The resulting set of data after the application of the described cuts contains 26,150 hybrid events. Their reconstructed energy and shower maximum is shown as a scatterplot in figure 5.1, where each event is represented by a cross. Two of these events are obviously possible candidates events, since they are quite deep compared to the rest of the events with comparable energy. The first of these events is the only one deeper than $1100\,\frac{\mathrm{g}}{\mathrm{cm}^2}$ at $\lg E[\mathrm{eV}] \approx 18.2$. The other one has a depth of shower maximum of about $1060\,\frac{\mathrm{g}}{\mathrm{cm}^2}$ and $\lg E[\mathrm{eV}] \approx 18.9$. It is expected that these two events appear as candidates in their respective bins.

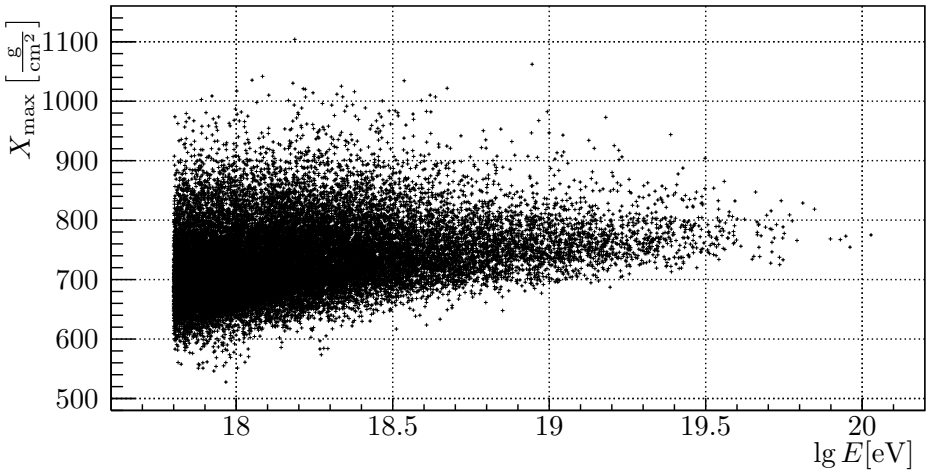

Figure 5.1.: A scatterplot of the ICRC data set [Bel17].

6 First application to data

The analysis presented in chapter 3 is applied to the data described in chapter 5. In this chapter the selected candidate events are presented and the corresponding probabilites are determined with at least 100,000 dedicated simulations for each event.

6.1. The selection of the candidate events

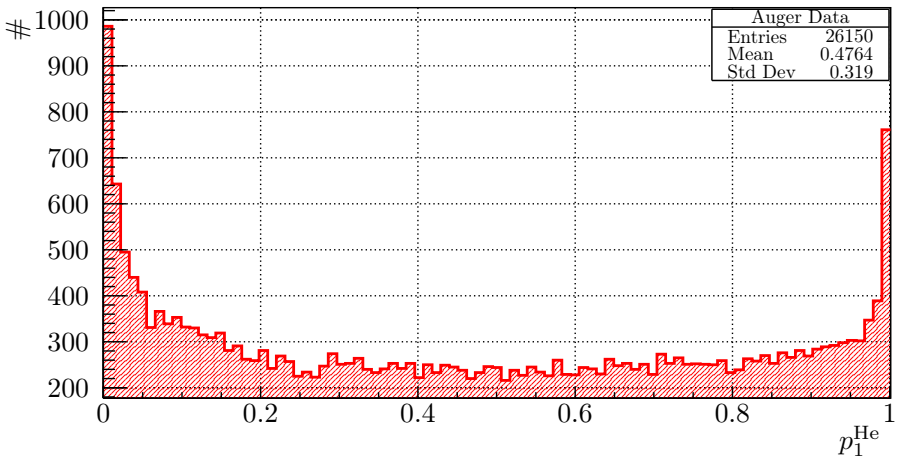

Figure 6.1.: The distribution of p_1^{He} in the data set.

Figure 6.1 shows the distribution of the preliminary probability p_1^{He} using QGSJet II-04. The pre-selection criterium of $p_1^{He} \leq 0.1$ is fulfilled by 4381 events, for which $p_{1,\Delta}^{He}$ is determined. The result of this determination is shown in figure 6.2. The fact that about 17 % of the total events passed the pre selection criterium of $p_1^{He} \leq 10\,\%$ may be seen as a slight hint that there may be lighter components than Helium nuclei in the primary composistion. A pure Helium composition is expected to produce a uniform p_1^{He} distribution with 10 % of the total events passing the pre-selection criterium. Likewise, the peak for $p_1^{He} \rightarrow 1$ indicates the presence of elements heavier than Helium.

A similar behavior is seen if EPOS-LHC is used, which is shown in appendix C.

The selection of the candidate events, based on $p_{1,\Delta}^{He}$, is shown in table 6.1, with the probabilities in table 6.2. Since there are no extremely

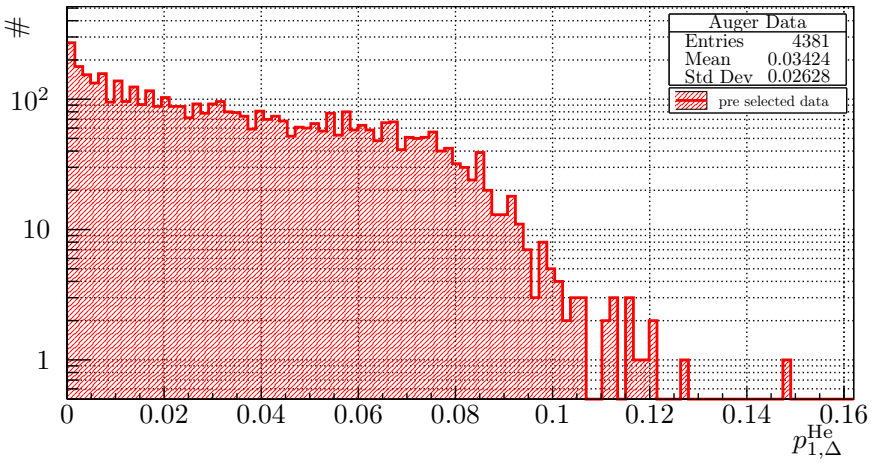

Figure 6.2.: The distribution of $p^{He}_{1,\Delta}$ of all events passing the pre-selection criterium.

bin	SD ID	$X_{max}\left[\frac{g}{cm^2}\right]$	$\Delta X_{max}\left[\frac{g}{cm^2}\right]$	$\lg E[eV]$	$\lg(\Delta E[eV])$
1	24824224	1002.8	34.3	17.889	16.807
2	11291575	1008.7	28.3	17.923	16.743
3	13916102	1041.8	16.1	18.084	16.851
4	9341447	1103.9	26.1	18.187	17.059
5	5158565	1020.0	24.1	18.221	16.960
6	11190385	1011.7	19.4	18.322	17.077
7	8211456	1000.5	20.8	18.467	17.197
8	10373860	1034.4	31.5	18.537	17.387
9	24348800	1021.7	15.6	18.674	17.586
10	3428370	1062.1	27.7	18.945	17.938
11	10079827	972.8	13.8	19.181	18.037
12	7624453	904.1	8.4	19.498	18.276

Table 6.1.: Overview of the candidate events in the dataset [Bel17]. For more details see appendix D. The total number of events in each bin is shown in table 3.2

deep events present in the data set, extremely low probabilities were not expected. Still, the probabilities reache down to the 10^{-6} level for the least probable event. This least probable event (bin 4) was already expected to be a possible candidate in chapter 5. The second mentioned event can also be found as candidate in bin 10. For these candidates the selection is very clear, since they have no other event within 75 $\frac{\mathrm{g}}{\mathrm{cm}^2}$ in the respective bin. The profiles of these two events are sufficiently well reconstructed, as shown in figure 6.3. Plots of all candidates can be found in appendix D. All candidates are of reasonable quality, only for the low-energy candidates the quality is sonmewhat degraded, which is, however, not unexpected.

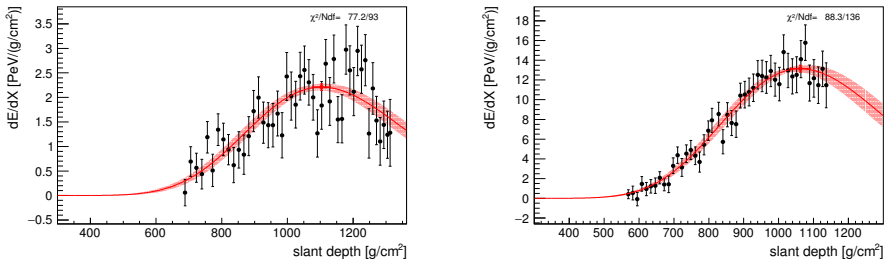

(a) Fourth bin.

(b) Tenth bin.

Figure 6.3.: Profiles of the two deepest candidates.

In bin 5, the deepest event was not chosen as a candidate, as shown in figure 6.4. This might happen, if the depths of the shower maxima are very close to each other and the difference in the uncertainty is big enough, which is the case in this bin.

6.2. Determination of the dedicated probabilities $P_{1,i}^{\mathrm{He}}$

For each of the selected candidate events 100,000 dedicated CONEX and Offline simulations[1] are performed and are used to determine $P_{1,i}^{\mathrm{He}}$ as described in chapter 3.6.1. The only exception to this is the candidate of bin four, for which 1,000,000 simulations were done, due to the small probability. The shower core's position and the direction were sampled

[1] All simulations used in this section were kindly performed by Alexey Yushkov, Fyzikální ústav AV ČR, Prague, Czech Republic.

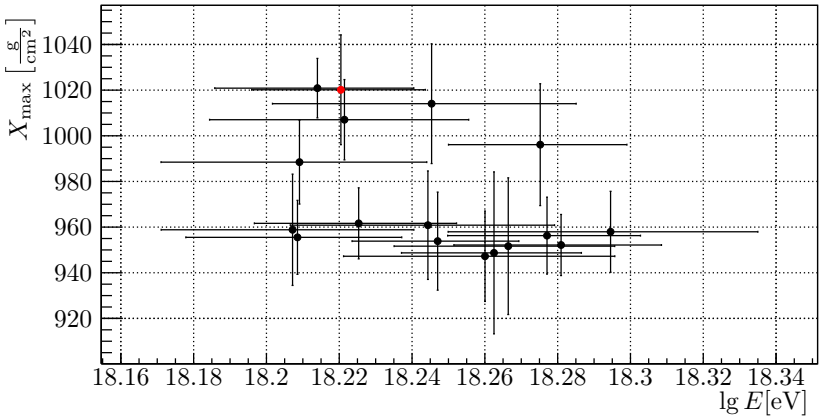

Figure 6.4.: All events of the ICRC 2017 dataset [Bel17] within a 75 $\frac{g}{cm^2}$ distance to the candidate in the fifth bin. The selected candidate event is marked in red.

from gaussian distributions with means and widths corresponding to the measured values and their uncertainties. The resulting f_{He} value and the corresponding values of $P^{\mathrm{He}}_{1,i}$ are listed in table 6.2.

bin	f_{He}	$p^{\mathrm{He}}_{1,\Delta}$	$P^{\mathrm{He}}_{1,i}$	$P^{\mathrm{He}}_{N,i}$	P^{He}_{i}
1	4.88	$4.19 \cdot 10^{-5}$	$4.88 \cdot 10^{-5}$	$2.01 \cdot 10^{-1}$	$9.32 \cdot 10^{-1}$
2	2.91	$2.52 \cdot 10^{-5}$	$2.91 \cdot 10^{-5}$	$1.10 \cdot 10^{-1}$	$7.53 \cdot 10^{-1}$
3	0.8473	$1.21 \cdot 10^{-5}$	$8.36 \cdot 10^{-6}$	$2.74 \cdot 10^{-2}$	$2.84 \cdot 10^{-1}$
4	1.13	$2.03 \cdot 10^{-6}$	$1.13 \cdot 10^{-6}$	$3.84 \cdot 10^{-3}$	$4.52 \cdot 10^{-2}$
5	0.73	$2.97 \cdot 10^{-5}$	$7.33 \cdot 10^{-6}$	$1.97 \cdot 10^{-2}$	$2.12 \cdot 10^{-1}$
6	5.42	$3.51 \cdot 10^{-5}$	$5.42 \cdot 10^{-5}$	$1.07 \cdot 10^{-1}$	$7.41 \cdot 10^{-1}$
7	6.71	$1.04 \cdot 10^{-4}$	$6.71 \cdot 10^{-5}$	$1.02 \cdot 10^{-1}$	$7.24 \cdot 10^{-1}$
8	5.40	$4.05 \cdot 10^{-5}$	$5.40 \cdot 10^{-5}$	$5.82 \cdot 10^{-2}$	$5.13 \cdot 10^{-1}$
9	6.55	$4.54 \cdot 10^{-5}$	$6.55 \cdot 10^{-5}$	$9.00 \cdot 10^{-2}$	$6.78 \cdot 10^{-1}$
10	1.99	$2.66 \cdot 10^{-5}$	$1.99 \cdot 10^{-5}$	$1.73 \cdot 10^{-2}$	$1.89 \cdot 10^{-1}$
11	54.61	$5.99 \cdot 10^{-4}$	$5.46 \cdot 10^{-4}$	$3.67 \cdot 10^{-1}$	$9.96 \cdot 10^{-1}$
12	990.66	$1.30 \cdot 10^{-2}$	$9.91 \cdot 10^{-3}$	$8.16 \cdot 10^{-1}$	1.00

Table 6.2.: The results of the dedicated simulations with the resulting values for the candidates. For all candidates, except the one in bin 4, 100,000 events were simulated. For the candidate in bin 4 a total of 1,000,000 events was simulated. All probabilities are determined using the QGSJET II-04 model.

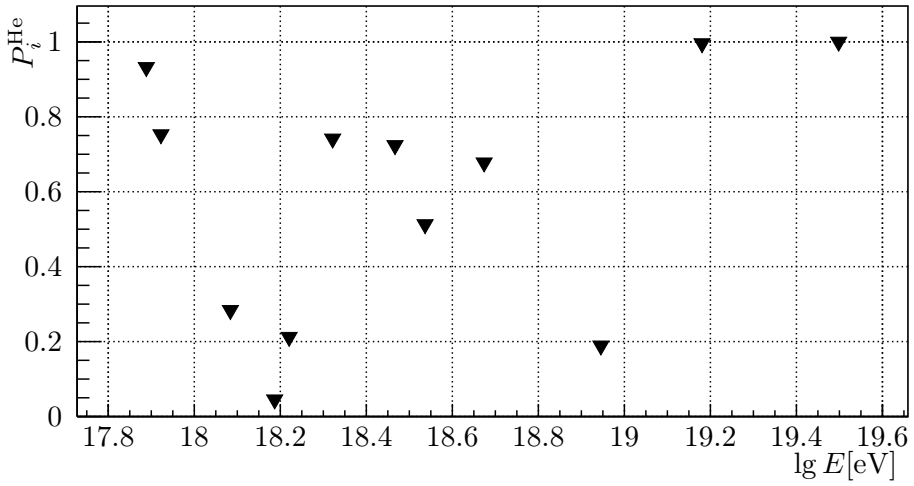

Figure 6.5.: Visualization of the final probabilities for all twelve candidate events in the ICRC 2017 data set [Bel17].

The determined $P^{\mathrm{He}}_{1,i}$ values are in accordance to the values predicted by $p^{\mathrm{He}}_{1,\Delta}$. The differences might be explained by the discrepancies of the averaged detector acceptence to the real acceptance of the specific candidate or in the very conservative handling of the systematic uncertainties.

The results of the dedicated simulations with penalizations for number of events and bins is visualized in figure 6.5.

The lowest probability is $P^{\mathrm{He}}_4 \approx 4.52\,\%$, which leads to the rejection of an Helium origin hypothesis with a confidence level of about 95 % up to an energy of $E \approx (1.54 \pm 0.12)\,\mathrm{EeV}$.

Also the candidate of bin 10 with $P^{\mathrm{He}}_{10} \approx 18.9\,\%$ and an energy of $E \approx (8.71 \pm 0.87)\,\mathrm{EeV}$ is of interest, even though the rejection with a confidence level of about 80 % is not significant.

This first application to the data shows that in principle, very deep proton events could show up this way and, by rejection of the He hypothesis, point to the existence of protons in ultra-high energy cosmic rays.

7 Summary and Outlook

In this work a new method for finding indications on the existence of ultra-high energy primary protons in cosmic rays was presented. The method utilizes the information on the depth of maximum in the longitudinal profiles of the extensive air showers as described in chapter 3. At the preliminary step an individual probability for a shower to be produced by helium is determined for every Auger hybrid event using parametrizations of the X_{max} distributions with the Gumbel function. The calculations take into account the detector effects (resolution and acceptance) and treat reconstruction and systematic uncertainties of the measurements in a conservative way. Events with the minimal probabilities in each of the energy bins are further selected as proton candidates. To take into account the detector and reconstruction effects in the most precise way for all candidate events the single helium probability is determined using dedicated RealMC simulations reproducing the status of the detector components (including the atmosphere) at the time of the registration of each data event. The final probability is obtained by penalizing the single helium probability for the number of total events in the corresponding energy bin and for the total number of bins. The check of the performance of the method in chapter 4 demonstrated that the method works as expected and is able to identify candidate events reliably.

In chapter 6 the presented method was applied to the data of the Pierre Auger Observatory, using the data set prepared by the collaboration for the International Cosmic Ray Conference 2017. The data was divided into twelve energy bins. The twelve selected candidates had preliminary (using Gumbel parameterizations) single event probabilities from the percent level down to the 10^{-6} level, which were further found agreeing well with the outcomes of the dedicated simulations. After the penalization for number of events and number of energy bins the existence of protons can be stated at 95 % CL up to an energy of 1.5 EeV.

This value can not be seen as a definite proof of the existence of protons at the ultra-high energies, but serves as a motivation for further studies. These studies may include the use of other observables sensitive to the electromagnetic-muon ratio from the SD of Auger, allowing one to increase the discrimination power with the combination of observables in a multivariate analysis.

Generally, the increase of statistics can of course help finding protons at highest energies, since even a small fraction of protons in the cosmic

rays will lead to a higher amount of deep showers than one would expect from a pure helium flux.

Another approach to enhance the results of this analysis could reside in a careful revision of the fiducial field-of-view anti-bias cut currently removing around two thirds of the data. Since this analysis does not rely on the unbiased estimation of the overall composition, a data set with a biased mass composition would not affect the conclusions on existence of protons at all. Nevertheless releasing this cut one should take care not to degrade the quality of the reconstructed data.

Another way to improve this analysis might be achieved via the inclusion of multiple candidate events per bin. This idea is based on the observation of two candidate events with similar X_{max}'s in the fifth bin. Even if a single event reaching a certain X_{max} can be expected (with a relatively small probability) for a pure helium flux, the existence of a second event with a comparable depth of maximum might be very unlikely. This should be checked in additional studies in the future.

A Additional plots to chapter 3

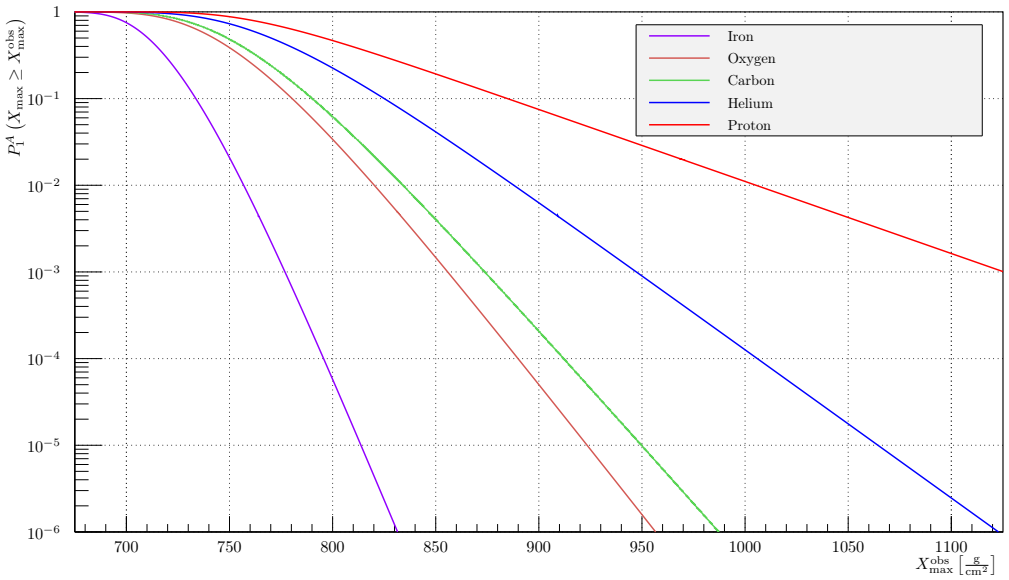

Figure A.1.: Probabilities $p_1\left(X_{\max} \geq X_{\max}^{\text{obs}} \middle| 10^{19}\ \text{eV}, A\right)$ to produce an event with $X_{\max} > X_{\max}^{\text{obs}}$ for several primaries for EPOS-LHC.

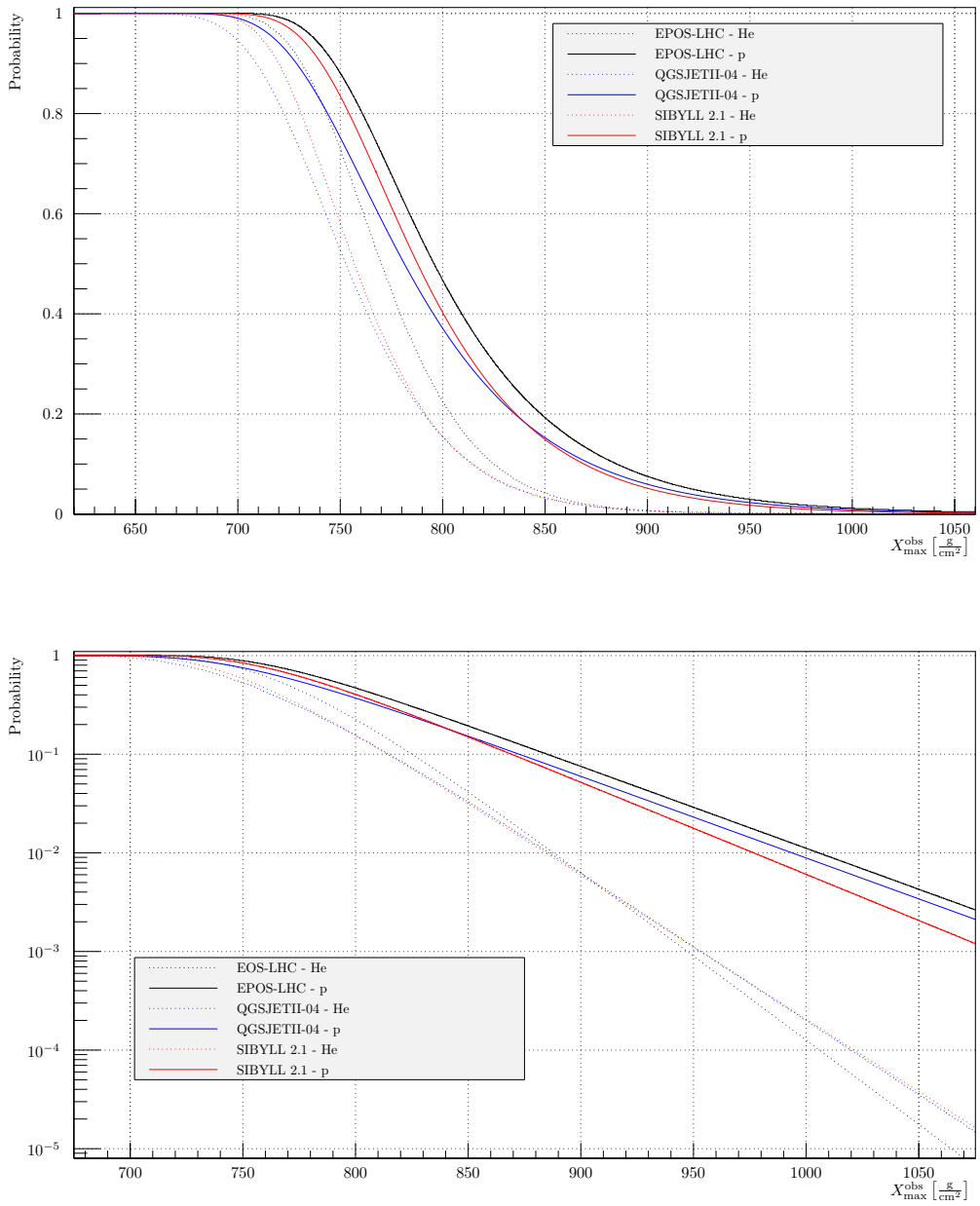

Figure A.2.: Probabilities $p_1\left(X_{\mathrm{max}} \geq X_{\mathrm{max}}^{\mathrm{obs}} \middle| 10^{19}\ \mathrm{eV}, A\right)$ to produce an event with $X_{\mathrm{max}} > X_{\mathrm{max}}^{\mathrm{obs}}$ for protons and helium for different interaction models.

B Selection table

cut	n	[%]
nTot	431172	–
isCLF	431171	100.0
isXLF	431171	100.0
keepHECOorCoihuecoHEAT	321012	74.5
eyeCut	286076	89.1
badFDPeriodRejection	269838	94.3
minMeanPixelRMSMergedEyes	269838	100.0
minMeanPixelRMSSimpleEyes	255529	94.7
badPixels	241174	94.4
good10MHzCorrection	239816	99.4
hasMieDatabase	193077	80.5
maxVAOD	182788	94.7
cloudCutXmaxPRD14	136053	74.4
hybridTankTrigger	130010	95.6
maxCoreTankDist	129316	99.5
maxZenithFD	129316	100.0
minLgEnergyFD	129316	100.0
skipSaturated	128688	99.5
minPBrass	123925	96.3
maxPBrassProtonIronDiff	123621	99.8
minLgEnergyFD	123621	100.0
FidFOVICRC13	27234	22.0
xMaxObsInExpectedFOV	26635	97.8
maxDepthHole	26477	99.4
profileChi2Sigma	26163	98.8
depthTrackLength	26150	100.0

Table B.1.: Selection table of the ICRC 2017 data [Bel17].

C Additional probability distributions

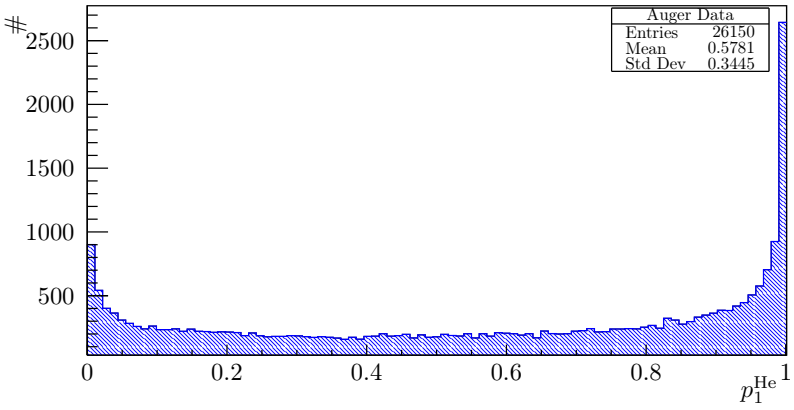

Figure C.1.: The distribution of p_1^{He} in the data set, determined with EPOS-LHC. Since EPOS-LHC expects deeper events in general, the peak $p_1^{He} \to 1$ is higher. For very deep events, EPOS-LHC has a smaller likelihood than QGSJet II-04, for which the peak should be at comparable height.

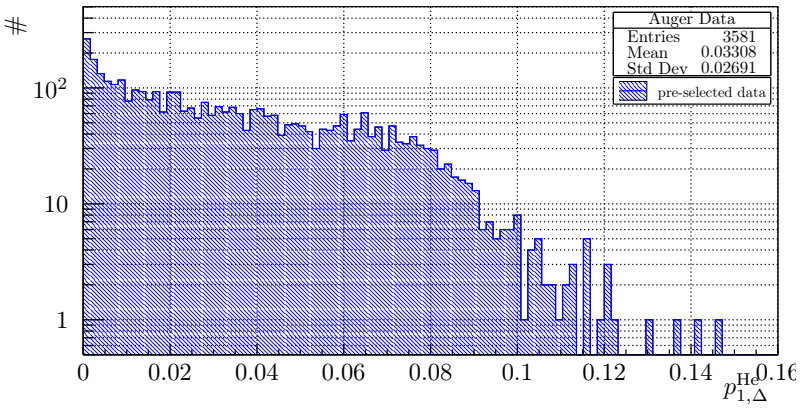

Figure C.2.: The distribution of $p_{1,\Delta}^{He}$ of all events passing the pre-selection criterium, using EPOS-LHC.

D Details of the candidate events

run 2572, event 3749
time stamp: 1072244982 s 271513371 ns
Trigger: 'Physics - Int or L/R trigger', 'Shower Candidate'
in Loma Amarilla mirror 3 (in DAQ: 1 2 3 4 5 6)
geometry: hybrid, station 1274 (ToT), showerPlaneDistance = 290 m
(θ, ϕ) = (41.5±0.9, 294.8±1.6) deg
(x, y) = (4.07±0.04, 25.46±0.08) km
R_p = 7.42 ± 0.10 km
profile: 4-parameter Gaisser-Hillas (type: classic)
E = (7.74 ± 0.40 ± 0.50) × 10^{17} eV
X_{max} = 1003 ± 34 g/cm^2
$(dE/dX)_{max}$ = 1.13 ± 0.05 PeV/(g/cm^2)
$(\lambda, X_0, fwhm)$ = (52±6, -42±110, 548) g/cm^2, f_{asym} = 0.46
Cherenkov-fraction = 0%, mva=0 deg.
databases:
Mie attenuation: measured (h<12.8 km, VAOD at 3km: 0.04)
LIDAR: h(cloud)=100.0 km, 0%; CloudCam: no data; CloudMap: max=0%
molecular profile: GDAS; time correction: good

(a) Overview of the reconstruction of the event.

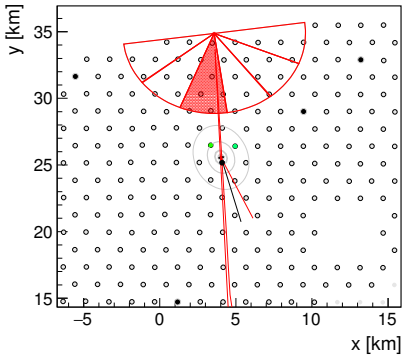

(b) Top view on the geometry reconstruction of the candidate.

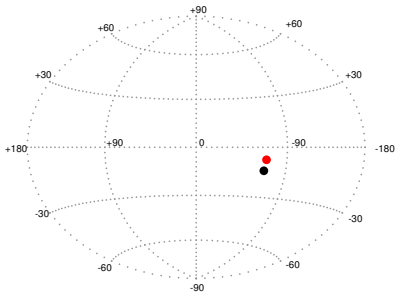

(c) Reconstruction of the direction of the candidate's shower axis.

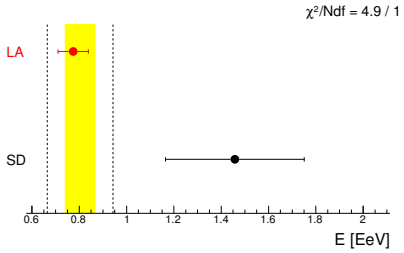

(d) Overview of the successfull energy reconstructions.

Figure D.1.: Candidate in bin 1.

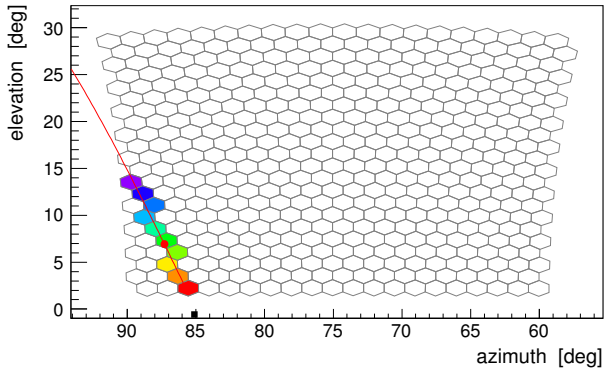

(a) Triggered pixels of the detecting FD site.

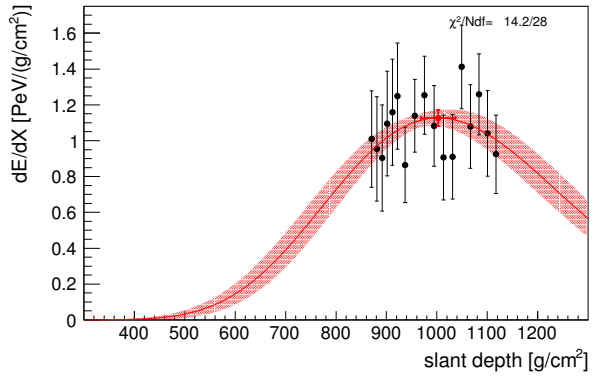

(b) Reconstruction of the candidate's profile with deposited energy and shower maximum.

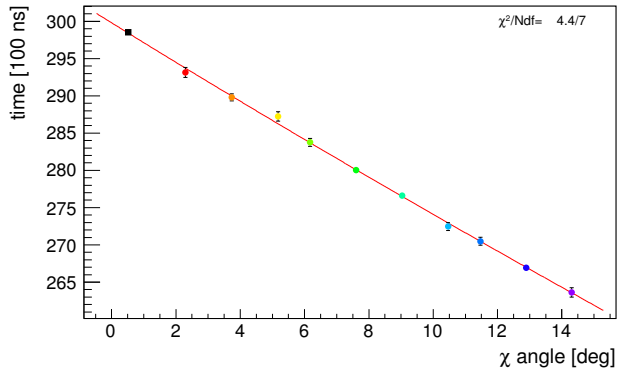

(c) The signal's arriving time of every pixels as a function of the viewing angle χ

Figure D.2.: Candidate in bin 1, Details of the FD reconstruction.

run 3052, event 13700
time stamp: 983867315 s 228850182 ns
Trigger: 'Physics - Int or L/R trigger', 'Shower Candidate'
in Los Morados mirror 1 (in DAQ: 1 2 3 4 5 6)
geometry: hybrid, station 748 (ToT), showerPlaneDistance = 248 m
$(\theta, \phi) = (49.6 \pm 0.6, 121.6 \pm 0.5)$ deg
$(x, y) = (27.10 \pm 0.06, 5.59 \pm 0.06)$ km
$R_p = 10.72 \pm 0.04$ km
profile: 4-parameter Gaisser-Hillas (type: classic)
$E = (8.36 \pm 0.40 \pm 0.39) \times 10^{17}$ eV
$X_{max} = 1009 \pm 28$ g/cm^2
$(dE/dX)_{max} = 1.20 \pm 0.05$ PeV/(g/cm^2)
$(\lambda, X_0, \text{fwhm}) = (53 \pm 7, -45 \pm 135, 555)$ g/cm^2, $f_{asym} = 0.46$
Cherenkov-fraction = 0%, mva=0 deg.
databases:
Mie attenuation: measured (h<13.2 km, VAOD at 3km: 0.04)
LIDAR: no data ; CloudCam: no data; CloudMap: no data
molecular profile: GDAS; time correction: good

(a) Overview of the reconstruction of the event.

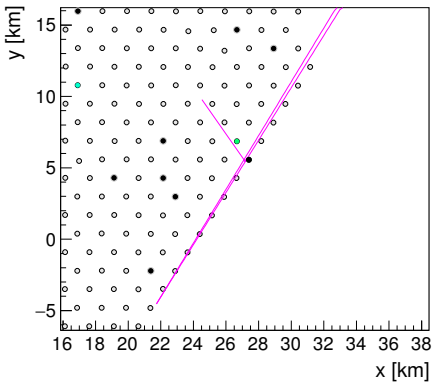

(b) Top view on the geometry reconstruction of the candidate.

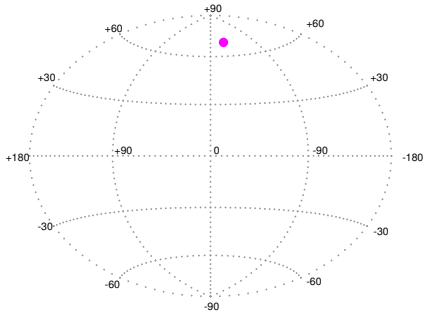

(c) Reconstruction of the direction of the candidate's shower axis.

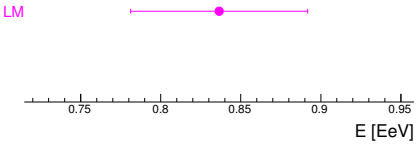

(d) Overview of the successfull energy reconstructions.

Figure D.3.: Candidate in bin 2.

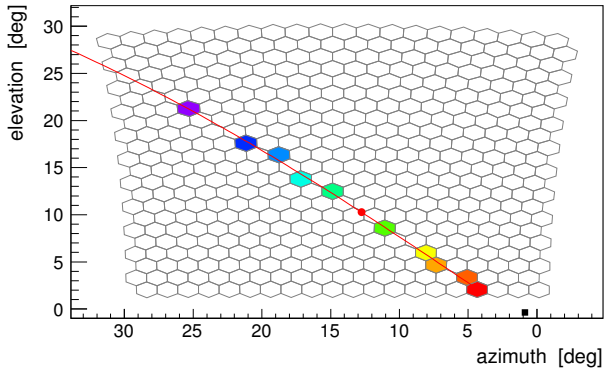

(a) Triggered pixels of the detecting FD site.

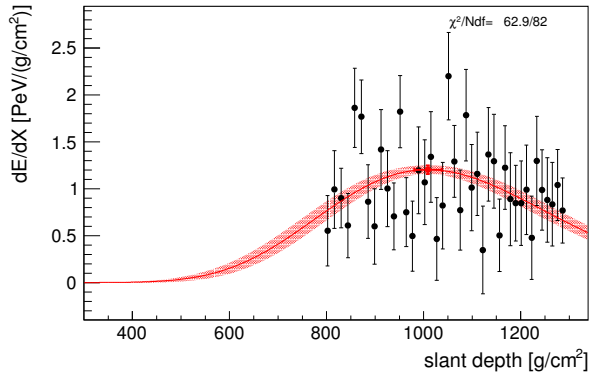

(b) Reconstruction of the candidate's profile with deposited energy and shower maximum.

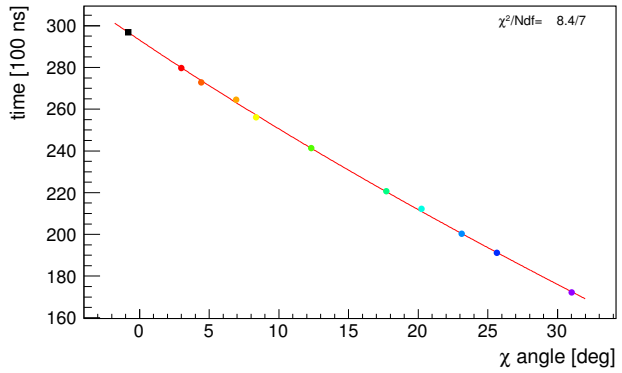

(c) The signal's arriving time of every pixels as a function of the viewing angle χ

Figure D.4.: Candidate in bin 2, Details of the FD reconstruction.

run 1970, event 6947
time stamp: 1014537079 s 844737065 ns
Trigger: 'Physics - Int or L/R trigger', 'Shower Candidate'
in Loma Amarilla mirror 5 6 (in DAQ: 1 2 3 4 5 6)
geometry: hybrid, station 1136 (ToT), showerPlaneDistance = 775 m
(θ, ϕ) = (51.7±0.4, 288.0±0.5) deg
(x, y) = (11.72±0.04, 33.99±0.03) km
R_p = 7.76 ± 0.02 km
profile: 4-parameter Gaisser-Hillas (type: classic)
E = (1.21 ± 0.04 ± 0.06) × 10^{18} eV
X_{max} = 1042 ± 16 g/cm^2
$(dE/dX)_{max}$ = 1.69 ± 0.04 PeV/(g/cm^2)
$(\lambda, X_0, fwhm)$ = (49±6, -179±131, 579) g/cm^2, f_{asym} = 0.46
Cherenkov-fraction = 0%, mva=0 deg.
databases:
Mie attenuation: measured (h<13.2 km, VAOD at 3km: 0.03)
LIDAR: no data ; CloudCam: no data; CloudMap: max=0%
molecular profile: GDAS; time correction: good

(a) Overview of the reconstruction of the event.

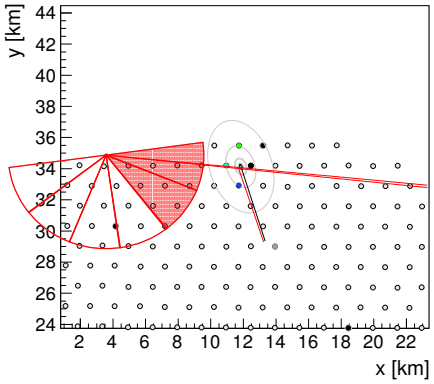

(b) Top view on the geometry reconstruction of the candidate.

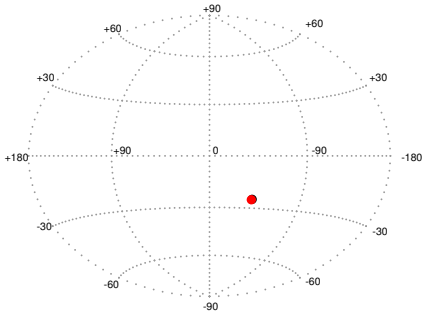

(c) Reconstruction of the direction of the candidate's shower axis.

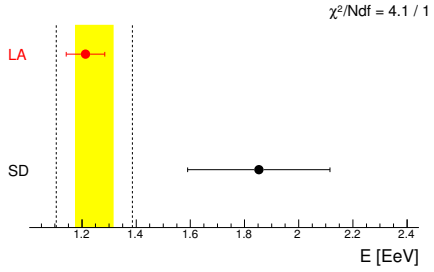

(d) Overview of the successfull energy reconstructions.

Figure D.5.: Candidate in bin 3.

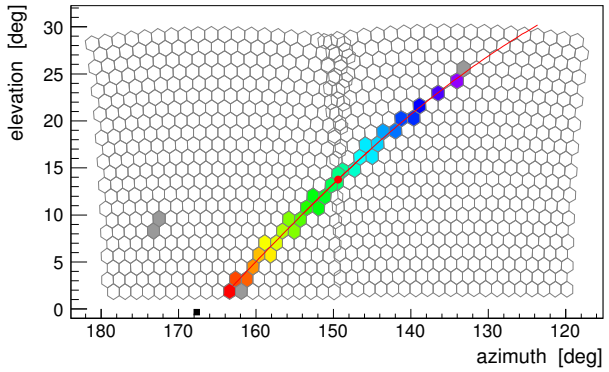

(a) Triggered pixels of the detecting FD site.

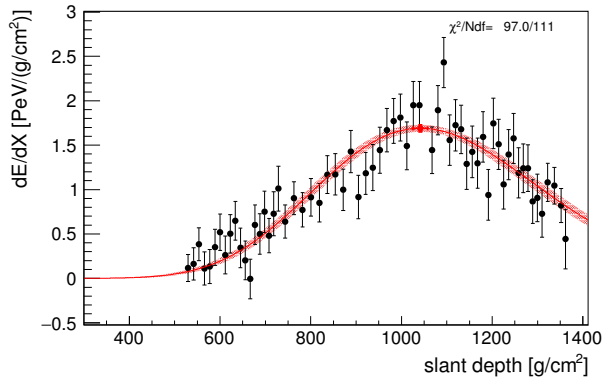

(b) Reconstruction of the candidate's profile with deposited energy and shower maximum.

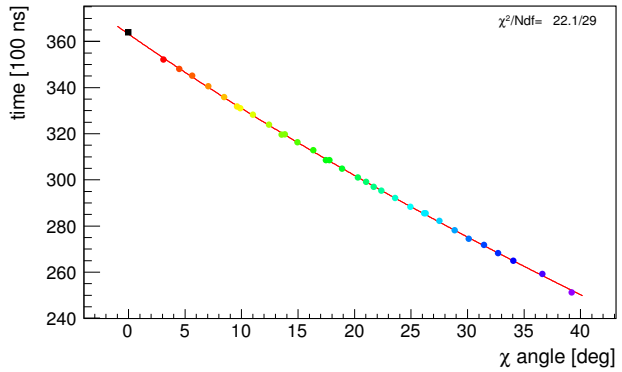

(c) The signal's arriving time of every pixels as a function of the viewing angle χ

Figure D.6.: Candidate in bin 3, Details of the FD reconstruction.

run 2728, event 710
time stamp: 953083570 s 134299185 ns
Trigger: 'Physics - Int or L/R trigger', 'Shower Candidate'
in Los Morados mirror 3 (in DAQ: 1 2 3 4 5 6)
geometry: hybrid, station 775 (ToT), showerPlaneDistance = 498 m
(θ, ϕ) = (50.0±0.7, 177.9±0.6) deg
(x, y) = (16.12±0.05, 4.79±0.06) km
R_p = 10.00 ± 0.04 km
profile: 4-parameter Gaisser-Hillas (type: classic)
E = (1.54 ± 0.06 ± 0.10) × 10^{18} eV
X_{max} = 1104 ± 26 g/cm^2
$(dE/dX)_{max}$ = 2.21 ± 0.07 PeV/(g/cm^2)
$(\lambda, X_0, fwhm)$ = (48±7, -77±139, 564) g/cm^2, f_{asym} = 0.46
Cherenkov-fraction = 0%, mva=0 deg.
databases:
Mie attenuation: measured (h<13.2 km, VAOD at 3km: 0.07)
LIDAR: h(cloud)=100.0 km, 0%; CloudCam: max(ζ)=(40/-100)%; CloudMap: max=0%
molecular profile: GDAS; time correction: good

(a) Overview of the reconstruction of the event.

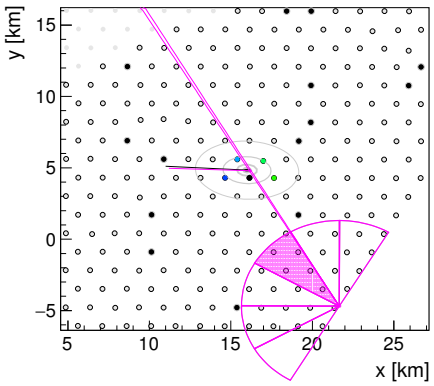

(b) Top view on the geometry reconstruction of the candidate.

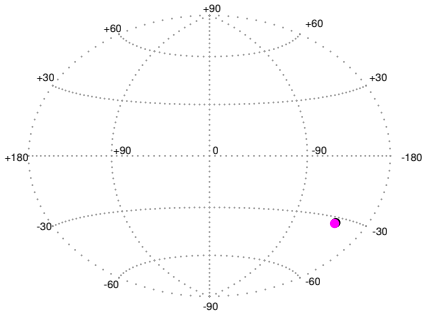

(c) Reconstruction of the direction of the candidate's shower axis.

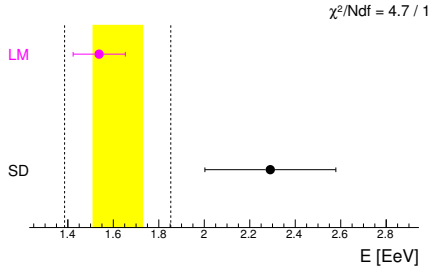

(d) Overview of the successfull energy reconstructions.

Figure D.7.: Candidate in bin 4.

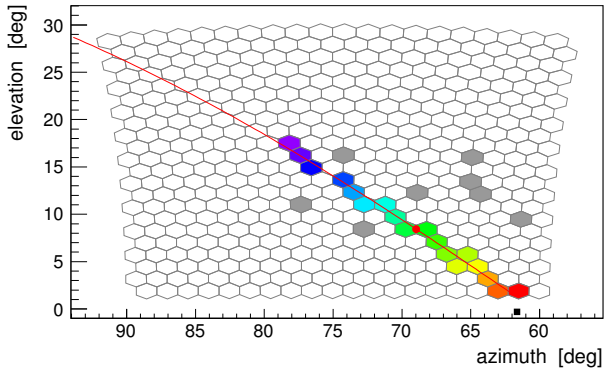

(a) Triggered pixels of the detecting FD site.

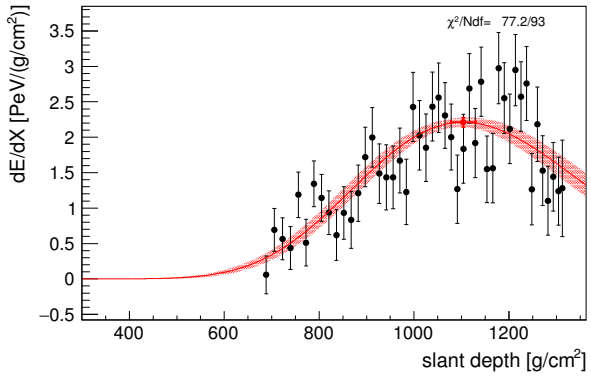

(b) Reconstruction of the candidate's profile with deposited energy and shower maximum.

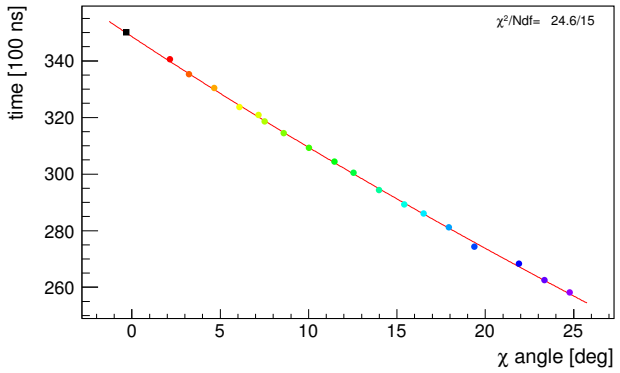

(c) The signal's arriving time of every pixels as a function of the viewing angle χ

Figure D.8.: Candidate in bin 4, Details of the FD reconstruction.

run 2657, event 6498
time stamp: 899185799 s 249769430 ns
Trigger: 'Physics - Int or L/R trigger', 'Shower Candidate'
in Coihueco mirror 3 (in DAQ: 1 2 3 4 5 6)
geometry: hybrid, station 1033 (ToT), showerPlaneDistance = 164 m
(θ, ϕ) = (70.7±0.3, 262.6±1.8) deg
(x, y) = (-16.13±0.29, 23.57±0.37) km
R_p = 14.96 ± 0.04 km
profile: 4-parameter Gaisser-Hillas (type: classic)
E = (1.66 ± 0.07 ± 0.06) × 10^{18} eV
X_{max} = 1020 ± 24 g/cm^2
$(dE/dX)_{max}$ = 2.41 ± 0.07 PeV/(g/cm^2)
$(\lambda, X_0, fwhm)$ = (53±7, -47±137, 559) g/cm^2, f_{asym} = 0.46
Cherenkov-fraction = 0%, mva=0 deg.
databases:
Mie attenuation: measured (h<11.7 km, VAOD at 3km: 0.00)
LIDAR: no data ; CloudCam: max(ζ)=(0/-100)%; CloudMap: max=40%
molecular profile: GDAS; time correction: good

(a) Overview of the reconstruction of the event.

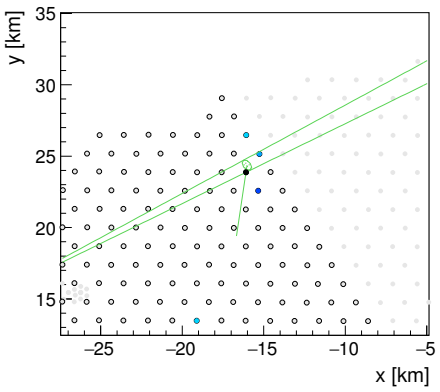

(b) Top view on the geometry reconstruction of the candidate.

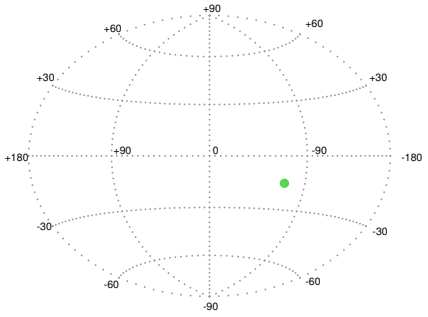

(c) Reconstruction of the direction of the candidate's shower axis.

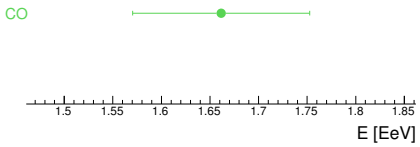

(d) Overview of the successfull energy reconstructions.

Figure D.9.: Candidate in bin 5.

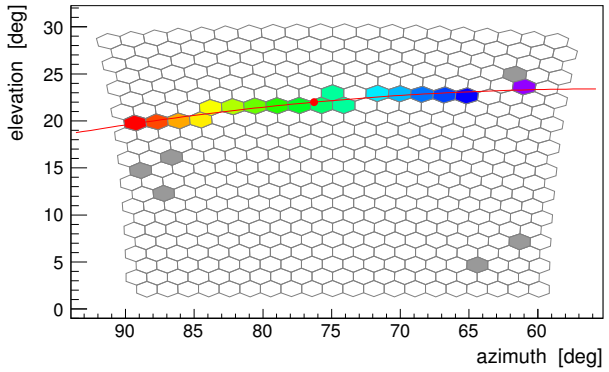

(a) Triggered pixels of the detecting FD site.

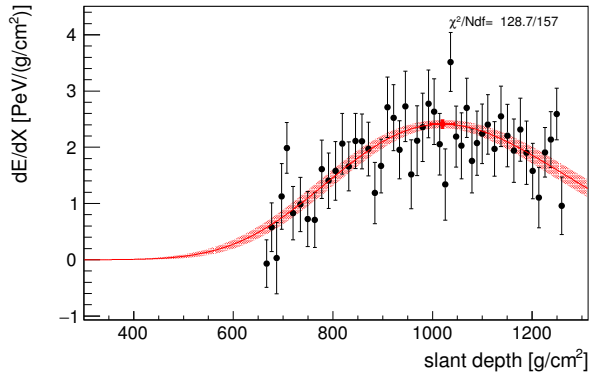

(b) Reconstruction of the candidate's profile with deposited energy and shower maximum.

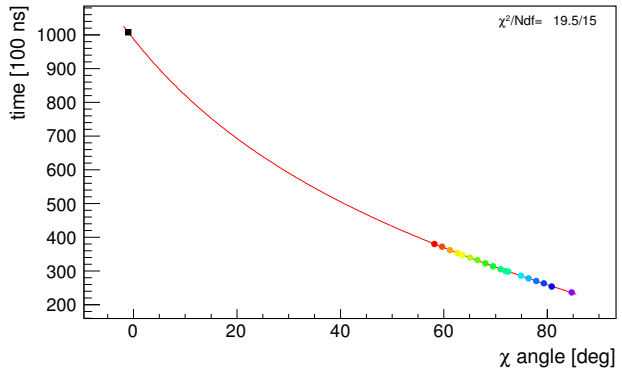

(c) The signal's arriving time of every pixels as a function of the viewing angle χ

Figure D.10.: Candidate in bin 5, Details of the FD reconstruction.

run 3832, event 1765
time stamp: 982734446 s 163821960 ns
Trigger: 'Physics - Int or L/R trigger', 'Shower Candidate'
in Coihueco mirror 2 (in DAQ: 1 2 3 4 5 6)
geometry: hybrid, station 640 (ToT), showerPlaneDistance = 170 m
(θ, ϕ) = (51.5±0.5, 236.3±0.5) deg
(x, y) = (-26.13±0.05, 6.54±0.05) km
R_p = 9.80 ± 0.03 km
profile: 4-parameter Gaisser-Hillas (type: classic)
E = (2.10 ± 0.07 ± 0.09) × 10^{18} eV
X_{max} = 1012 ± 19 g/cm^2
$(dE/dX)_{max}$ = 3.04 ± 0.08 PeV/(g/cm^2)
$(\lambda, X_0, fwhm)$ = (52±8, -72±149, 562) g/cm^2, f_{asym} = 0.46
Cherenkov-fraction = 0%, mva=0 deg.
databases:
Mie attenuation: measured (h<13.2 km, VAOD at 3km: 0.03)
LIDAR: h(cloud)=100.0 km, 0%; CloudCam: max(ζ)=(0/-100)%; CloudMap: no data
molecular profile: GDAS; time correction: good

(a) Overview of the reconstruction of the event.

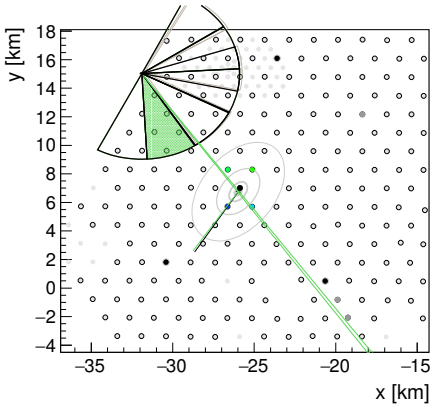

(b) Top view on the geometry reconstruction of the candidate.

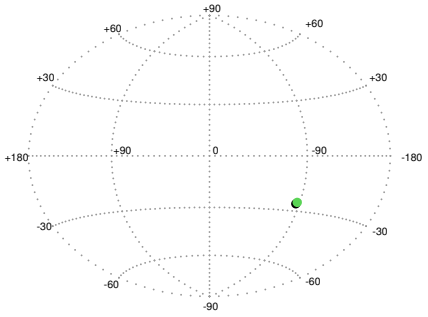

(c) Reconstruction of the direction of the candidate's shower axis.

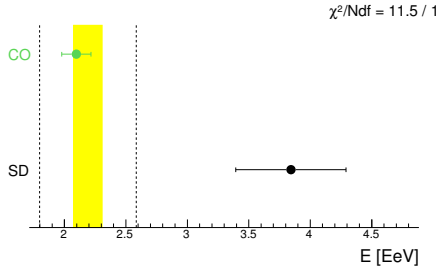

(d) Overview of the successfull energy reconstructions.

Figure D.11.: Candidate in bin 6.

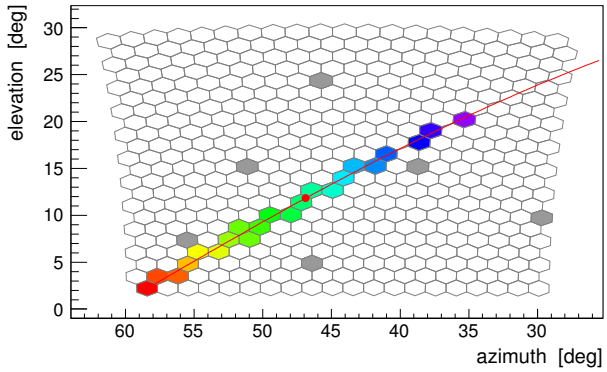

(a) Triggered pixels of the detecting FD site.

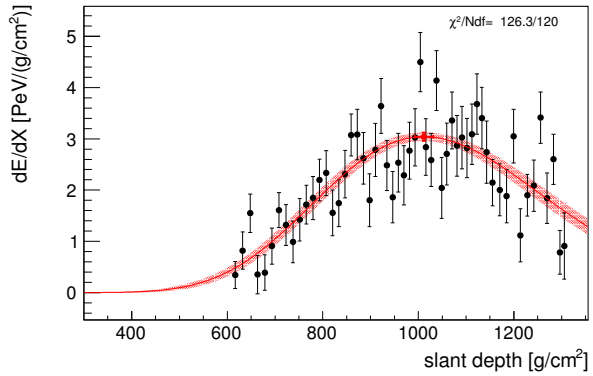

(b) Reconstruction of the candidate's profile with deposited energy and shower maximum.

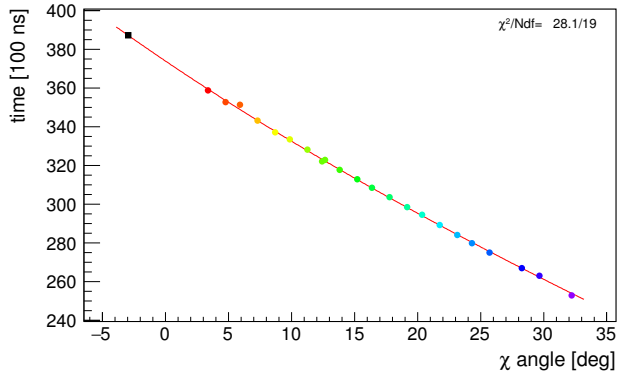

(c) The signal's arriving time of every pixels as a function of the viewing angle χ

Figure D.12.: Candidate in bin 6, Details of the FD reconstruction.

run 3228, event 757
time stamp: 935023542 s 524867076 ns
Trigger: 'Physics - Int or L/R trigger', 'Shower Candidate'
in Coihueco mirror 6 (in DAQ: 1 2 3 4 5 6)
geometry: hybrid, station 1027 (ToT), showerPlaneDistance = 336 m
(θ, ϕ) = (45.7±0.7, 97.5±0.5) deg
(x, y) = (-24.32±0.05, 23.26±0.05) km
R_p = 9.94 ± 0.03 km
profile: 4-parameter Gaisser-Hillas (type: classic)
E = (2.93 ± 0.12 ± 0.10) × 10^{18} eV
X_{max} = 1001 ± 21 g/cm^2
$(dE/dX)_{max}$ = 4.33 ± 0.09 PeV/(g/cm^2)
$(\lambda, X_0, fwhm)$ = (52±8, -52±135, 552) g/cm^2, f_{asym} = 0.46
Cherenkov-fraction = 0%, mva=0 deg.
databases:
Mie attenuation: measured (h<10.0 km, VAOD at 3km: 0.01)
LIDAR: h(cloud)=7.7 km, 91%; CloudCam: max(ζ)=(100/-100)%; CloudMap: no data
molecular profile: GDAS; time correction: good

(a) Overview of the reconstruction of the event.

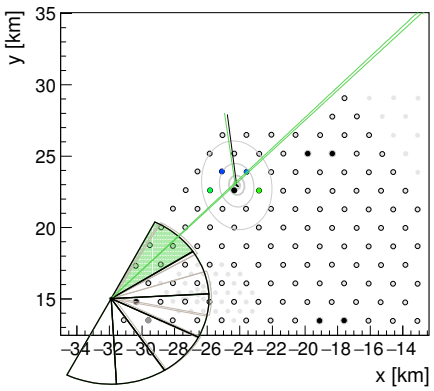

(b) Top view on the geometry reconstruction of the candidate.

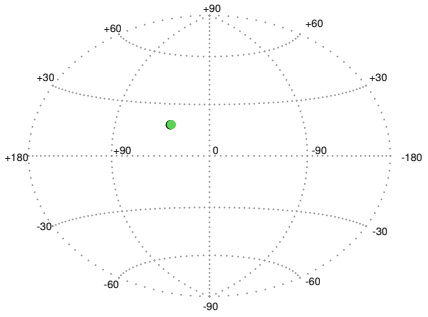

(c) Reconstruction of the direction of the candidate's shower axis.

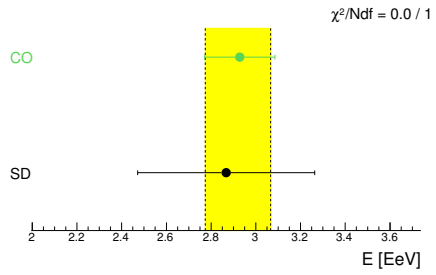

(d) Overview of the successfull energy reconstructions.

Figure D.13.: Candidate in bin 7.

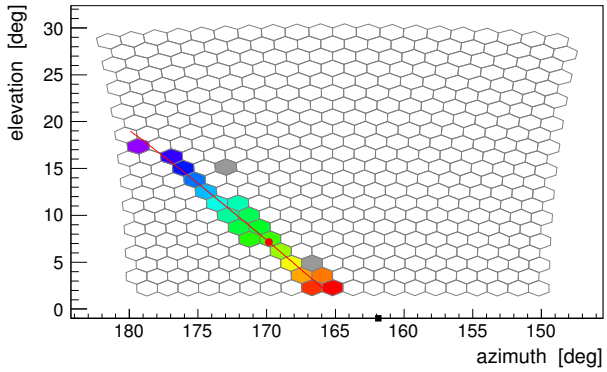

(a) Triggered pixels of the detecting FD site.

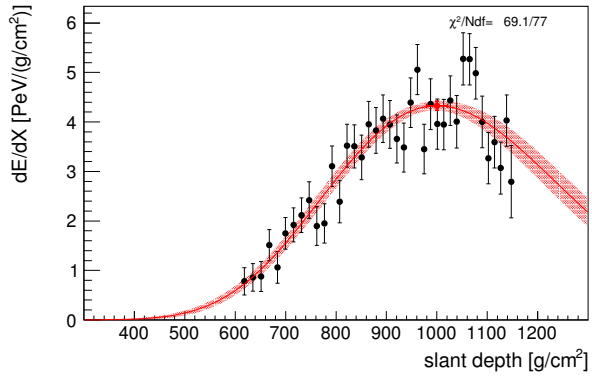

(b) Reconstruction of the candidate's profile with deposited energy and shower maximum.

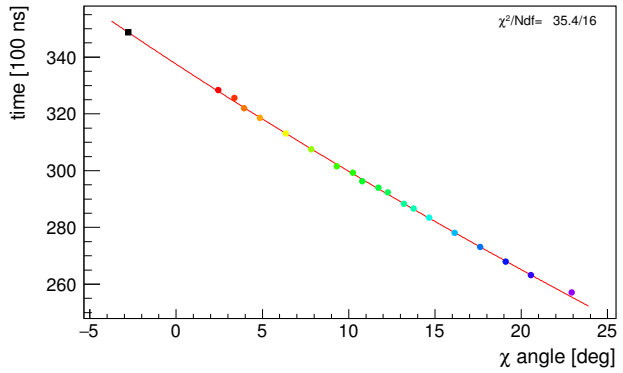

(c) The signal's arriving time of every pixels as a function of the viewing angle χ

Figure D.14.: Candidate in bin 7, Details of the FD reconstruction.

run 3731, event 5682
time stamp: 970464604 s 227241442 ns
Trigger: 'Physics - Int or L/R trigger', 'Shower Candidate'
in Coihueco mirror 2 (in DAQ: 1 2 3 4 5 6)
geometry: hybrid, station 1071 (ToT), showerPlaneDistance = 591 m
(θ, ϕ) = (51.9±0.7, 228.7±0.5) deg
(x, y) = (-27.18±0.07, 1.13±0.06) km
R_p = 13.47 ± 0.05 km
profile: 4-parameter Gaisser-Hillas (type: classic)
E = (3.44 ± 0.14 ± 0.20) × 10^{18} eV
X_{max} = 1034 ± 32 g/cm^2
$(dE/dX)_{max}$ = 4.85 ± 0.14 PeV/(g/cm^2)
(λ, X_0, fwhm) = (54±8, -85±154, 579) g/cm^2, f_{asym} = 0.46
Cherenkov-fraction = 0%, mva=0 deg.
databases:
Mie attenuation: measured (h<13.2 km, VAOD at 3km: 0.04)
LIDAR: h(cloud)=100.0 km, 0%; CloudCam: max(ζ)=(0/-100)%; CloudMap: no data
molecular profile: GDAS; time correction: good

(a) Overview of the reconstruction of the event.

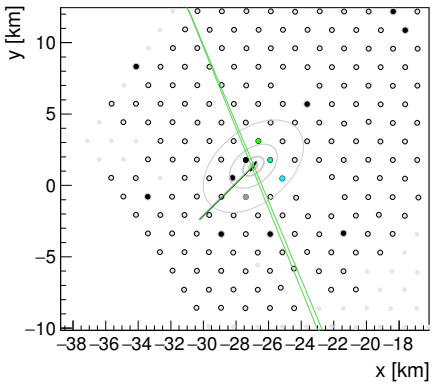

(b) Top view on the geometry reconstruction of the candidate.

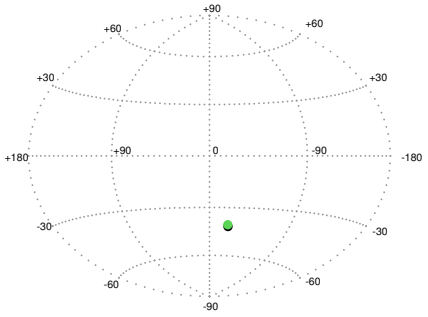

(c) Reconstruction of the direction of the candidate's shower axis.

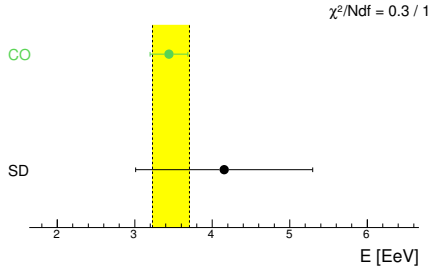

(d) Overview of the successfull energy reconstructions.

Figure D.15.: Candidate in bin 8.

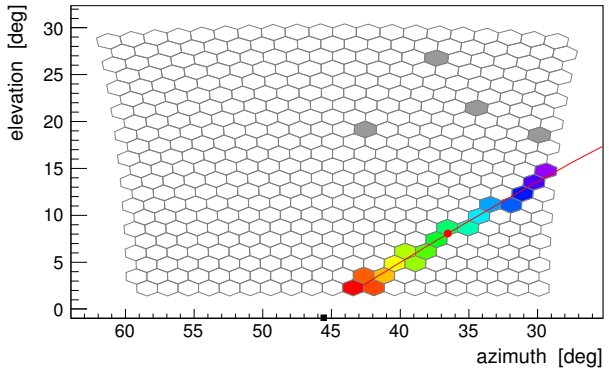

(a) Triggered pixels of the detecting FD site.

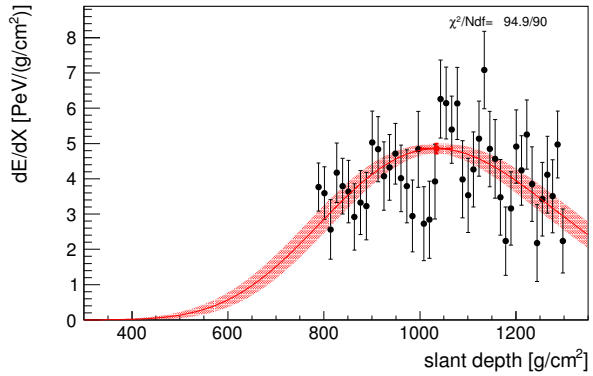

(b) Reconstruction of the candidate's profile with deposited energy and shower maximum.

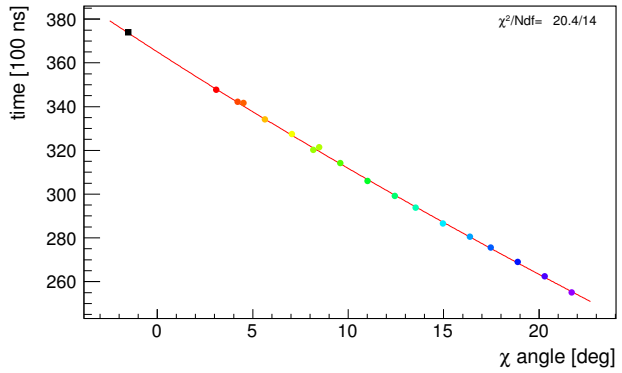

(c) The signal's arriving time of every pixels as a function of the viewing angle χ

Figure D.16.: Candidate in bin 8, Details of the FD reconstruction.

run 2556, event 3266
time stamp: 1069735265 s 678256182 ns
Trigger: 'Physics - Int or L/R trigger', 'Shower Candidate'
in Loma Amarilla mirror 3 4 (in DAQ: 1 2 3 4 5 6)
geometry: hybrid, station 1431 (ToT), showerPlaneDistance = 606 m
(θ, ϕ) = (44.7±0.3, 68.7±0.7) deg
(x, y) = (3.58±0.05, 17.34±0.02) km
R_p = 13.28 ± 0.03 km
profile: 4-parameter Gaisser-Hillas (type: classic)
E = (4.72 ± 0.22 ± 0.32) × 10^{18} eV
X_{max} = 1022 ± 16 g/cm^2
$(dE/dX)_{max}$ = 6.55 ± 0.20 PeV/(g/cm^2)
$(\lambda, X_0, fwhm)$ = (51±6, -195±116, 590) g/cm^2, f_{asym} = 0.46
Cherenkov-fraction = 0%, mva=0 deg.
databases:
Mie attenuation: measured (h<13.2 km, VAOD at 3km: 0.02)
LIDAR: h(cloud)=100.0 km, 0%; CloudCam: no data; CloudMap: max=0%
molecular profile: GDAS; time correction: good

(a) Overview of the reconstruction of the event.

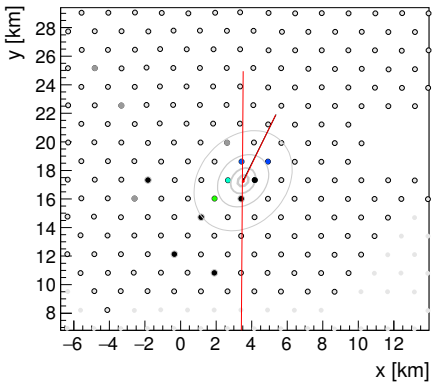

(b) Top view on the geometry reconstruction of the candidate.

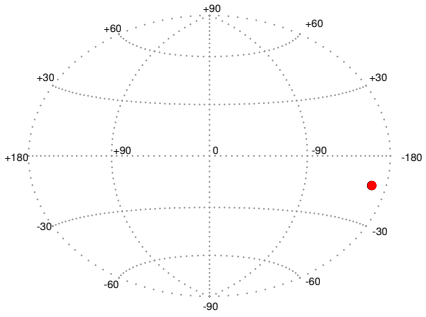

(c) Reconstruction of the direction of the candidate's shower axis.

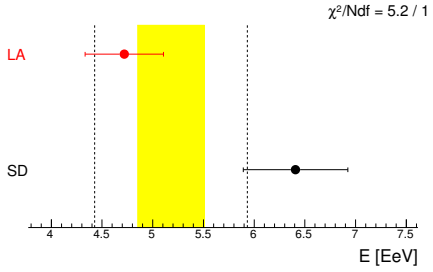

(d) Overview of the successfull energy reconstructions.

Figure D.17.: Candidate in bin 9.

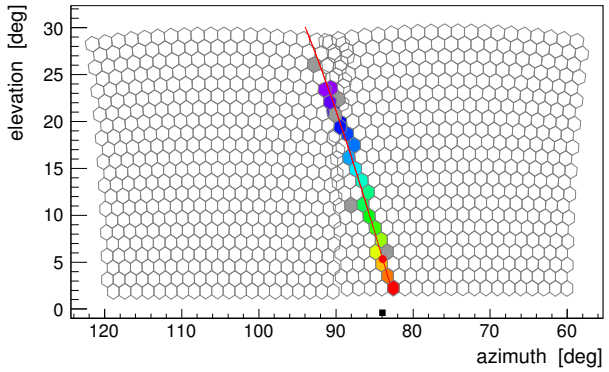

(a) Triggered pixels of the detecting FD site.

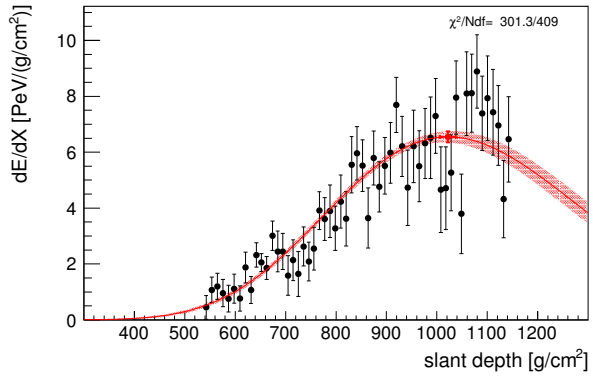

(b) Reconstruction of the candidate's profile with deposited energy and shower maximum.

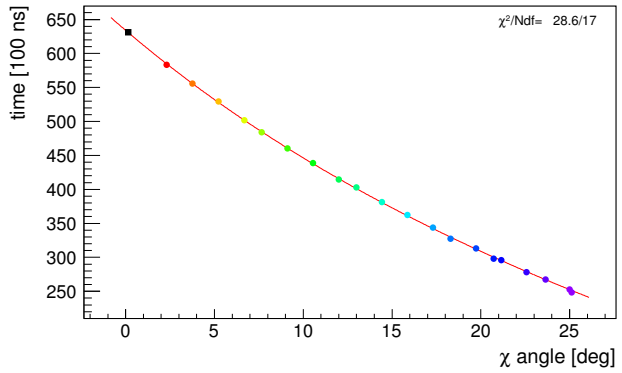

(c) The signal's arriving time of every pixels as a function of the viewing angle χ

Figure D.18.: Candidate in bin 9, Details of the FD reconstruction.

run 1425, event 21914
time stamp: 863067276 s 971401917 ns
Trigger: 'Physics - Int or L/R trigger', 'Shower Candidate'
in Los Morados mirror 3 4 (in DAQ: 1 2 3 4 5 6)
geometry: hybrid, station 696 (ToT), showerPlaneDistance = 1221 m
$(\theta, \phi) = (43.3 \pm 1.0, 87.9 \pm 0.5)$ deg
$(x, y) = (6.71 \pm 0.06, 0.96 \pm 0.07)$ km
$R_p = 15.58 \pm 0.04$ km
profile: 4-parameter Gaisser-Hillas (type: classic)
$E = (8.82 \pm 0.42 \pm 0.76) \times 10^{18}$ eV
$X_{max} = 1062 \pm 28$ g/cm^2
$(dE/dX)_{max} = 13.14 \pm 0.35$ PeV/(g/cm^2)
$(\lambda, X_0, \text{fwhm}) = (52 \pm 7, 7 \pm 112, 552)$ g/cm^2, $f_{asym} = 0.46$
Cherenkov-fraction = 0%, mva=0 deg.
databases:
Mie attenuation: measured (h<9.2 km, VAOD at 3km: 0.03)
LIDAR: h(cloud)=8.4 km, 14%; CloudCam: max(ζ)=(100/-100)%; CloudMap: max=40%
molecular profile: GDAS; time correction: good

(a) Overview of the reconstruction of the event.

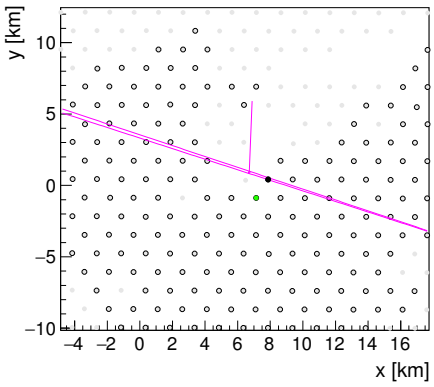

(b) Top view on the geometry reconstruction of the candidate.

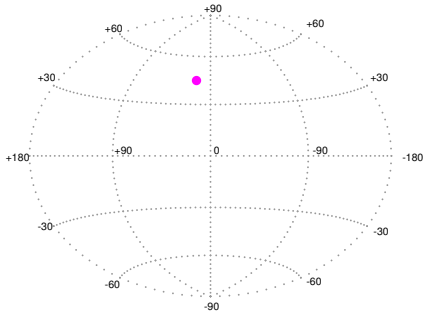

(c) Reconstruction of the direction of the candidate's shower axis.

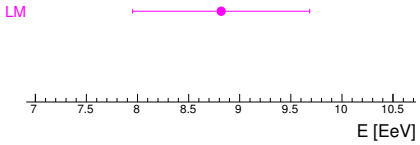

(d) Overview of the successfull energy reconstructions.

Figure D.19.: Candidate in bin 10.

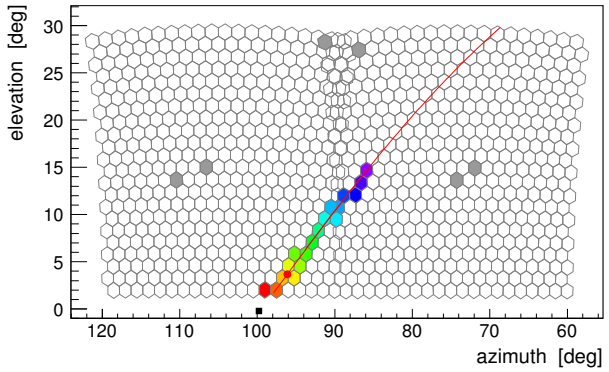

(a) Triggered pixels of the detecting FD site.

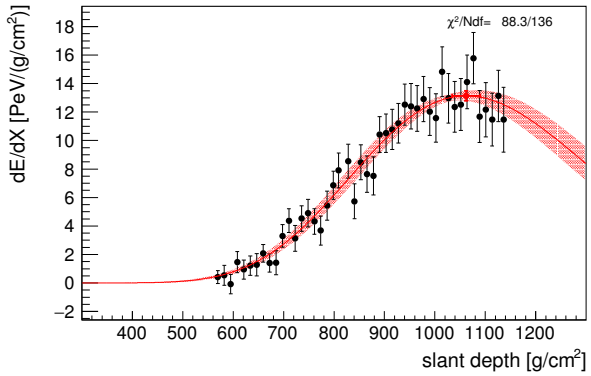

(b) Reconstruction of the candidate's profile with deposited energy and shower maximum.

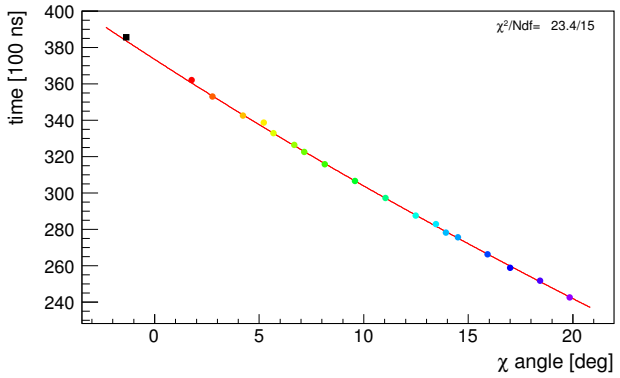

(c) The signal's arriving time of every pixels as a function of the viewing angle χ

Figure D.20.: Candidate in bin 10, Details of the FD reconstruction.

run 2909, event 4247
time stamp: 965979621 s 521242939 ns
Trigger: 'Physics - Int or L/R trigger', 'Shower Candidate'
in Los Morados mirror 1 2 (in DAQ: 1 2 3 4 5 6)
geometry: hybrid, station 1512 (ToT), showerPlaneDistance = 205 m
(θ, ϕ) = (50.1±0.3, 327.7±0.4) deg
(x, y) = (16.33±0.06, 14.81±0.04) km
R_p = 16.69 ± 0.03 km
profile: 4-parameter Gaisser-Hillas (type: classic)
E = (1.52 ± 0.04 ± 0.10) × 10^{19} eV
X_{max} = 973 ± 14 g/cm^2
$(dE/dX)_{max}$ = 21.75 ± 0.34 PeV/(g/cm^2)
$(\lambda, X_0, fwhm)$ = (53±7, -151±109, 575) g/cm^2, f_{asym} = 0.46
Cherenkov-fraction = 0%, mva=0 deg.
databases:
Mie attenuation: measured (h<4.9 km, VAOD at 3km: 0.03)
LIDAR: no data ; CloudCam: max(ζ)=(100/-100)%; CloudMap: max=20%
molecular profile: GDAS; time correction: good

(a) Overview of the reconstruction of the event.

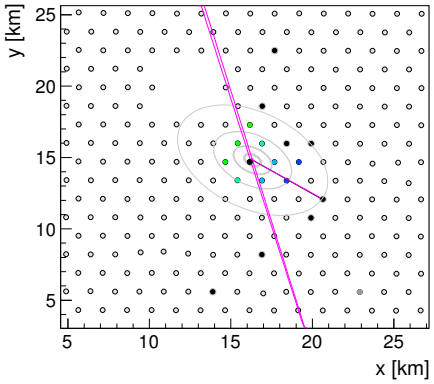

(b) Top view on the geometry reconstruction of the candidate.

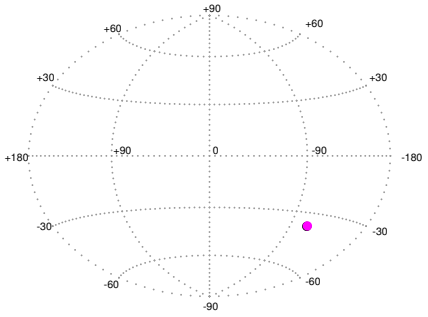

(c) Reconstruction of the direction of the candidate's shower axis.

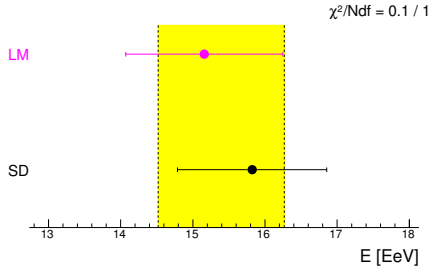

(d) Overview of the successfull energy reconstructions.

Figure D.21.: Candidate in bin 11.

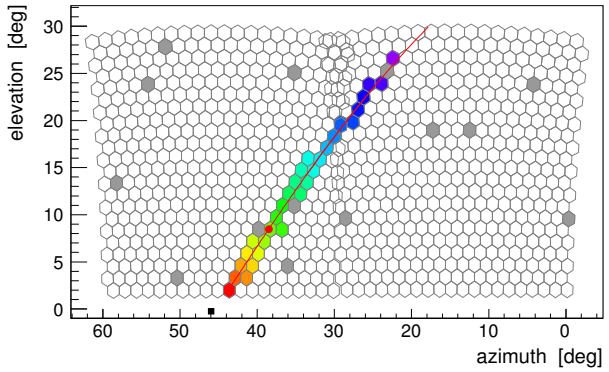

(a) Triggered pixels of the detecting FD site.

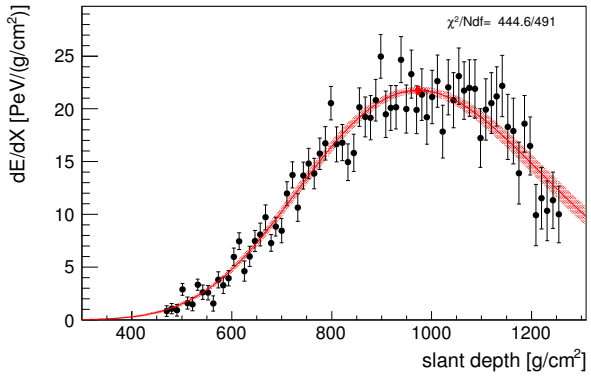

(b) Reconstruction of the candidate's profile with deposited energy and shower maximum.

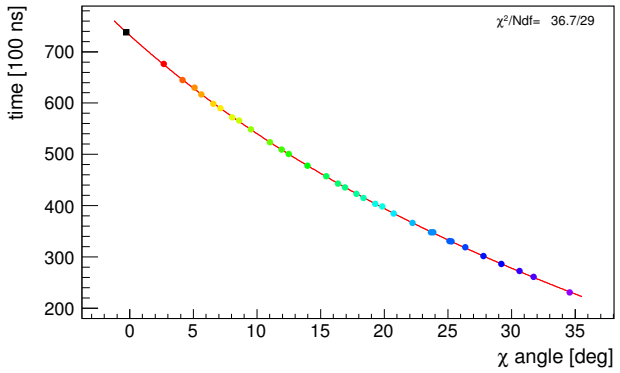

(c) The signal's arriving time of every pixels as a function of the viewing angle χ

Figure D.22.: Candidate in bin 11, Details of the FD reconstruction.

run 3066, event 5762
time stamp: 924421566 s 323971481 ns
Trigger: 'Physics - Int or L/R trigger', 'Shower Candidate'
in Coihueco mirror 5 (in DAQ: 1 2 3 4 5 6)
geometry: hybrid, station 1201 (ToT), showerPlaneDistance = 389 m
(θ, ϕ) = (55.0±0.2, 181.9±0.6) deg
(x, y) = (-8.15±0.04, 22.17±0.08) km
R_p = 15.22 ± 0.03 km
profile: 4-parameter Gaisser-Hillas (type: classic)
E = (3.15 ± 0.06 ± 0.18) × 10^{19} eV
X_{max} = 904 ± 8 g/cm^2
$(dE/dX)_{max}$ = 47.10 ± 0.49 PeV/(g/cm^2)
$(\lambda, X_0,$ fwhm) = (68±7, 95±70, 553) g/cm^2, f_{asym} = 0.44
Cherenkov-fraction = 0%, mva=0 deg.
databases:
Mie attenuation: measured (h<13.2 km, VAOD at 3km: 0.01)
LIDAR: no data ; CloudCam: no data; CloudMap: max=20%
molecular profile: GDAS; time correction: good

(a) Overview of the reconstruction of the event.

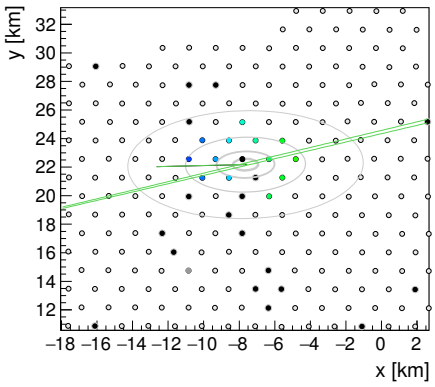

(b) Top view on the geometry reconstruction of the candidate.

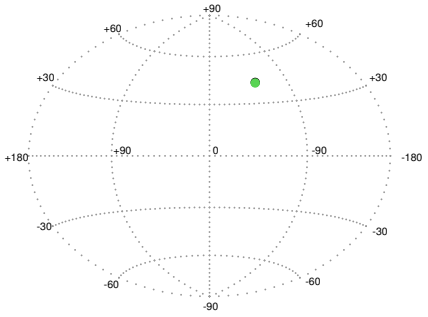

(c) Reconstruction of the direction of the candidate's shower axis.

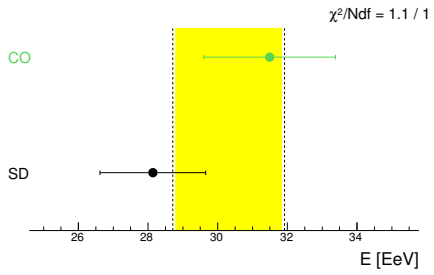

(d) Overview of the successfull energy reconstructions.

Figure D.23.: Candidate in bin 12.

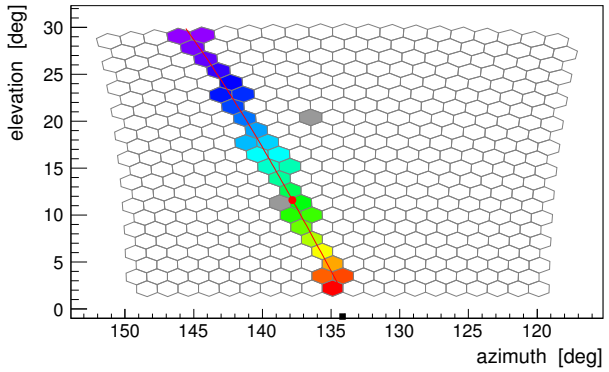

(a) Triggered pixels of the detecting FD site.

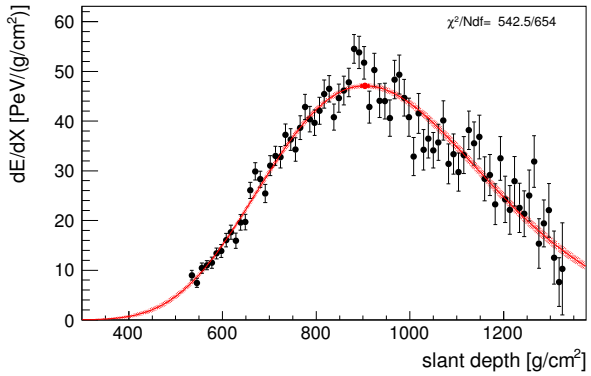

(b) Reconstruction of the candidate's profile with deposited energy and shower maximum.

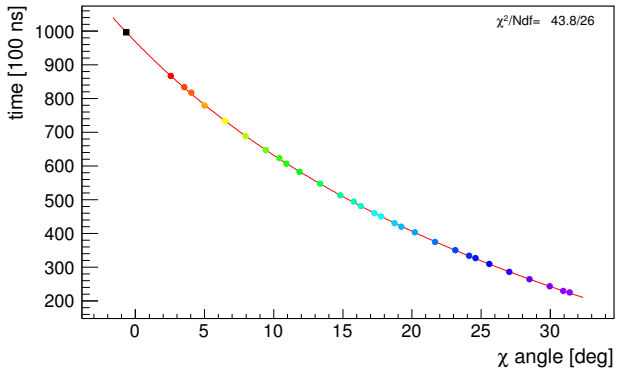

(c) The signal's arriving time of every pixels as a function of the viewing angle χ

Figure D.24.: Candidate in bin 12, Details of the FD reconstruction.

E Bibliography

[Aab14] Aab, A. et al. (Pierre Auger Collaboration). *Depth of maximum of air-shower profiles at the Pierre Auger Observatory: Measurements at energies above* $10^{17.8}$ *eV*. *Phys. Rev.*, D90(12):p. 122005 (2014). doi:10.1103/PhysRevD.90.122005. 1409.4809.

[Aab15] Aab, A. et al. (Pierre Auger Collaboration). *Searches for anisotropies in the arrival directions of the highest energy cosmic rays detected by the Pierre Auger Observatory*. *The Astrophysical Journal*, 804(1):p. 15 (2015).

[Aab17] Aab, A. et al. (Pierre Auger Collaboration). *Search for photons with energies above* 10^{18} eV *using the hybrid detector of the Pierre Auger Observatory*. *Journal of Cosmology and Astroparticle Physics*, 2017(04):p. 009 (2017).

[Abb10] Abbasi, R. et al. (High Resolution Flys Eye Collaboration). *Indications of proton-dominated cosmic-ray composition above 1.6 EeV*. *Physical Review Letters*, 104(16):p. 161101 (2010).

[Abb13] Abbasi, R. et al. (IceCube Collaboration). *IceTop: The surface component of IceCube*. *Nuclear Instruments and Methods in Physics Research Section A: Accelerators, Spectrometers, Detectors and Associated Equipment*, 700:pp. 188–220 (2013).

[Abra] Abraham, J. et al. (Pierre Auger Collaboration). *The fluorescence detector of the Pierre Auger Observatory*. *Nuclear Instruments and Methods in Physics Research Section A: Accelerators, Spectrometers, Detectors and Associated Equipment*, (2–3):pp. 227–251. ISSN 0168-9002. doi:10.1016/j.nima.2010.04.023.

[Abrb] Abraham, J. et al. (Pierre Auger Collaboration). *Trigger and aperture of the surface detector array of the Pierre Auger Observatory*. *Nuclear Instruments and Methods in Physics Research Section A: Accelerators, Spectrometers, Detectors and Associated Equipment*, (1):pp. 29–39. ISSN 0168-9002. doi:10.1016/j.nima.2009.11.018.

[Abr10] Abraham, J. et al. (Pierre Auger Collaboration). *Measurement of the depth of maximum of extensive air showers above* 10^{18} *eV*. *Physical review letters*, 104(9):p. 091101 (2010).

[Ahn09] Ahn, E.-J. et al. *Cosmic ray interaction event generator SIBYLL 2.1. Physical Review D*, 80(9):p. 094003 (2009).

[All08] Allekotte, I. et al. (Pierre Auger Collaboration). *The Surface Detector System of the Pierre Auger Observatory. Nucl. Instrum. Meth.*, A586:pp. 409–420 (2008). doi:10.1016/j.nima.2007.12.016. 0712.2832.

[Amb] Ambrosio, M. et al. *The camera of the Pierre Auger Observatory Fluorescence Detector. Nuclear Instruments and Methods in Physics Research Section A: Accelerators, Spectrometers, Detectors and Associated Equipment*, (1):pp. 125–129. ISSN 0168-9002. doi:10.1016/S0168-9002(01)01731-4. Proceedings of the ninth Int.Conf. on Instrumentation.

[Aug39] Auger, P. et al. *Extensive cosmic-ray showers. Reviews of Modern Physics*, 11(3-4):pp. 288–291 (1939).

[Bel17] Bellido, J. (Pierre Auger Collaboration). *Depth of maximum of air-shower profiles at the Pierre Auger Observatory: Measurements above* $10^{17.2}$ *eV and Composition Implications*. In *The Pierre Auger Observatory: Contributions to the 35th International Cosmic Ray Conference (ICRC 2017)*, pp. 40–47 (2017). URL http://inspirehep.net/record/1618417/files/1617990_40-47.pdf.

[Ben] BenZvi, S. et al. *The Lidar system of the Pierre Auger Observatory. Nuclear Instruments and Methods in Physics Research Section A: Accelerators, Spectrometers, Detectors and Associated Equipment*, (1):pp. 171–184. ISSN 0168-9002. doi:10.1016/j.nima.2007.01.094.

[Ber] Bertou, X. et al. (Pierre Auger Collaboration). *Calibration of the surface array of the Pierre Auger Observatory. Nuclear Instruments and Methods in Physics Research Section A: Accelerators, Spectrometers, Detectors and Associated Equipment*, (2):pp. 839–846. ISSN 0168-9002. doi:10.1016/j.nima.2006.07.066.

[Bir93] Bird, D. J. et al. (High Resolution Fly's Eye Collaboration). *Evidence for correlated changes in the spectrum and composition of cosmic rays at extremely high-energies. Phys. Rev. Lett.*, 71:pp. 3401–3404 (1993). doi:10.1103/PhysRevLett.71.3401.

[BON09] *The angular resolution of the Pierre Auger Observatory*. *Nuclear Physics B - Proceedings Supplements*, 190(Supplement C):pp. 20 – 25 (2009). ISSN 0920-5632. doi:https://doi.org/10.1016/j.nuclphysbps.2009.03.063. Proceedings of the Cosmic Ray International Seminars.

[Che34] Cherenkov, P. A. *Visible emission of clean liquids by action of γ radiation*. *Doklady Akademii Nauk SSSR*, 2:pp. 451+ (1934). URL `http://ufn.ru/en/articles/2007/4/g/`.

[Cou85] de Coulomb, C.-A. *Troisième Mémoire sur l'Electricité et le Magnétisme*. *Mèmoires de l'Acadêmie Royale des Sciences*, pp. 612–638 (1785).

[Dom] Domenico, M. D. et al. doi:10.1088/1475-7516/2013/07/050.

[DS17] De Souza, V. (Pierre Auger Collaboration and Telescope Array Collaboration). *Testing the agreement between the X_{max} distributions measured by the Pierre Auger and Telescope Array Observatories*. In *The 35th International Cosmic Ray Conference* (2017).

[Els01] Elster, J. et al. *Weitere Versuche über die Elektrizitätszerstreuung in abgeschlossenen Luftmengen*. *Phys. Zeit.*, 2:pp. 560–563 (1901).

[Eng11] Engel, R. et al. *Extensive air showers and hadronic interactions at high energy*. *Annual review of nuclear and particle science*, 61:pp. 467–489 (2011).

[Eng16] Engel, R. (Pierre Auger Collaboration). *Upgrade of the Pierre Auger Observatory (AugerPrime)*. *PoS*, ICRC2015:p. 686 (2016).

[ESO99] ESO. *Colour composite image of the crab nebula*. `http://www.eso.org/public/images/eso9948f/` (1999). Accessed: 2018-02-22.

[ESO09] ESO/WFI (Optical), N., MPIfR/ESO/APEX/A.Weiss et al. (Submillimetre). *Colour composite image of Centaurus A*. `http://www.eso.org/public/images/eso0903a/` (2009). Accessed: 2018-02-22.

[Fli] Fliescher, S. (Pierre Auger Collaboration). *Radio detection of cosmic ray induced air showers at the Pierre Auger Observatory*. *Nuclear Instruments and Methods in Physics Research Section A:*

Accelerators, Spectrometers, Detectors and Associated Equipment, (Supplement 1):pp. S124–S129. ISSN 0168-9002. doi:10.1016/j.nima.2010.11.045. 4th International workshop on Acoustic and Radio EeV Neutrino detection Activities.

[Fod02] Fodor, Z. et al. *Relic neutrino masses and the highest energy cosmic rays*. *Journal of High Energy Physics*, 2002(06):p. 046 (2002).

[Gai77] Gaisser, T. K. et al. *Reliability of the method of constant intensity cuts for reconstructing the average development of vertical showers*. *International Cosmic Ray Conference*, 8:pp. 353–357 (1977).

[Gai16] Gaisser, T. et al. *Cosmic rays and particle physics*. Cambridge University Press (2016).

[Gor] Gorham, P. W. et al. (ANITA Collaboration). *Observations of the Askaryan Effect in Ice*. *Phys. Rev. Lett.*, p. 171101 (Oct). doi:10.1103/PhysRevLett.99.171101.

[Gre66] Greisen, K. *End to the cosmic ray spectrum?* *Phys. Rev. Lett.*, 16:pp. 748–750 (1966). doi:10.1103/PhysRevLett.16.748.

[Har10] Harris, G. L. H. et al. *The Distance to NGC 5128 (Centaurus A)*. *Publications of the Astronomical Society of Australia*, 27(4):p. 457462 (2010). doi:10.1071/AS09061.

[Hec98] Heck, D. et al. *Upgrade of the Monte Carlo code CORSIKA to simulate extensive air showers with energies* $> 10^{20}$ *eV*. In *Prepared for Spring Meeting of*, FZKA-6097 (1998).

[Hes12] Hess, V. F. *Über Beobachtungen der durchdringenden Strahlung bei sieben Freiballonfahrten*. *Phys.Zeit.*, XIII:pp. 1084–1091 (1912).

[Hil84] Hillas, A. M. *The origin of ultra-high-energy cosmic rays*. *Annual review of astronomy and astrophysics*, 22(1):pp. 425–444 (1984).

[Hüm10] Hümmer, S. et al. *Energy dependent neutrino flavor ratios from cosmic accelerators on the Hillas plot*. *Astroparticle Physics*, 34(4):pp. 205–224 (2010).

[Jan11] Janka, H.-T. *Supernovae und kosmische Gammablitze: Ursachen und Folgen von Sternexplosionen*. Spektrum Akademischer Verlag (2011).

[Kal99] Kalashev, O. E. et al. *Top-down models and extremely high energy cosmic rays. arXiv preprint astro-ph/9911035* (1999).

[Kaw08] Kawai, H. et al. *Telescope array experiment. Nuclear Physics B-Proceedings Supplements*, 175(SUPPL.: COMPLETE):pp. 221–226 (2008).

[Kei13] Keilhauer, B. et al. *Nitrogen fluorescence in air for observing extensive air showers.* In *EPJ Web of Conferences*, volume 53, p. 01010. EDP Sciences (2013).

[Kli] Klinkhamer, F. R. et al. *Ultrahigh-energy cosmic-ray bounds on nonbirefringent modified-Maxwell theory. Phys.Rev.D77:016002,2008* (June). doi:10.1103/PhysRevD.77.016002. 0709.2502v6.

[Kol13] Kolhörster, W. *Messungen der durchdringenden Strahlung im Freiballon in größeren Höhen. Phys.Zeit.*, XIV (1913).

[Kol14] Kolhörster, W. *Messungen der durchdringenden Strahlung bis in Höhen von* 9300 m. In *Verhandlungen der Physikalischen Gesellschaft zu Berlin*, volume Band 16, pp. 719–721 (1914).

[Kuz98] Kuzmin, V. et al. *Ultrahigh-energy cosmic rays, superheavy long-lived particles, and matter creation after inflation. Journal of Experimental and Theoretical Physics Letters*, 68(4):pp. 271–275 (1998).

[Lid03] Lide, D. *CRC Handbook of Chemistry and Physics, 84th Edition.* CRC HANDBOOK OF CHEMISTRY AND PHYSICS. Taylor & Francis (2003). ISBN 9780849304842.

[Lin63] Linsley, J. *Evidence for a Primary Cosmic-Ray Particle with Energy 10^{20} eV. Physical Review Letters*, 10:pp. 146–148 (February 1963). doi:10.1103/PhysRevLett.10.146.

[Lor04] Lorenz, E. et al. (MAGIC Collaboration). *Status of the 17 m MAGIC telescope. New Astronomy Reviews*, 48(5-6):pp. 339–344 (2004).

[Mat] Matthews, J. *A Heitler model of extensive air showers. Astroparticle Physics*, (5–6):pp. 387–397. ISSN 0927-6505. doi:10.1016/j.astropartphys.2004.09.003.

[Meu] Meurer, C. et al. (Pierre Auger Collaboration). *HEAT – a low energy enhancement of the Pierre Auger Observatory*. *Astrophysics and Space Sciences Transactions*, (2):pp. 183–186. doi:10.5194/astra-7-183-2011.

[Mil] Millikan, R. A. et al. *High Frequency Rays of Cosmic Origin I. Sounding Balloon Observations at Extreme Altitudes*. *Phys. Rev.*, pp. 353–361 (Apr). doi:10.1103/PhysRev.27.353.

[NEW07] *The optimum distance at which to determine the size of a giant air shower*. *Astroparticle Physics*, 26(6):pp. 414 – 419 (2007). ISSN 0927-6505. doi:https://doi.org/10.1016/j.astropartphys.2006.08.003.

[Nie15] Niechciol, M. *A new window to the universe?: searching for ultra-high-energy photons at the Pierre Auger Observatory*. Ph.D. thesis, Universität Siegen (2015).

[Och14] Ochilo, L. et al. *Mass Composition Analysis Using Elongation Rate* (2014). Internal note: GAP-2014-044.

[Oli14] Olive, K. A. et al. (Particle Data Group). *Review of Particle Physics*. *Chin. Phys.*, C38:p. 090001 (2014). doi:10.1088/1674-1137/38/9/090001.

[Ost11] Ostapchenko, S. *Monte Carlo treatment of hadronic interactions in enhanced Pomeron scheme: QGSJET-II model*. *Physical Review D*, 83(1):p. 014018 (2011).

[Pes11] Pesce, R. (Pierre Auger Collaboration). *Energy calibration of data recorded with the surface detectors of the Pierre Auger Observatory: an update*. *Proc. 32nd ICRC, Beijing, China* (2011).

[Pie96] Pierre Auger Collaboration. *The Pierre Auger Project Design Report* (1996).

[Pie12] Pierre Auger Collaboration,. *The rapid atmospheric monitoring system of the Pierre Auger Observatory*. *Journal of Instrumentation*, 7(09):p. P09001 (2012). URL `http://stacks.iop.org/1748-0221/7/i=09/a=P09001`.

[Pie15a] Pierog, T. et al. *EPOS LHC: Test of collective hadronization with data measured at the CERN Large Hadron Collider*. *Physical Review C*, 92(3):p. 034906 (2015).

[Pie15b] Pierre Auger Collaboration. *The Pierre Auger cosmic ray observatory. Nuclear Instruments and Methods in Physics Research Section A: Accelerators, Spectrometers, Detectors and Associated Equipment*, 798:pp. 172–213 (2015).

[Plu] Plum, M. (Pierre Auger Collaboration). *Measurements of the Mass Composition of UHECRs with the Pierre Auger Observatory*. In *Proceedings of 2016 International Conference on Ultra-High Energy Cosmic Rays (UHECR2016)*. doi:10.7566/JPSCP.19.011011.

[Por70] Porter, L. et al. *A space-time detector for cosmic ray showers. Nuclear Instruments and Methods*, 87(1):pp. 87 – 92 (1970). ISSN 0029-554X. doi:https://doi.org/10.1016/0029-554X(70)90886-4. URL http://www.sciencedirect.com/science/article/pii/0029554X70908864.

[Por14] Porcelli, A. *Measurement of the depth of shower maximum in the transition region between galactic and extragalactic cosmic rays with the pierre auger observatory* (2014).

[Rie15] Riehn, F. et al. *A new version of the event generator Sibyll. arXiv preprint arXiv:1510.00568* (2015).

[Ris14a] Risse, M. et al. *Analysis indicator, the power of Λ and p/He ratio* (2014). Internal note: GAP-2014-115.

[Ris14b] Risse, M. et al. *Correlation between depth of shower maximum and signal in ground stations: pure or mixed composition?* (2014). Internal note: GAP-2014-006.

[Sch13] Schröder, F. G. et al. *Cosmic ray measurements with LOPES: Status and recent results*. In *AIP Conference Proceedings*, volume 1535, pp. 78–83. AIP (2013).

[SSD16] *Pierre Auger Observatory homepage*. https://www.auger.org/index.php/news/latest-news/1st-ssd-stations-deployed-in-the-field (2016). Accessed: 2017-11-11.

[Sta10] Stanev, T. *High energy cosmic rays*. Springer Science & Business Media (2010).

[Suo] Suomijärvi, T. (Pierre Auger Collaboration). In *Proceedings of the 30th International Cosmic Ray Conference (ICRC 2007): Merida, Yucatan, Mexico, July 3-11, 2007*.

[Suo09] Suomijärvi, T. et al. (Pierre Auger Collaboration). *Performance and operation of the Surface Detector of the Pierre Auger Observatory*. *Proc. 31st ICRC,(Łódz, Poland)*, 2(009) (2009).

[The] The Pierre Auger Collaboration,. *Properties and performance of the prototype instrument for the Pierre Auger Observatory*. *Nuclear Instruments and Methods in Physics Research Section A: Accelerators, Spectrometers, Detectors and Associated Equipment*, (1 - 2):pp. 50–95. ISSN 0168-9002. doi:10.1016/j.nima.2003.12.012.

[Tue13] Tueros, M. J. (Pierre Auger Collaboration). *Estimate of the non-calorimetric energy of showers observed with the fluorescence and surface detectors of the Pierre Auger Observatory*. In *Proceedings of the 33rd Int. Cosmic Ray Conf., Rio de Janeiro, Brazil* (2013).

[Val15] Valino, I. (Pierre Auger Collaboration). *The flux of ultra-high energy cosmic rays after ten years of operation of the Pierre Auger Observatory*. *PoS*, p. 271 (2015).

[Var13] Varela, E. (Pierre Auger Collaboration). *The low-energy extensions of the Pierre Auger Observatory*. *Journal of Physics: Conference Series*, 468(1):p. 012013 (2013). URL `http://stacks.iop.org/1742-6596/468/i=1/a=012013`.

[Veb13] Veberič, D. *Maps of the Pierre Auger Observatory*. `https://web.ikp.kit.edu/darko/auger/auger-array/` (2013). Accessed: 2017-11-20.

[Ver13] Verzi, V. (Pierre Auger Collaboration). *The Energy Scale of the Pierre Auger Observatory*. In *Proceedings, 33rd International Cosmic Ray Conference (ICRC2013): Rio de Janeiro, Brazil, July 2-9, 2013*, p. 0928 (2013). URL `http://www.cbpf.br/%7Eicrc2013/papers/icrc2013-0928.pdf`.

[Wer14] Werner, M. et al. *Sensitivity of the exponential slope of the $X_{\max}$ distribution tail to the primary mass composition* (2014). Internal note: GAP-2014-059.

[Wil01] Wilson, C. *On the Ionisation of Atmospheric Air*. *Proceedings of the Royal Society of London A*, 68:pp. 151–161 (1901).

[Wul09] Wulf, T. *Beobachtungen über die Strahlung hoher Durchdringungsfähigkeit auf dem Eiffelturm*. *Phys.Zeit.*, 10:pp. 152–157 (1909).

[You12] Younk, P. et al. *Sensitivity of the correlation between the depth of shower maximum and the muon shower size to the cosmic ray composition*. *Astroparticle Physics*, 35(12):pp. 807–812 (2012).

[Zat66] Zatsepin, G. T. et al. *Upper Limit of the Spectrum of Cosmic Rays*. *Soviet Journal of Experimental and Theoretical Physics Letters*, 4:p. 78 (August 1966).

[Zor15] Zorn, J. *Preparation of an Extended Measurement Cycle of the Fluorescence Telescopes of the Pierre Auger Observatory*. Master's thesis, Institut für Experimentelle Kernphysik (IEKP) (2015).

List of Figures

List of Tables

F Acknowledgements

Eine solche Arbeit wie diese kann nicht entstehen, ohne die Hilfe und Unterstützung vieler Menschen. An dieser Stelle möchte ich einigen von ihnen meinen besonderen Dank aussprechen.

An erster Stelle sei hier Prof. Markus Risse zu nennen, der mir die Möglichkeit gab an seinem Lehrstuhl zu forschen und der erste Gutachter dieser Arbeit ist. Ich habe seine Kollegialität, seinen Rat und die Zusammenarbeit stets sehr geschätzt und möchte mich für all dies bedanken.

Ebenfalls verdient Prof. Ivor Fleck meinen Dank, der sich als Zweitgutachter für diese Arbeit zur Verfügung gestellt hat. Ebenso danke ich den Professoren Christopher Wiebusch und Guido Bell, die die Promotionskomission vervollständigen.

Neben Prof. Risse möchte ich mich auch bei Dr. Alexey Yushkov bedanken, der meine Arbeit von Anfang bis Ende mit betreut hat, neue Ideen eingebracht, die GAP-notes und Kapitel dieser Arbeit Korrektur gelesen und schlussendlich die dedizierten Simulationen für die Anwendung der entwickelten Analyse bereit gestellt hat. Ohne ihn wäre die Arbeit in der vorliegenden Form nicht möglich gewesen.

Weiteren Dank möchte ich Dr. Marcus Niechciol aussprechen, der zum einen wichtige Korrekturen an dieser Arbeit angeregt hat und zum anderen über all die Jahre stets ein angenehmes Klima im gemeinsamen Büro verbreitet hat, dass die Arbeit sehr angenehm gestaltete.

Für ein angenehmes Arbeitsklima sind jedoch auch die Kollegen ausschlaggebend, die nicht im selben Raum arbeiten. Ihnen sei hier auch gedankt, insbesondere Alexander Aab, Sebastian Sonntag, Livingstone Ochilo, Philip Rühl und Mona Erfani für die stets interessanten Gespräche und die tolle Zusammenarbeit bei der Planung des Youngster's Meeting.

Weiterer Dank gebührt Prof. Klinkhamer und Dr. Jorge De Diaz für die Diskussionen über Verletzung der Lorentzinvarianz und den damit verbundenen Einstieg in die spezifische Motivation für die hier gezeigte Analyse.

Neben der akademischen Unterstützung bedarf es allerdings auch Hilfe aus dem privaten Umfeld. Daher möchte ich meinen größten Dank sowohl meinen Eltern Andrea und Jörg sowie meinem Bruder Marius aussprechen, die mich in der Zeit meiner Promotionsarbeit nicht nur emotional, ideologisch und finanziell unterstützt haben, sondern mich

auch initial dazu motiviert haben diesen Schritt zu gehen.

Meiner Partnerin Verena Schmitz gebührt mein Dank für die stets emotionale Unterstützung und die Bereicherung meines Lebens gerade in der Schlusszeit dieser Arbeit.

Neben der Familie sind die Freunde eine Konstante in meinem Leben. Sie sorgten stets für Ablenkung und Zerstreuung, wenn ich sie brauchte, und halfen mir des¨fteren auf meinen Weg zurück zu finden, als es schien, dass ich ihn verloren hatte. Dafür danke ich Pierre Meinokat, Stefanie Glaeser sowie Nora Heiting, auch für ihre vielseitige Unterstützung für die Dissertation.

In eine neue Stadt zu ziehen ist niemals leicht, daher ist jegliche Unterstützung für den Anfang willkommen. In diesem Zusammenhang möchte ich mich beim Löschzug 2 der Freiwilligen Feuerwehr der Stadt Siegen bedanken, der mich schnell in ihren Reihen aufnahm und auch tatkräftig bei meinem Umzug mit anpackte.

Zum Abschluss möchte ich nochmal der Person danken, die an all dem hier maßgeblich die Schuld trägt: Ohne den mitreißenden Physikunterricht von Klaus Hegel in der Mittel- und Oberstufe hätte ich diesen Weg vermutlich niemals eingeschlagen. Meinen allerherzlichsten Dank dafür.